5-9-2024

The Conceptual Design, Analysis and Optimization of a Hydrogen Combustion and a Hydrogen Fuel-Cell Powered Aircraft

Michael Kiely
Washington University – McKelvey School of Engineering

Recommended Citation

Kiely, Michael, "The Conceptual Design, Analysis and Optimization of a Hydrogen Combustion and a Hydrogen Fuel-Cell Powered Aircraft" (2024). *McKelvey School of Engineering Theses & Dissertations*. 1031.
https://openscholarship.wustl.edu/eng_etds/1031

WASHINGTON UNIVERSITY IN ST. LOUIS

McKelvey School of Engineering
Department of Mechanical Engineering and Materials Science

Dissertation Examination Committee:
Ramesh K. Agarwal, Chair
Richard Axelbaum
Swami Karunamoorthy
Xianglin Li
David Peters

The Conceptual Design, Analysis, and Optimization of a Hydrogen Combustion and a Hydrogen Fuel-Cell Powered Aircraft

by
Michael Kiely

A dissertation presented to
the McKelvey School of Engineering
of Washington University in
partial fulfillment of the
requirements for the degree
of Doctor of Philosophy

May 2024
St. Louis, Missouri

Table of Contents

List of Figures vii

List of Tables x

Acknowledgments xi

Abstract xii

Chapter 1: Introduction 1

- 1.1 Motivation 1
- 1.2 Background 2
- 1.3 Hydrogen Powered Aircraft 3
  - 1.3.1 Propulsion Systems – Hydrogen Combustion vs. Hydrogen Fuel Cell 4
  - 1.3.2 Background and Literature Review 5
- 1.4 Proposed Configurations 6
  - 1.4.1 Hydrogen Combustion Aircraft Configuration 7
  - 1.4.2 Hydrogen Fuel Cell Configurations 8
  - 1.4.3 Truss Braced Wing Aircraft Configuration 8
- 1.5 Design Process 9
  - 1.5.1 Preliminary Design 10
  - 1.5.2 Intermediate Design 10
  - 1.5.3 Aerodynamic Shape Optimization 11
- 1.6 Objective 11

Chapter 2: WUADS – An Aircraft Conceptual Design Tool 14

2.1 Introduction 14

2.2 Methodology 14

2.2.1 Weight Estimation 16

2.2.2 Vortex Lattice Method 17

2.2.3 Drag Estimation Methods 18

2.2.4 Propulsion Performance Estimation 22

2.2.5 Breguet Range Equation 25

2.3 Code Structure 27

2.4 Bayesian Optimization 28

2.5 Validation 30

2.5.1 Weights and Range Estimates 31

2.5.2 Optimization 33

Chapter 3: Hydrogen Combustion Powered Aircraft 36

3.1 Methodology 36

3.2 External Fuel Tank Configuration 37

3.2.1 Design 37

3.2.2 Results 38

3.3 Internal Fuel Tank Configuration 39

3.3.1 Design 39

3.3.2 Results 41

Chapter 4: Modeling of Powertrain for Hydrogen Fuel Cell Powered Aircraft 42

4.1 Introduction 42

4.2 Powertrain Components ... 42

4.2.1 Fuel Cell Stacks ... 43

4.2.2 Turbo-Normalizing Compressor ... 44

4.2.3 Thermal Management System ... 45

4.2.4 Hybrid Battery-Fuel Cell Power ... 48

4.2.5 Hybrid Turbogenerator-Fuel Cell Power ... 49

4.3 Powertrain Modeling ... 49

4.3.1 Fuel Cell Model ... 50

4.3.2 Compressor ... 52

4.3.3 Cooling System ... 53

4.3.4 Subsystems ... 54

4.4 System Performance and Optimization ... 54

Chapter 5: Hydrogen Fuel Cell Powered Aircraft Configurations ... 56

5.1 Proposed Configurations ... 56

5.2 Design Process ... 60

5.3 Test Case – Cessna 208 Caravan ... 62

5.3.1 Problem Setup ... 62

5.3.2 Results ... 63

5.4 Technology Readiness Evaluation – CRJ200 ... 64

5.4.1 Problem Definition ... 64

5.4.2 Problem Setup ... 65

5.4.3 Component Performance Estimates ... 66

5.4.4 Results 67

5.5 B717-200 Class Aircraft 69

5.5.1 Problem Definition 69

5.5.2 Mission Profile 70

5.5.3 Configuration Optimization 71

5.5.4 Analysis and Results 73

Chapter 6: Optimization of 2D Airfoils 75

6.1 Introduction 75

6.2 Airfoil Parameterization 75

6.2.1 Bezier-Parsec Parameterization 75

6.2.2 CST Parameterization 77

6.3 WuFoil 78

6.4 Convolutional Neural Networks (CNN) for Airfoil Prediction 80

6.4.1 Introduction 80

6.4.2 Neural Network Setup 82

6.4.3 Results 83

6.5 2D Airfoil Optimization 83

6.5.1 Problem Setup and Methodology 83

6.5.2 Results 84

Chapter 7: Optimization of Airfoils for 3D Wing 89

7.1 Introduction 89

7.2 2D to 3D Airfoil Mapping Methods 89

7.2.1 2.5D Mapping 89

7.2.2 2.75D Mapping 90

7.2.3 2.75D Mapping with Curvature Correction 92

7.3 Full Wing Optimization 94

7.3.1 Problem Set up 94

7.3.2 Methodology 95

7.3.3 Results 95

7.4 3D Wing Analysis 97

7.4.1 Methodology 98

7.4.2 Results 99

Chapter 8: Summary and Future Work 102

8.1 Summary 102

8.2 Future Work 103

References 105

Appendix A: Weight Estimation Methods 113

Appendix B: Generalized Turbofan Model 122

List of Figures

Figure 1.1 Hydrogen powered aircraft configurations with external LH2 tanks (left) and internal LH2 tanks (right) 4

Figure 1.2 Yearly aviation carbon emissions by aircraft class [3] 7

Figure 1.3 Boeing's high transonic truss-braced wing configuration (SUGAR) 9

Figure 2.1 WUADS code structure 16

Figure 2.2 Boeing's published values vs. WUADS estimated values for the range of Boeing 737-800 [38] 33

Figure 2.3 Convergence history of the 737-800 wing shape optimization problem 34

Figure 3.1 B 737-800 mission profile used for the analysis of aircraft configuration with hydrogen combustion. 36

Figure 3.2 Schematic of B737-800 based hydrogen combustion aircraft configuration with externally mounted fuel tanks. 38

Figure 3.3 Hydrogen combustion powered aircraft based on the fuselage of the B767 with internal LH2 fuel tanks 40

Figure 4.1 Model of the powertrain of a hydrogen fuel cell powered aircraft 43

Figure 4.2 Turbo normalizing compressor system 45

Figure 4.3 Powertrain thermal management system 46

Figure 4.4 Power required during the takeoff and climb sections normalized by the power required at cruise 48

Figure 4.5 Powertrain weight (left) and SFC (right) for a 1MW hydrogen fuel cell powertrain . 55

Figure 5.1 Proposed hydrogen fuel cell powered aircraft configuration with aft fuel tanks 57

Figure 5.2 Proposed hydrogen fuel cell powered aircraft configuration with aft and overhead fuel tanks 58
Figure 5.3 Cross sectional view of the overhead fuel tank configuration 59
Figure 5.4 Aircraft configuration with a truss braced wing 60
Figure 5.5 Hydrogen fuel cell powered aircraft design process 61
Figure 5.6 Cessna 208 Caravan 62
Figure 5.7 Baseline model of the Bombardier CRJ200 65
Figure 5.8 Hydrogen fuel cell powertrain subsystem sizing at different levels of technological advancement 67
Figure 5.9 Two potential configurations of hydrogen fuel cell powered aircraft 70
Figure 5.10 Cruise Mach number vs. maximum range for standard and truss braced wing configurations 71
Figure 5.11 Fuel required vs. design range for each tested configuration 73
Figure 6.1 Bezier-Parsec Parameterized Airfoil 76
Figure 6.2 WUFoil generated airfoil mesh 79
Figure 6.3 A sketch of the framework of Multi-Layer Perceptron (MLP) Artificial Neural Network (ANN) 81
Figure 6.4 Optimized mid-span airfoil compared to the original B737 mid-span airfoil 85
Figure 6.5 Shock wave formation on the surface of the optimized mid-span airfoil (left) and the original B737 mid-span airfoil (right) 85
Figure 6.6 Optimized outboard airfoil vs original 737 outboard airfoil 86
Figure 6.7 Shock wave formation on optimized and original B737 outboard airfoils 86
Figure 6.8 Comparison of the optimized airfoils with and without neural net regression 87

Figure 7.1 Baseline 2D airfoil and 3D airfoil in simple sweep theory 90

Figure 7.2 Conical parameters on a swept tapered wing 91

Figure 7.3 Airfoil optimization results at various wing sections 96

Figure 7.4 Shock wave formation on the optimized airfoil at y/b = 0.6. 97

Figure 7.5 3D wing with fully optimized airfoil distribution 97

Figure 7.6 Coarsened version of mesh used in full wing CFD simulation. 98

Figure 7.7 Pressure coefficient distribution on the 3D optimized wing. 99

Figure 7.8 Comparison of pressure distributions on airfoils at various sections of the optimized wingspan using the full 3D CFD and 2.75 D theory. 100

List of Tables

Table 2.1 Constants used in Howe's Engine Performance Estimates [29] 23

Table 2.2 Characteristics of 4 WUADS tests cases 30

Table 2.3 Calculated values from WUADS vs published values for range and weight predictions. 31

Table 2.4 Optimized wing shape results vs. real world values for the Boeing 737-800............. 35

Table 3.1 Wing optimization results for hydrogen combustion powered aircraft with 767 Body40

Table 3.2 Fuel costs for B737-800 and modified B767 hydrogen combustion powered aircraft configurations at mission ranges of 1500 and 2500 nmi 41

Table 4.1 Fuel cell model parameters 51

Table 5.1 Performance of the hydrogen fuel cell (HFC) powered Cessna 208 compared to the baseline aircraft.. 63

Table 5.2 Hydrogen fuel cell powertrain's component weight and power requirements for Cessna 208.. 64

Table 5.3 Performance estimates for future fuel cell powertrain subsystems in the years 2025, 2030, and 2035... 66

Table 5.4 Performance of hydrogen fuel cell powered CRJ200 at different technology levels .. 68

Table 5.5 Calculated optimum variables of standard and truss braced wing aircraft configurations 72

Table 6.1 Drag coefficients of the optimized airfoils with and without using CNN regression.. 88

Table B.1 Maximum thrust (lbf.) at different altitudes (ft.) and Mach Numbers 122

Table B.2 Specific fuel consumption at different altitudes (ft.) and Mach Numbers 122

Acknowledgments

I would like to express my most sincere gratitude to Dr. Ramesh Agarwal for his continued guidance and support throughout this whole process of research towards doctoral degree and completion of this dissertation. His extensive knowledge in the field of aerodynamics and mentorship have been instrumental in my development as an engineer. Along the same lines, I would like to thank Chris Rice (retired engineer from Boeing – St. Louis) for his continued guidance and expansive knowledge of the aerospace industry to provide valuable assistance in all aspects of this dissertation.

An additional debt of gratitude goes to all members of my PhD committee and staff of the MEMS department, as well as to all my colleagues in the Computational Fluid Dynamics (CFD) Laboratory. My time at Washington University in Saint Louis has truly been an honor and a privilege, thanks to the wonderful environment cultivated by all these people.

Last but certainly not least, I would like to thank my parents Dan and Theresa and my partner Emily. I am truly fortunate in life to be surrounded by such genuine, incredible people and this thesis serves as a testament of their continued love and support.

Mike Kiely

Washington University in St. Louis

May 2024

ABSTRACT OF THE DISSERTATION

The Conceptual Design, Analysis and Optimization of a Hydrogen Combustion and a Hydrogen Fuel-Cell Powered Aircraft

by

Michael Kiely

Doctor of Philosophy in Aerospace Engineering

Washington University in St. Louis, 2024

Professor Ramesh Agarwal, Chair

In the effort to combat climate change worldwide, the aviation industry faces particularly complex design challenges in designing new, emission free vehicles. One potential solution to this problem is the use of hydrogen fuel as a means of propulsion. Hydrogen fuel has many benefits over traditional jet fuel such as a higher gravimetric energy density; however, it requires the aircraft to carry large, pressurized, cryogenic fuel tanks. This thesis examines the design challenges, potential solutions, and the analysis methods for the design of a short to medium range hydrogen powered commercial airliner. To accomplish this goal, a comprehensive conceptual design and analysis code called WUADS (Washington University Aircraft Design Software) is developed. WUADS employs a combination of empirical and numerical methods to analyze an arbitrarily input aircraft's overall weight, propulsive efficiency, and aerodynamic performance. This code is first validated on several existing aircraft to verify the accuracy of the analysis and optimization methodology of WUADS, then it is used to analyze several configurations of hydrogen powered aircraft. The first hydrogen powered configuration tested is a medium range airliner based on the performance metric of the Boeing 737-800, which makes use of propulsion through direct hydrogen combustion. The Preliminary analysis shows that the optimal placement of the required cryogenic hydrogen fuel tanks is inside the fuselage. With this knowledge, a hydrogen powered aircraft configuration is designed and optimized with an extended fuselage to fit the fuel tanks. This configuration demonstrates a clear increase in efficiency over the Boeing 737-800. Next, the design of an electric hydrogen fuel cell powered configuration is analyzed. A system architecture for the electrified powertrain and its required subcomponents is developed and modelled to determine the propulsive efficiency of such a design. These models are used to test three configurations of hydrogen fuel cell powered aircraft which are based on the Cessna 208 Caravan, the Bombardier CRJ-200, and the Boeing 717-200. The models employed for the hydrogen fuel cell powertrain are first validated on the Cessna 208 configuration. Next, the projected component efficiencies at technology levels in the near future are tested on the Bombardier CRJ-200 configuration where it is determined that a hydrogen fuel cell powered aircraft could be highly efficient and technologically viable by the year 2035. Finally, the Boeing 717-200 configuration is used to analyze a hydrogen fuel cell powered configuration's efficiency against a hydrogen combustion powered configuration at different design ranges. A truss braced wing model is also employed for additional increases to the efficiency. It is determined that the hydrogen fuel cells are effective in design ranges shorter than 2000 nmi; however, the hydrogen combustion may be required beyond this range. With these geometrically optimized designs, a more detailed analysis of the aerodynamic shape optimization of the wing is performed. Both the airfoil and twist distribution across the wing are optimized using machine learning based optimization methods. In this analysis, highly efficient, supercritical airfoils are designed using Bayesian optimization. An artificial neural network model is employed in attempt to increase the computational efficiency and is found to provide near optimal results. The 2D to 3D airfoil mapping methods are then employed to optimize the airfoil distribution of an entire transonic wing.

Chapter 1: Introduction

1.1 Motivation

As global temperatures continue to rise, it is currently of utmost importance that emission free solutions for all major industries are thoroughly researched and developed. The commercial aviation industry represents roughly 2-3% of the yearly carbon emissions; however, it presents one of the most unique challenges in the path towards decarbonization [1, 2]. The overall design of commercial transport jets has remained almost the same since the industry's inception, and for a good reason. Traditional kerosene-based jet fuel has a high volumetric energy density and requires no special pressurized tank to carry it on the aircraft; it is generally stored easily in the wings of a commercial aircraft. This allows for the design of a sleek, highly efficient aircraft with minimal special consideration of fuel storage. This luxury however is not granted in the design of emission free aircraft, such as the novel concept of a CO_2 emission free hydrogen powered aircraft. For a hydrogen powered aircraft, the entire aircraft configuration needs be redesigned considering the storage of the cryogenic hydrogen fuel and the new propulsion system for combustion of hydrogen. The overarching goal of research in this dissertation is to analyze the optimal design and viability of several potential aircraft configurations with engines using hydrogen as fuel. Achieving this objective however poses unique challenges for aircraft aerodynamics and design optimization. Therefore, the additional goal of this work is to examine and implement new, state-of-the-art analysis tools and optimization techniques to assist in expediting the conceptual design process of an emission free aircraft. An additional goal of this dissertation is to design a hydrogen fuel cell powered aircraft which is totally emissions free.

1.2 Background

Several potential alternative fuel sources other than Jet A or kerosene have been proposed for reducing or mitigating the CO_2 emissions from an aircraft. Sustainable Aviation Fuel (SAF), being a drop-in fuel, provides the simplest and immediate impactful solution. SAF's are a type of biofuels created using the leftover biomass produced by farmlands which can reduce carbon emissions by up to 80% [1, 2]. The key benefit of SAFs are the fuels' close chemical properties to the traditional Jet-A fuel, so that the existing aircraft would only have to undergo very limited retrofitting to operate using SAF; it is for this reason that SAFs are called the 'drop-in' fuels and they are a subject of extensive investigation by the aircraft manufacturers and the fuel providers around the world with a clear plan of scaling the global supply of SAF progressively until 2050 as described in the US Department of Energy's 2021 pledge to produce enough SAF to meet 100% of the aviation sector's fuel demand by the year 2050 [3, 4]. While SAF's will remain critical in short to medium term for reduction of greenhouse gas emission due to aviation, they present several challenges which would ultimately prevent a complete reliance on them. First, SAF's by nature are not entirely emission free, with differing sources reporting large variation in reduction of the lifecycle CO_2 emission between 40 to 70% of current values [5]. Additionally, a complete shift to the use of SAFs would require an expensive large scale sustained investment in biofuel manufacturing along with an extensive allotment of resources for producing the required non-consumable biomass (nonfood crops). In fact, O'Malley et al. in 2021 estimated that only 5.5% of the EU's jet fuel requirements could be supplied by SAF produced by the byproducts of existing feedstock [6]. For these reasons, although SAF remains a highly important development for immediate reduction of CO_2 emissions, alternative power sources still must be developed.

Full electric power using batteries has been researched and tested to great effect for aircraft propulsion. NASA estimates suggest that the threshold energy density for batteries to be used efficiently for commercial aircraft is 750 Wh/Kg, well above what is currently achievable [7, 8]. Current advancements in lithium based solid state batteries seem promising with energy densities of up to 500-600 Wh/Kg; however, these values are still far too less to act as the main power source for a medium to long range commercial aircraft [9].

Perhaps the most promising solution to the decarbonization of the commercial aviation industry is the use of hydrogen fuel. Hydrogen as a fuel source has the benefit of having a gravimetric energy density about 2.8 times higher than the traditional kerosene-based jet fuel; however, it has a much lower volumetric energy density, which is four times lower than that of Jet-A. In terms of design, this means that a hydrogen-based aircraft would have a lower fuel weight requirement but would require the use of large, pressurized cryogenic fuel tanks instead of storing the fuel in the wing. This is the main challenge in the design of any hydrogen powered aircraft. A hydrogen powered aircraft could be powered through either direct combustion of hydrogen in a gas turbine or by using an electrified drivetrain using an array of hydrogen fuel cell, the differences between the two approaches is discussed in the next sections.

1.3 Hydrogen Powered Aircraft

As previously mentioned, the liquid hydrogen has the benefit of 2.9 times higher gravimetric energy density than the traditional jet fuel but has four times lower volumetric density compared to Jet-A, therefore requires cryogenic, pressurized fuel storage tanks to store the fuel which must be stored either inside the fuselage or be externally mounted on the wings thus further increasing the structural weight of the aircraft. These two potential designs of a hydrogen powered aircraft are shown in Figure 1.1. Furthermore, a drag cost is incurred due to the addition of these fuel tanks further reducing the aircraft efficiency.

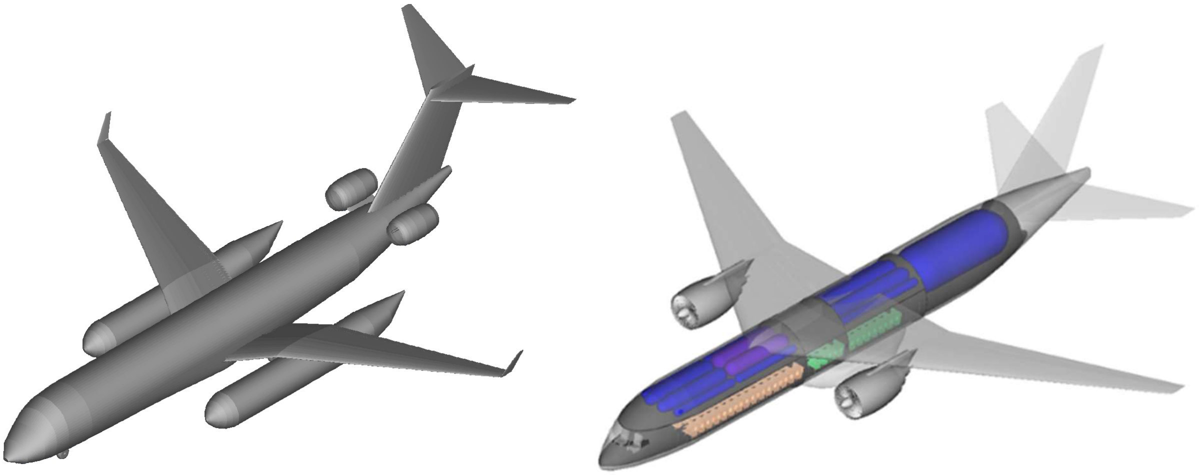

Figure 1.1 Hydrogen powered aircraft configurations with external LH2 tanks (left) and internal LH2 tanks (right)

1.3.1 Propulsion Systems – Hydrogen Combustion vs. Hydrogen Fuel Cell

Two potential propulsion system have been proposed in the literature for powering a hydrogen powered aircraft: direct hydrogen combustion and hydrogen fuel cells. A hydrogen combustion power aircraft would operate using a propulsion system powered by the direct combustion of liquid hydrogen fuel, much like the jet fuel in current jet engines with some modifications. This approach has the potential to be highly efficient and is straightforward. Additionally, with the high energy density of the fuel, a hydrogen combustion powered aircraft could theoretically have a much greater fuel efficiency than the traditional jet fuel aircraft. However, a hydrogen combustion powered aircraft has the inherent drawback of not being entirely emission free. It is true that it is free of all carbon emissions; however, the combustion of hydrogen would still produce Nitrogen Oxide (NOx) and water vapor, which can result in contrails.

The second alternative is the use of hydrogen fuel cells to power a fully electrified powertrain. A hydrogen fuel cell is a device which converts the chemical energy of hydrogen fuel into electricity through a chemical reaction with oxygen, producing only water as a byproduct. In a hydrogen fuel cell configuration, the aircraft would be propelled using a number of electric propeller engines. This configuration has the same natural benefits of a hydrogen combustion engine, however, experiences a number of drawbacks as well. Namely, the addition of a fuel cell powered electrified powertrain introduces significant structural weight and complexity to the propulsion system. Additionally, the size of the required fuel cell stacks is seen to increase exponentially with the cruise velocity due to power requirements, potentially limiting the efficiency of the aircraft at traditional transonic cruise Mach numbers. For these reasons, it is generally believed that, in the near future, the potential of a hydrogen fuel cell powered aircraft will be limited to aircraft of smaller size and range, for example the general aviation and regional airliners.

1.3.2 Background and Literature Review

The use of hydrogen as an alternative fuel source is far from a novel concept, in fact this idea goes back over 60 years. The U.S. Airforce first experimented with the use of a hydrogen combustion powered turbojet engine to reduce the total takeoff weight on a B-57 bomber aircraft all the way back in 1957 and continued developing plans for hydrogen powered aircraft through the 1970's [10]. Continued interest in the use of hydrogen fuel for commercial aircraft existed in companies such as Lockheed and Airbus through the 2000's; however, a general lack of funding in these concepts ultimately resulted in a hydrogen powered commercial aircraft never being built. It wasn't until the 2010's when a general renewal of interest in hydrogen powered aircraft generated as a solution to the decarbonization of commercial aviation.

In June 2012, Boeing conducted the first test flight of its new liquid hydrogen powered high-altitude long-endurance unmanned aerial vehicle, the Phantom Eye [11]. Featuring a large wingspan of 150 ft, a 450 lb. payload, and a cruise ceiling of up to 65,000 ft., this demonstrator served to prove the efficiency of increasing possibilities of hydrogen powered combustion engines.

In Europe, fueled by the potential ban on fossil fuel powered aircraft, a large scale multinational effort has been underway to design an aircraft with alternative fuels, other than Jet-A and kerosene, since the mid 2010's. Spearheading this effort is Airbus with its "ZEROe" program, a pledge to produce a fully hydrogen powered fleet of aircraft by the year 2035 [12]. This initiative has shown key innovation demonstrations on both hydrogen combustion and hydrogen fuel cell powered aircraft engines, with conceptual configurations being designed for both these modes of propulsion. In USA, perhaps the most prolific development in hydrogen powered aircraft has been the NASA funded CHEETA program from the University of Illinois. This project aims to develop a hydrogen fuel cell powered aircraft comparable to the Boeing 737 [13]. Beyond conceptual aircraft design, this project has served as a launchpad for the development of key, state-of-the-art, highly efficient electronic systems for use on an electrified aircraft. Key work has been conducted in fields such as cryogenically cooled superconducting motors, ducted fan based distributed propulsion systems, boundary layer ingestion, and more. Numerous ongoing projects exist in the field of hydrogen powered regional size aircraft being conducted by the universities and private companies as well, such as the GKN Aerospace's H2GEAR project or ZeroAvia's retrofitted hydrogen fuel cell powered Dornier 228, which flew its first test flight in January 2023 [14, 15]. In fact, as recently as February 2024, Universal Hydrogen announced the successful testing of the world's first Megawatt-class hydrogen fuel cell powered aircraft [16].

1.4 Proposed Configurations

Several potential configurations of hydrogen powered aircraft are proposed and analyzed in this dissertation. While selecting a proposed configuration, it is important to decide the class of flight in which the aircraft will operate in. As shown below in Fig. 1.2, the commercial aircraft produce an overwhelming majority of the aviation sector's yearly carbon emissions, and thus have been selected as the key market to aid in the decarbonization efforts.

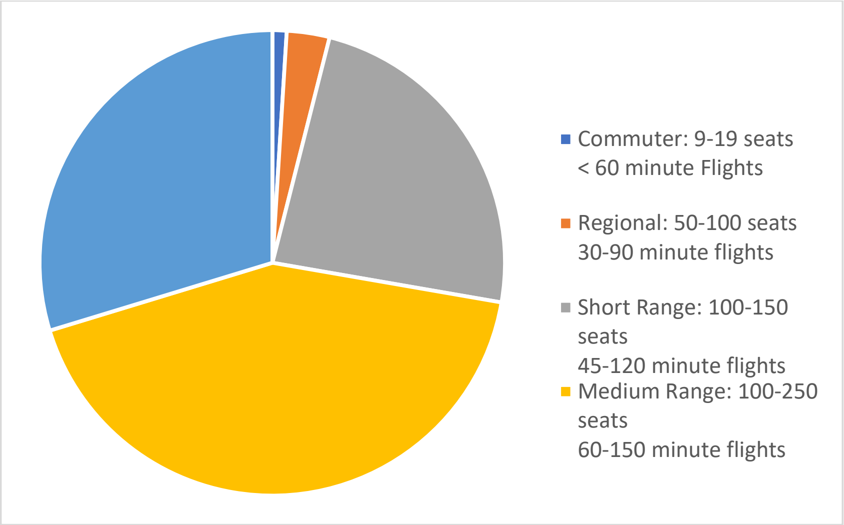

Figure 1.2 Yearly aviation carbon emissions by aircraft class [3]

The goal of this work is to analyze these configurations in the regional, short range, and medium range aircraft classes, since the long-range flights are likely to remain unachievable for the hydrogen powered aircraft in near future. This is accomplished in this dissertation by selecting widely used, well established aircraft in each of these regimes as a comparison point. The proposed configurations will employ these established aircraft to determine their target mission ranges, passenger count, cargo weight, etc. as well as the baseline geometry.

1.4.1 Hydrogen Combustion Aircraft Configuration

For the first configuration considered, the Boeing 737-800 is used as a target for the design and analysis of a hydrogen combustion powered aircraft. The Boeing 737-800 and other comparable planes are the most frequently flown planes in the world and make up an overwhelming majority of flights in the medium range aircraft class, making this size aircraft an obvious choice for decarbonization efforts. This configuration is designed using the baseline mission profile and passenger count of the 737-800; however, it is altered to include the hydrogen fuel tanks and is aerodynamically optimized. Both a configuration with internal LH2 tanks and a configuration with external LH2 tanks are analyzed and are compared. The design of this configuration is examined in Chapter 3.

1.4.2 Hydrogen Fuel Cell Configurations

A hydrogen fuel cell powered aircraft poses a highly complex challenge in conceptual design. First the system infrastructure for the hydrogen fuel cell powertrain must be designed and modelled to estimate the performance of the propulsion system. Using these developed models, several hydrogen fuel cells powered aircraft configurations are analyzed ranging from commuter aircraft to medium range. The first configuration that is examined is a 50-passenger regional size aircraft. Although not the most widely used class of aircraft, a regional size airliner is an important step in the technological innovation required for the hydrogen fuel cell powered aircraft. For this reason, a regional size aircraft configuration is used to test efficiencies of various components at different technology levels. Next, a short-range airliner configuration based on the Boeing 717-200 is considered. This configuration is analyzed and optimized for different design ranges between 1000 and 2300 nmi and is compared to a similarly designed hydrogen combustion powered aircraft configuration.

1.4.3 Truss Braced Wing Aircraft Configuration

Another configuration that is examined is the potential use of a truss braced wing on a hydrogen fuel cell powered aircraft configuration. A truss braced wing is a concept in which a truss is used to greatly increase the aspect ratio of an aircraft; it has garnered significant amount of attention in recent years, particularly with Boeing’s ongoing Subsonic Ultra Green Aircraft Research (SUGAR) project. In this project, Boeing and NASA found that the use of a truss was able to significantly reduce the structural and aeroelastic concerns of the wing allowing a mid-sized commercial aircraft to have aspect ratios up to 23 and a lift to drag ratio at cruise up to 26 [17]. These advancements should greatly increase the range and efficiency of an aircraft. A schematic of one of the configurations tested in the SUGAR project is shown below in Fig. 1.3.

Figure 1.3 Boeing's high transonic truss-braced wing configuration (SUGAR)

1.5 Design Process

The addition of the extra drag introduced in a hydrogen powered aircraft due to LH2 fuel tanks means that these configurations require a special degree of aerodynamic optimization. The process of this optimization is a highly complex issue in which variables such as the overall structural weight and drag must be balanced to maximize efficiencies. To analyze and optimize a large number of such complex configurations, new and computationally efficient design methodology must be developed and employed. Therefore, a secondary but important objective of this research is to implement modern design methodologies in shape optimization of a hydrogen powered aircraft. A comprehensive, model based, conceptual aircraft design and optimization code called WUADS (Washington University Aircraft Design System) has been developed for this purpose. Further discussion on design and implementation of WUADS is provided in Chapter 2.

The conceptual design process in this dissertation has been split into two parts: the preliminary design and the intermediate design. In general, the preliminary design concerns optimizing the high-level concepts of the aircraft such as the wing planform shape using the low fidelity highly efficient methods. WUADS was used extensively in the preliminary design process. Intermediate design concerns more finely detailed design variables such as airfoil distribution on the wing which require a much higher degree of fidelity. Note that while these two design stages are presented in this dissertation as separate processes, these labels are not rigidly designated, and the methodology presented extends through all stages of the aircraft's design.

1.5.1 Preliminary Design

Traditionally the preliminary design process of an aircraft relies heavily on the utilization of a variety of empirical methods derived from experimental results and empirical estimations, however low fidelity CFD results from codes based on the panel methods can be utilized for this process as well. Consolidating these results with the results from various empirical weight estimation methods can allow for the full performance characteristics of a given aircraft configuration to be rapidly estimated within reasonable accuracy. Automation of this process can allow numerous configurations of aircraft to be tested and optimized in a highly computationally efficient manner. This is precisely the reason the WUADS code was developed and implemented, to optimize the basic aerodynamic shape of an aircraft. Finer details of an aircraft's aerodynamic layout such as airfoil and twist distribution require the use of higher fidelity methods.

1.5.2 Intermediate Design

Intermediate design beyond the general aerodynamic layout of the aircraft requires a higher fidelity prediction of aerodynamic performance than the empirical estimates and the simple panel methods are able to provide. For these purposes full RANS CFD simulations are required. A key example of intermediate level design that will be examined in this work involves a wing's airfoil and twist distribution. Transonic airfoil design optimization is a highly complex field which involves predicting flows which often include shock wave and shock induced separation effects. Modern airfoil design aims to mitigate these shock waves and separation effects by employing the so called supercritical airfoils. Using the general wing shape derived from the previous methods, high fidelity CFD results can be used to optimize the wing to a much finer detail. This process in its current state is performed by dividing the wing into a number of two-dimensional airfoil sections which are optimized using their local flight conditions.

1.5.3 Aerodynamic Shape Optimization

Aerodynamic shape optimization at both the preliminary and the intermediate stages of design remains a highly complex topic. Aerodynamic analysis using numerical methods is an inherently computationally expensive process and is prone to slight errors. Evolutionary methods such as genetic algorithm simply require far too many function evaluations to be a feasible method. Additionally, gradient based methods such as SLSQP can be seen as unreliable due to high degrees of dimensionality and inherent solution noise. Luckily recent advancements in machine learning based optimization methods such as Bayesian optimization allow for converged solutions in a fraction of the number of function evaluations through the use of probabilistic surrogate models. This allows for the derivation of an optimized aerodynamic solution at a very low computational cost while minimizing the effect of noise generated from the inherent errors generated by the required estimation methods. The machine learning based methodology used in this project are discussed in detail in Chapter 2.

1.6 Objective

The overarching objective of this research is to conduct a comparative study on the design and analysis of regional to medium sized hydrogen powered commercial airliners. In order to achieve this, a comprehensive set of analysis tools and methods are developed and implemented. Itemized, the main objectives are as follows.

1. Develop a software package capable of rapid design, analysis, and optimization of a given configuration of aircraft
2. Analyze the design and feasibility of a hydrogen combustion powered aircraft and perform a full preliminary optimization on the selected configuration
3. Develop a system architecture and analysis methodology for hydrogen fuel cell powered aircraft
4. Optimize and analyze configurations of hydrogen fuel cell powered aircraft and compare those results to hydrogen combustion powered configurations
5. Fully optimize the wing of both configurations including variables such as airfoil and twist distribution
6. Validate the results with RANS CFD simulations

Item 1 in the above list must be achieved first in order to develop a software capable of accurately predicting the range and overall aerodynamic performance of an arbitrary configuration of aircraft. This allows for the rapid testing of several configurations of aircraft in which the geometric design parameters, mission profile, passenger count, etc. can be altered. This code will operate by using a conjunction of empirical methods for an aircraft's structural weight, parasite drag, wave drag, etc. along with rudimentary simulation results to predict its overall aerodynamic performance. Development of this software package along with various validation cases is outlined in Chapter 2.

Using this code, item 2 in the above list can be achieved by analyzing a hydrogen combustion powered medium range commercial aircraft configuration. The proposed configuration of aircraft is based on the performance of the Boeing 737-800. Chapter 3 discusses in detail this analysis along with the aerodynamic shape optimization of the configuration's wing and fuselage.

Next, a hydrogen fuel cell powered configuration is examined. Chapter 4 covers the design of an electrified, hydrogen fuel cell powertrain for use on an aircraft. The methodology used to analyze the performance of this drivetrain is implemented into the previously discussed conceptual design code and a test case is run on a commuter sized aircraft for validation.

Chapter 5 covers the results obtained by analyzing the performance of a hydrogen fuel cell powered aircraft. First, a regional size airliner is analyzed with performance estimates of different components representing different technological levels in the near future to analyze the technological readiness of such a design. Next, the efficiency of hydrogen fuel cell powered configurations is compared to that of hydrogen combustion powered configurations.

Chapter 6 covers the methodology used for airfoil optimization. This includes the automation of the CFD airfoil analysis process and the implementation of machine learning based methods to reduce the naturally high computational cost and errors inherent in this methodology. Chapter 7 covers the process of applying these airfoil optimization methods to a 3D swept tapered wing. This involves splitting the wing into several 2D wing stations and optimizing the airfoil at each station using the full RANS CFD simulations. A fully optimized 3D wing is generated and tested to validate the estimation methods used throughout the dissertation. Finally, Chapter 8 summarizes the key results of the research and provides suggestions for future work.

Chapter 2: WUADS – An Aircraft Conceptual Design Tool

2.1 Introduction

As mentioned in Chapter 1, the large number of configurations to be tested as well as the complex, time consuming nature of aerodynamic performance analysis required the development of a whole new analysis tool specifically made for the task at hand. For this reason, the WUADS (Washington University Aircraft Design System) code was developed. WUADS is a model based conceptual design software which employs empirical and panel methods to estimate aircraft performance values such as weight, range, and stability. Alongside the main WUADS code, another code referred to as WuFoil was developed for use in airfoil design and optimization. This code can be used beyond the stage of preliminary design to achieve a highly detailed, fully designed 3D wing. The development of WuFoil will be examined further in Chapter 6. The following section describes in detail the methodology and implementation strategy employed in WUADS. To find the full versions of these codes, the reader is referred to Refs. [18, 19]. It should be noted that WUADS in its current state works for aircraft designed for subsonic to transonic flight regimes and is not configured to work for the design of a supersonic aircraft.

2.2 Methodology

WUADS was designed as a model based conceptual design tool which employs a blend of empirical methods and low fidelity simulation methods to estimate aircraft performance. A simplified diagram of the structure of the WUADS code is shown in Fig. 2.1. Using this methodology, an aircraft can be input using its list of components, geometric design variables, mission requirements, and mission profile and have the full analyses run to determine its range, overall weight, stability and control, etc. This code was designed to be simple, efficient, and automated to allow for the rapid testing of arbitrary aircraft configurations, allowing for the use of optimization algorithms. The following section provides details of the methodology and implementation strategy for this code.

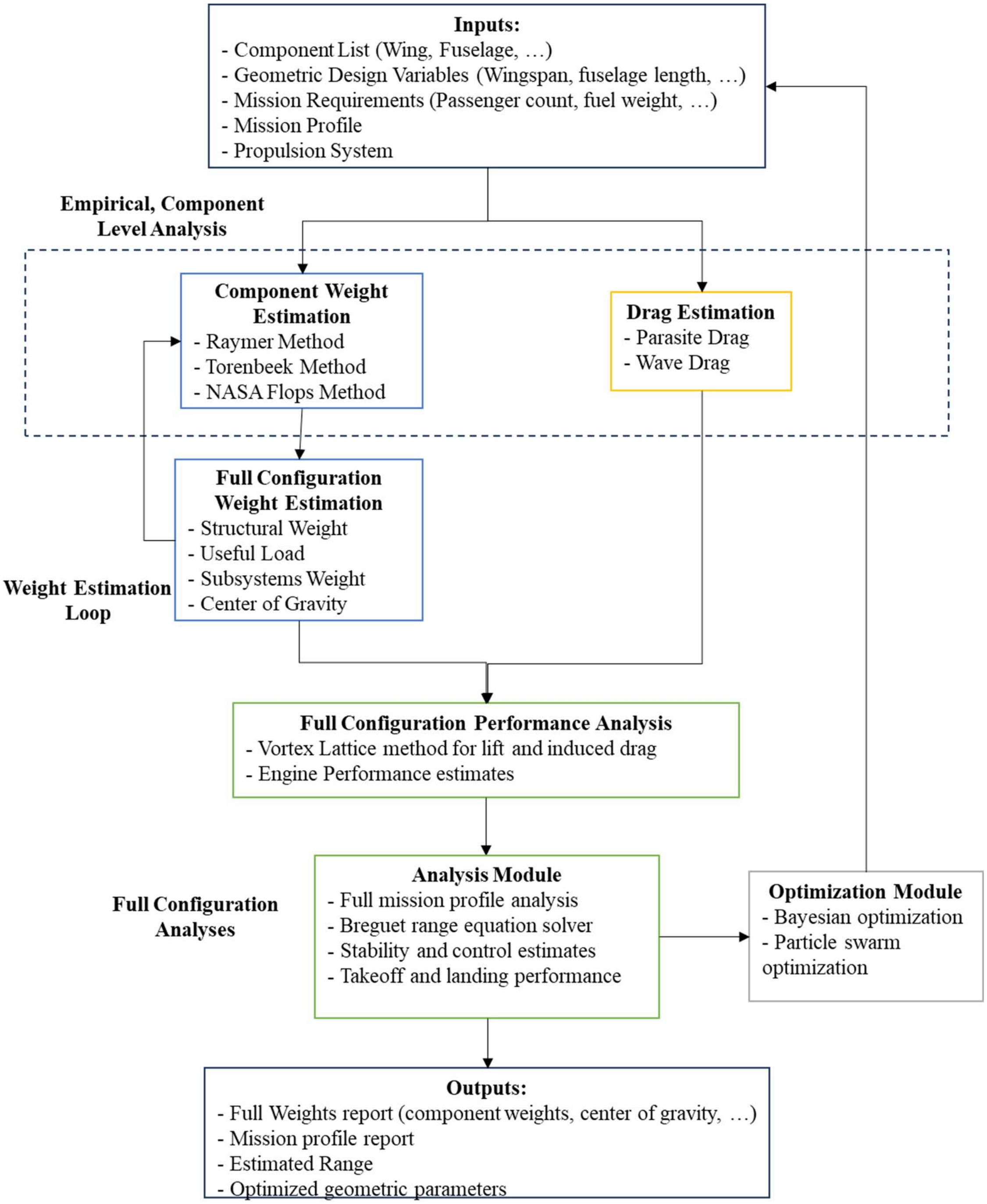

Figure 2.1 WUADS code structure

2.2.1 Weight Estimation

To estimate an aircraft's overall structural weight, WUADS uses a weighted average of three separate estimation methods: Raymer [20], Torenbeek [21], and NASA Flops [22]. These weight estimation methods all work on a component level. In WUADS, this works by calculating the weight of each input component and applying averaging according to a weighted average. The weights used for these component averages were determined to maximize the estimation accuracy using the modern construction materials. These weight values were found through extensive testing on several configurations. To understand the component level weight estimation methods, see Appendix A. Several component weight estimates in each utilized method require an input of the aircraft's takeoff gross weight, meaning that the code must use an iterative loop to converge on the accurate component and gross takeoff weights. Beyond the input aerodynamic components, the WUADS code estimates the weight of various subsystems such as the landing gear, air conditioning, avionics, etc. using similarly described methods. With these complete aircraft weights buildup methods along with the useful input loads such as passengers, cargo and fuel, the overall structural weight and takeoff gross weight of the aircraft can be calculated. The center of gravity can then be calculated using the aircraft's complete moment of inertia.

2.2.2 Vortex Lattice Method

Vortex Lattice Method is a low fidelity CFD method used in the conceptual design process to provide computationally cheap aerodynamic performance characteristics of lifting surfaces. The vortex lattice method works by discretizing aerodynamic surfaces into a grid of panels which are modelled as horseshoe vortices whose vortex strength can be calculated. This method allows for the estimation of velocity and pressure distributions on the surface along with wake and downwash characteristics, and subsequently allows for the calculation of total aerodynamic forces exerted on the aircraft. This method is widely used in both industry and academia since it provides reasonably accurate results at a relatively low computational cost. The vortex lattice method is limited mainly by its assumption of incompressible and inviscid flow. The assumption of incompressible flow can be rectified slightly by the use of the Prandtl-Glauert compressibility transformation; however the transonic effects cannot be modeled using this method. The assumption of inviscid flow means that the drag results from the vortex lattice method would strictly represent the induced drag, meaning that the parasite drag must be calculated using separate methods.

The selected flow solver used for the conceptual design process is Athena Vortex Lattice (AVL), an extended vortex lattice method-based solver developed by Mark Drela of MIT which has been widely used and validated in the past [23]. AVL allows for the estimation of aerodynamic forces, static and dynamic stability, control surface effectiveness, lift distribution, Oswald efficiency etc. about a given configuration of aircraft at specified flight characteristics. Despite the inherent limitations of the vortex lattice method, these estimates have been shown to be reasonably accurate when compared to real world data.

2.2.3 Drag Estimation Methods

Due to the inherent limitation of the vortex lattice method since it assumes an incompressible inviscid flow, separate methods must be used to predict compressibility and viscous effects on the aircraft. In preliminary design, parasite drag can be estimated at a component level using the empirical methods. Similar to the weight estimation methods, the parasite drag can be estimated from a component buildup, as described below in Eq. (2.1) [20, 24]. Note that for all calculations in the WUADS code which uses atmospheric conditions, the 1976 US Standard Atmospheric model is used [25].

$$C_{D_0} = \sum C_{D_{0_c}} Q_C + C_{D_{misc}} + C_{D_{wave}} \tag{2.1}$$

The aircraft's overall parasite drag, C_{D_0}, can be calculated using the sum of each component's individual parasite drag, indicated by the subscript 'c'. In this method, each component's drag contribution is estimated as its parasite drag coefficient, $C_{D_{0_c}}$, multiplied by an interference factor, Q_c. Added to the component drag buildup is any additional miscellaneous drag value, $C_{D_{misc}}$, and the wave drag coefficient, $C_{D_{wave}}$. Using this method, the main task becomes to find each component's individual parasite drag coefficient, which is calculated as follows.

$$C_{D_{0_c}} = C_f FF \frac{S_{wet}}{S_{ref}} \tag{2.2}$$

where C_f represent the skin friction coefficient, FF represents the component's form factor, and $\frac{S_{wet}}{S_{ref}}$ represents the ratio of the components wetted area to the reference wing area. The skin friction coefficient can be estimated simply using the equations for a flat plate described by Raymer [20].

$$C_{f_{laminar}} = \frac{1.328}{\sqrt{Re}} \tag{2.3}$$

$$C_{f_{turbulent}} = \frac{0.455}{(\log_{10} Re)^{2.58}(1 + 0.144M_\infty^2)^{0.65}} \tag{2.4}$$

$$C_f = L_{\%} C_{f_{laminar}} + (1 - L_{\%}) C_{f_{turbulent}} \tag{2.5}$$

The skin friction coefficient for the laminar and turbulent regions of the flow are found separately, then the overall skin friction coefficient is determined using the percentage of laminar flow over the component, $L_{\%}$. Several estimation methods have been published for the form factor by Raymer [20] and Shevell [26]. In both methods, components are split into bodies and wings.

2.2.3.1 Bodies

Fuselages, nacelles, and other slim bodies are considered as individual components. The main driving factor for form factor in both methods is the body's fineness ratio, l/d. Shevell's method to estimate the form factor of a body is as follows [26]:

$$FF_{body} = 1 + \frac{2.8}{(l/d)^{1.5}} + \frac{3.8}{(l/d)^3} \tag{2.6}$$

In Raymer's method, the form factor is given by:

$$FF_{body} = 1 + .0025(l/d) + \frac{60}{(l/d)^3} \tag{2.7}$$

In testing, both methods were found to be accurate in the case of nacelles and externally mounted slender bodies, however both struggled in predicting the fuselage's drag coefficient with fineness ratios outside the range between 8 and 10. For this purpose, an improved form factor estimation proposed by Götten et al. is used specifically for the fuselages [27].

$$FF_{fuselage} = cs_1(l/d)^{cs_2} + cs_3 \tag{2.8}$$

$$cs_1 = -0.825885(2r/w) + 4.0001 \tag{2.9}$$

$$cs_2 = -.340977(2r/w)^{7.54327} - 2.27920 \tag{2.10}$$

$$cs_3 = -0.013846(2r/w)^{1.34253} + 1.11029 \tag{2.11}$$

where r is the fuselage's average diameter and w is the fuselage's width.

2.2.3.2 Wings and Tail Surfaces

In estimating a wing's or tale surface's parasite drag and wave drag contribution, it is necessary to split the wing into several strips, each of which can be treated as its own separate component. The total wing parasite drag is then calculated as follows.

$$C_{D_{0_{wing}}} = \sum C_{f_c} FF_c \frac{S_c}{S_{ref}} \tag{2.12}$$

where FF_c is the strip's local form factor, C_{f_c} is the strips skin friction coefficient, calculated by Eq. (2.5), S_c is the strip's planform area and S_{ref} is the total wing area. Shevell's method for estimating the form factor of each strip is as follows [26].

$$FF = 1 + \frac{(2 - M_\infty^2)\cos\Lambda_{c/4}}{\sqrt{1 - M_\infty^2 \cos^2\Lambda_{c/4}}}\left(\frac{t}{c}\right) + 100\left(\frac{t}{c}\right)^4 \tag{2.13}$$

where M_∞ represents the freestream Mach number, $\Lambda_{c/4}$ is the quarter chord sweep angle, and $\frac{t}{c}$ is the average airfoil thickness ratio of the wing. Raymer's method for estimating the strip's form factor is as follows [20].

$$FF = \left[1 + \frac{.6}{(x/c)_m}\left(\frac{t}{c}\right) + 100\left(\frac{t}{c}\right)^4\right]\left[1.34 M_\infty^{0.18}(\cos\Lambda_m)^{.28}\right] \tag{2.14}$$

where $(x/c)_m$ is the normalized x coordinate of the point of maximum thickness on the strip's representative airfoil and Λ_m is the sweep angle connecting these points.

WUADS uses a similar strip described by Gur et al. to solve for a transonic wing's wave drag contribution [24]. Note that in The WUADS code, wave drag is assumed to be only produced by the wing. In this method, it is important to first find each strip's critical Mach number, M_{cr}, defined as the Mach number at which the sonic point first appears on the wing. This can be found using the following relation.

$$M_{cr} = M_{DD} - .1077 \tag{2.15}$$

where M_{DD} is the drag divergence number defined as the Mach number at which the drag increase due to shock wave formation reaches 0.002. The drag divergence Mach number can be estimated using the following equation [28].

$$M_{DD}\cos\Lambda_{0.5} + \frac{C_l}{10\cos^2 \Lambda_{0.5}} + \frac{t/c}{\cos\Lambda_{0.5}} = \kappa_A \tag{2.16}$$

where $\Lambda_{0.5}$ is the sweep angle at the half chord, C_l is the lift coefficient, and κ_A is the Korn factor which is equal to 0.95 for supercritical airfoils and 0.87 for conventional airfoils. Once the critical Mach number is calculated, the following equation can be used to estimate the wave drag on each strip.

$$C_{d_{wave}} = \begin{cases} 0 & M \leq M_{cr} \\ 20(M_\infty - M_{cr}) & x \geq 0 \end{cases} \tag{2.17}$$

The wing’s wave drag coefficient can then be calculated using the same summation for each strip given in Eq. (2.12).

2.2.3.3 Interference Factors and Miscellaneous Drag

The last remaining values needed to calculate each component’s drag contribution is the interference factor. For a general case, the following interference factors are used; however, these values can be altered freely. A nacelle or any wing or fuselage mounted component experiences very clear interference effects and thus have an interference factor of 1.25-1.5, depending on the distance away from the component they are mounted on. A fuselage with mounted landing gear can be assumed to have an interference factor of about 1.07. Lastly, both horizontal and vertical tail surfaces can be assumed to have an interference factor between 1.03 and 1.05 [20].

2.2.4 Propulsion Performance Estimation

Estimating the propulsion performance is an incredibly crucial step in the process of analyzing an aircraft configuration’s performance and is likely the largest source of uncertainty in the entire range predicting process in WUADS. The source of this uncertainty is the fact that the engine performance data is often classified as proprietary by manufacturers, meaning that the values used for maximum thrust and specific fuel consumption must be acquired either through empirical analysis or through complex simulations. To account for this uncertainty, WUADS has considered two available methods with varying levels of fidelity.

The first method, described by Howe in his book “Aircraft Conceptual Design Synthesis,” works using a set of 3 input variables, the engine’s bypass ratio, R, maximum thrust at sea level, T_{max}, and specific fuel consumption at cruise conditions, c [29]. In this method, the maximum thrust available and specific fuel consumption for an engine is scaled by the aircraft’s current altitude, H, and Mach Number M_∞. The equation used to scale the maximum thrust available is as follows. Note that this section applies specifically to turbofan engines.

$$\frac{T_{available}}{T_{max}} = (k_1 + k_2 R + (k_3 + k_4 R) M_\infty)\sigma^S \tag{2.18}$$

where σ represents the density ratio between the ambient density and the density at sea level, calculated using the 1976 US Standard Atmosphere model [25]. The constants k_{1-4} and S in this model are defined in Table 2.1. Note that the constant S is used only at altitudes below 36000 ft, above this altitude S is always equal to 1.

Table 2.1 Constants used in Howe's Engine Performance Estimates [29]

Bypass Ratio, R	Mach Number, M_∞	k_1	k_2	k_3	k_4	S
<1	<0.4	1.0	0	-0.2	0.07	0.8
	0.4-0.9	0.856	0.062	0.16	-0.23	0.8
3-6	<0.4	1.0	0	-0.6	-0.4	0.7
	0.4-0.9	0.88	-0.016	-0.3	0	0.7
>8	<0.4	1.0	0	-0.595	-0.03	0.7
	0.4-0.9	0.89	-0.014	-0.3	0.005	0.7

The specific fuel consumption, c, can then be calculated using the following equation.

$$c = c'(1 - 0.15R^{0.65})[1 + 0.28(1 + 0.063R^2)M_\infty]\sigma^{0.08} \tag{2.19}$$

This specific fuel consumption represents the fuel used at the maximum thrust value calculated in Eq. (2.18). To scale this specific fuel consumption to represent partial power usage, the following equation is used.

$$c_{OD} = c\left(1 + 0.01\left(\frac{T}{T_{OD}} - 1\right)\right) \tag{2.20}$$

where c_{OD} and T_{OD} represent the off-design conditions used at the partial required thrust value. This model has been shown to be fairly accurate for the areas of interest and has the benefit of requiring very little knowledge beforehand [30]. That is the purpose of its inclusion in the WUADS code, to provide a semi accurate engine performance estimation very early in the design process. However, in testing on various configurations, this model was not seen to be accurate enough for detailed analysis. For this purpose, a higher fidelity model was used.

One such higher fidelity engine estimation method is described by Mattingly [31]. In this method, the thrust and fuel consumption available are estimated based on the component efficiencies and performance with the input being the temperature and pressure at different parts of the engine. This method is certainly accurate enough to provide detailed results for the range predictions, however, is not yet implemented in WUADS in its current state. There are currently plans to implement such a model, however, currently estimates in WUADS are based on a pre calculated data set using Mattingly's equation. This dataset is meant to represent a general model of a modern turbofan engine under typical conditions. Note that this method has also been employed as well by Raymer to great effect [20]. This general turbofan model as well as the method used to scale results to the user's desired case can be seen in Appendix B. Using these results should give a fairly accurate representation of the uninstalled thrust and specific fuel consumption at a given flight condition; however, the specific fuel consumption estimate must still be altered to represent the partial power usage. This can be accomplished using the following equation.

$$\frac{c}{c_{max}} = \frac{0.1}{T/T_{max}} + \frac{0.24}{(T/T_{max})^{0.8}} + 0.66(T/T_{max})^{0.8} + 0.1M_{\infty}\left(\frac{1}{T/T_{max}} - (T/T_{max})\right) \quad (2.21)$$

where c_{max} and T_{max} represent the conditions at maximum available thrust. With these methods employed, an accurate estimate for fuel consumption and thrust available can be obtained for a turbofan engine given the input values for thrust and fuel consumption at both takeoff and climb conditions. Additionally, WUADS has the ability to implement custom engine performance estimation methods. This is useful in cases for which the performance code such as NASA's Numerical Propulsion System Simulation (NPSS) has already been implemented with engine performance already determined. In fact, a majority of the cases presented in the following section used scaled results obtained through NPSS simulations.

2.2.5 Breguet Range Equation

The previously described estimation methodology allows for an arbitrarily input aircraft to be automatically analyzed at any set flight conditions. The aircraft performance then can be analyzed at several points throughout its mission profile to determine the maximum range. A typical mission profile for a commercial aircraft consists of the following stages: taxi, takeoff, climb, cruise, descent, and landing. Additional, reserve fuel must be held for a missed approach scenario, consisting of an additional climb, loiter, descent, and landing.

The basic form of the Breguet Range equation is as follows.

$$R = \frac{V}{c}\frac{L}{D}\ln\frac{W_i}{W_{i-1}} \tag{2.22}$$

where R represents the range of a mission segment, V represents the velocity, c is the specific fuel consumption, $\frac{L}{D}$ represents the lift to drag ratio, and $\frac{W_i}{W_{i-1}}$ represents the segment's weight fraction, defined as the aircraft's weight at the end of the mission segment divided by the weight at the start of the segment. The taxi stage of the mission profile is simply modeled assuming that the specific fuel consumption is 1.5 times the value at maximum thrust at sea level. Takeoff then is modelled using the engine performance estimates at maximum thrust. Given that the specific fuel consumption is defined as the ratio of the thrust produced to fuel consumption, the fuel burnt during these segments can simply be represented as follows.

$$W_{fuelburnt} = cTd \tag{2.23}$$

The fuel fraction spent during the climb section requires an energy analysis to account for the changes in altitude and velocity. The resultant equation, provided by Raymer, is shown below [20].

$$\frac{W_i}{W_{i-1}} = \exp\left[\frac{-c\Delta h_c}{V\left(1-\frac{D}{T}\right)}\right] \tag{2.24}$$

$$\Delta h_c = \Delta\left(h + \frac{1}{2g}V^2\right) \tag{2.25}$$

where *h* represents the altitude, *g* represents the gravitational constant (32.2 in imperial units), and *V* represents the velocity. For aerodynamic and propulsive estimates, the models are evaluated at a weighted value 2/3 of the way through the climb. This equation is not meant to represent large changes in altitude and velocity, meaning the climb must be split into segments for an accurate analysis. For a commercial airliner cruising at 35,000 ft at a Mach number of 0.8, this typically requires 3-5 different analysis points for the climb segment.

The range of the climb segment is typically not known and often must be solved for. For this purpose, an inverse process is used in which the weight fraction of the taxi, takeoff, and climb segments are solved for and then the mission profile is analyzed in reverse order. It is assumed that 5% of the fuel is saved for reserve fuel. The landing segment is typically represented by a constant very small weight fraction (~0.997). The descent segment is simply calculated using idle power settings. The rate of descent can be calculated using the following equation

$$R_{descent} = V\left(\frac{T}{W}\right) - \frac{\rho V^3 C_{D_0}}{2\left(\frac{W}{S}\right)} - \frac{2K}{\rho V}\left(\frac{W}{S}\right) \tag{2.26}$$

$$K = \frac{C_{D_{induced}}}{C_L^2} \tag{2.27}$$

Using the rate of descent and the idle engine performance, the fuel burnt can be calculated using Eq. (2.23). The weight fraction of the required loiter segment can be calculated using Eq. (2.22). Combining these methods, the fuel at the beginning and end of the cruise segment is known and the resultant range in the cruise section can be calculated using Eq. (2.22) as well. This gives a full estimate of the aircraft's maximum range with a given fuel weight.

2.3 Code Structure

WUADS is designed with an object-oriented framework with the top-level class being the aircraft. The aircraft object contains all top-level values such as the weight, aerodynamic characteristics, engine performance estimates, etc. Also stored in the aircraft class are lists of components and analyses.

Components in WUADS are broken up into 3 categories: aerodynamic surfaces, bodies, and subsystems. Aerodynamic surfaces represent the wing and tail surfaces, bodies are the fuselage and nacelle, and the subsystems are any component on the aircraft which does not directly contribute to the aerodynamic performance, such as the landing gears or air conditioning. Each component has inscribed methods to set the weight, parasite drag, wave drag, and center of gravity, all of which were explained in the previous section. The top-level aircraft class has methods to analyze the full drag and weight characteristics of each component. Additionally, each component is inscribed with a method called "update_component" which works to change features of the component; it should be accessed through the aircraft class to update the aircraft's overall characteristics. This function is highly useful in optimization problems. Range estimation analysis is structured in a similar fashion, with individual mission segments represented by the class objects with a method in the aircraft class which uses the methods described in section 2.2.5 to estimate the maximum range.

2.4 Bayesian Optimization

With the automation of the entire process of geometry creation and analysis, the application of optimization algorithms becomes possible. It consider the high level of dimensionality, the black box function nature of the analysis, and the computational expense of the objective function. Certain gradient-based optimization methods such as SLSQP and particularly SNOPT have been applied to similar problems with good results in the past; however, the gradient based methods are prone to finding local minimums and require a nearly optimized set of design variables to produce accurate results [32]. The overall computational time required for the wing optimization can be reduced by splitting the problem into multiple sub-problems; however, the aerodynamic shape optimization is a highly complex field with several unpredictable coupling effects skewing the results. For example, optimizing a wing planform shape alone might not produce the same results as running an optimization problem with the wing's planform area, sweep angle, and wingspan. To alleviate these issues while still maintaining high computational efficiency, Bayesian optimization was used in this research. In particular, two separate python libraries were utilized, the scikit-opt's gp_minimize algorithm [33] and the library titled Bayesian Optimization [34], although the latter was primarily used for the airfoil optimization problems which are described later in the dissertation.

The Bayesian optimization is a gradient free, surrogate model-based optimization algorithm. The Bayesian optimization works to optimize a function using the following method. A function $f(x)$ is first sampled at several points across the design space X over which a probabilistic model is estimated. Using this probabilistic model an acquisition function is employed to determine the expected optimum value and the most beneficial point to evaluate to improve the existing model. Using this newly derived datapoint, the model is improved and reevaluated [35].

Typically, in the Bayesian optimization a Gaussian process is employed. A Gaussian process is a powerful regression tool in which a multivariate Gaussian distribution is fit around the given function values by use of a mean function, μ, and a covariance matrix, Σ. The covariance matrix of a multivariate Gaussian distribution is structured such that the term Σ_{ij} corresponds to the correlation between the two random function evaluations i and j. The ultimate goal of the Bayesian Optimization is to optimize the accuracy of this distribution with respect to the evaluated training data by altering the hyperparameters of the covariance matrix while simultaneously searching for an optimum point [36]. There are a number of ways in which to tune these hyperparameters using the given kernels, such as the commonly used automatic relevance determination method [35]. To efficiently tune the hyperparameters of the Gaussian process, evaluation points must be selected strategically through acquisition functions such as Expected Improvement or Probability of improvement in which the selected next point is evaluated by analyzing the current model and selecting points at which the best function value is likely to improve.

For further improvements in the computational efficiency, a domain reduction scheme is a useful tool in the implementation of the Bayesian optimization in cases with particularly expensive function evaluation with ill-defined bounds and the potential of failed simulation. When generating random data points for a complex aerodynamic analysis, infeasible solutions may result in the solver resulting in divergence and therefore not returning a function value. This is particularly an issue in airfoil optimization where infeasible airfoils will be unable to converge to a RANS CFD solution, as would be be seen in Chapter 6. This situation drastically increases the run time of the optimization since not only useless simulations are being run, the Gaussian Prior distribution employed in the Bayesian optimization experiences unexpectedly noisy results. Using domain reduction, the bounds of the problem can be dynamically shifted to ensure a feasible design space. The specific domain reduction scheme used is described by Stander et. al in Reference [37]. In practice, this method works as follows. The optimization problem is run for the initial samples, after which an initial optimum point is estimated. Subsequently after each function call, for each variable the bounds are then reevaluated using a contraction parameter which is determined based on the optimum value's deviation from the center of that variable's domain. This allows the bounds to shift and contract, further converging on areas of the design space which are known to be both feasible and optimal. This process is seen to drastically reduce run time and was employed in all subsequent airfoil optimizations

2.5 Validation

Several validation cases were run using WUADS to ensure accuracy, five of which are presented below. These cases include the Boeing 737-800 [38], the Boeing 717-200 [39], the Gulfstream g650er [40], the Bombardier CRJ-200er [41], and the Boeing Sugar-Volt [7]. Some of the key characteristics of these test cases are given in Table 2.2.

Table 2.2 Characteristics of 4 WUADS tests cases

	Passengers	Maximum Fuel (lbs.)	Maximum Takeoff Weight (lbs.)	Design Range (nmi)	Cruise Altitude (ft)	Cruise Mach No.
G650	19	44200	99600	7000	41000	0.85
717-200	134	24609	110000	1430	35000	0.77
737-800	189	46000	174200	2935	36000	0.789
Sugar Volt	154	14000	150000		40000	0.7

Both twin engine, single aisle commercial aircraft, the 737-800 and the 717-200 are critical to this project since these are the configurations on which the baseline hydrogen combustion aircraft configuration and the hydrogen fuel cell aircraft configuration respectively are based on in this study. In fact, the 737-800 is the configuration for which the WUADS code was originally designed. For this reason, the Gulfstream G650 and the Bombardier CRJ-200ER are selected to determine the WUADS code's ability to analyze the smaller aircraft configurations, a task which would be crucial in designing a hydrogen fuel cell based aircraft configuration. Finally, the Sugar Volt is an experimental truss braced wing configuration tested by Boeing as a part of its Subsonic Ultra Green Aircraft Research (SUGAR). This configuration is selected to evaluate the WUADS ability in using custom components outside the standard tube and wing model. The truss in this case is modelled as a wing with its weight scaled to match the results of the Sugar Volt project [7]. Note that the range estimates of this configuration are not considered since the project uses a hybrid electric propulsion system making it difficult to achieve the specific fuel consumption estimates. Instead, aerodynamic performance results are compared to the reported lift to drag ratio at cruise.

2.5.1 Weights and Range Estimates

Each configuration was tested using WUADS to analyze its maximum takeoff weight and range at maximum loading conditions. These results are given in Table 2.3.

Table 2.3 Calculated values from WUADS vs published values for range and weight predictions.

	Takeoff Gross Weight (lbs.)		Range (nmi)	
	Calculated	Published	Calculated	Published
g650	98291	99600	6667.8	7000
CRJ-200er	51118	51000	1318	1305
Boeing 717-200	110754	110000	1467	1430
Boeing 737-800	175970	174200	2962	2935
Sugar Volt	148972	150000		

In Table 2.3, WUADS' weight estimation in all the four cases can be seen to be very accurate, within about 1.5% of the real-world values. Range estimates however are slightly more off. In particular, the range is underpredicted for g650 by about 5%. It is possible that the actual g650 has certain range increasing high lift devices, or a higher percentage of laminar flow than estimated by WUADS, or the mission profile used was wrong; however, it is difficult to determine the source of this discrepancy. The range predicting capability of WUADS for smaller aircraft configurations can still be considered as relatively accurate based on the calculations for the CRJ-200er case. The weight estimation for the Sugar Volt is within 1% of the published values. The lift to drag ratio at cruise for this case was calculated by WUADS to be 22.97 compared to the published value of 23.047 [7]. From these results it can be concluded that the weight and range estimates computed by the WUADS are highly accurate and are applicable to a wide range of aircraft configurations, from smaller passenger aircraft to experimental truss braced wing configuration.

As an additional test of the WUADS' range prediction capability at off-design conditions, a total of 27 different cases were run for the 737-800 by varying the fuel weight and the cargo. The result of these cases are shown in Fig. 2.2.

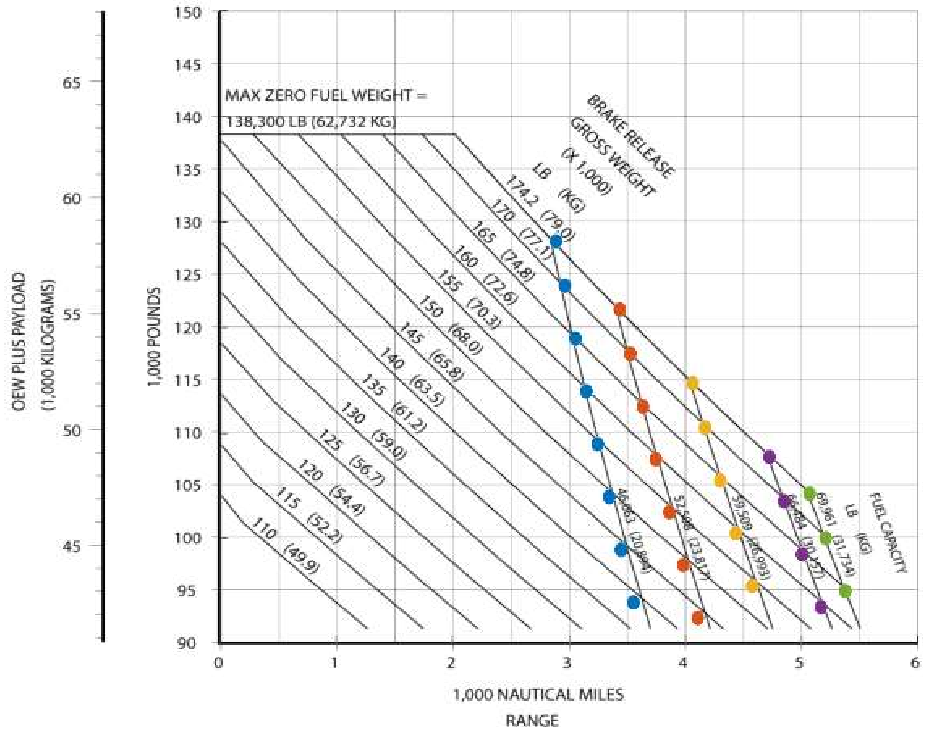

Figure 2.2 Boeing's published values vs. WUADS estimated values for the range of Boeing 737-800 [38]

The largest deviation from the expected value occurs at a gross take-off weight of 135,000 pounds and a fuel capacity of 46,063 pounds where WUADS predicted a range of 3554 nmi compared to the published value of 3625 nmi. All other tested points fall well within this 2% error.

2.5.2 Optimization

To validate the optimization capabilities of WUADS along with the Bayesian optimization method mentioned in section 2.4, an optimization case was run on the wing planform shape of the Boeing 737-800. In this optimization problem, the fuselage and tail surface geometries were held constant. The performance of the CFM56-7B24 engine was estimated using the methods discussed in section 2.2.4. The aspect ratio of the wing was held constant at 9.45 to maintain constant wing loading at takeoff and landing. This resulted in only three design variables required to fully describe the trapezoidal reference wing: quarter chord sweep, taper ratio, and wingspan. The quarter chord sweep and taper ratio were both constrained simply by considering the feasible values leaving a very open design space. The wingspan however was constrained to a maximum of 112.5 ft in compliance with the relevant ICAO Aerodrome Reference Code 3C [42]. Note that this wingspan constraint can be bypassed with the use of a wing folding mechanism similar to that of the Boeing 777; however, this technology is not featured on the 737 and therefore was not employed in this optimization case. It is assumed that the real-world values in this case roughly represent the true aerodynamically optimized values.

When the three variable Bayesian optimization case was run, the values were found to converge rapidly. As shown in Fig. 2.3, 300 total function evaluations were run; however, the results can be seen to converge around iteration number 80.

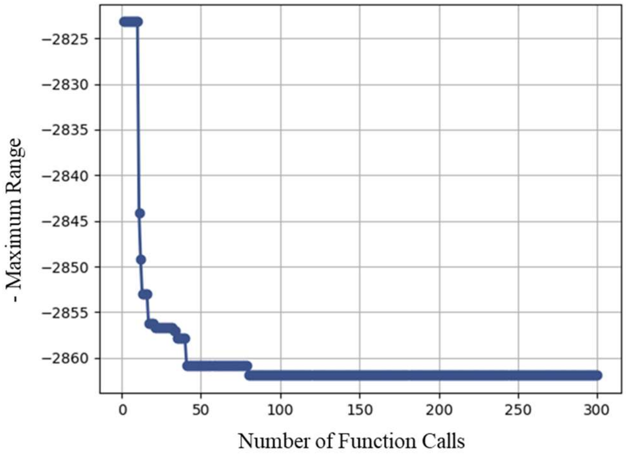

Figure 2.3 Convergence history of the 737-800 wing shape optimization problem

As given in the Table 2.4, the results produced by the optimization can be seen to be highly accurate to the real world published values for the 737-800.

Table 2.4 Optimized wing shape results vs. real world values for the Boeing 737-800

	Taper Ratio	c/4 Sweep Angle (deg)	Wingspan (ft)
Optimization Results	0.153	25.02	112.5
Boeing 737-800	0.159	25.3	112.5
Percent Difference	3.5%	1.1%	0.0%

In Table 2.4, the predicted optimum sweep angle and the wingspan both can be seen to match their corresponding real-world values to a high degree of accuracy. The code is found to underpredict the taper ratio slightly and it is unclear why; however, the margin of error is still relatively small. It is possible that the real-world values include effects other than pure aerodynamic optimization.

Chapter 3: Hydrogen Combustion Powered Aircraft

The first case run for a hydrogen powered aircraft was on a medium range hydrogen combustion powered configuration designed to match the passenger count and maximum range of the Boeing 737-800. Two separate configurations were considered, one with internal pressurized cryogenic hydrogen fuel tanks, and the other with external tanks stored under the wings. This chapter provides the details of the design and analysis of these two configurations.

3.1 Methodology

Both modified Boeing 737-800 configurations with internal and external LH2 tanks were tested using the WUADS software. The mission profile was set to match that of the Boeing 737-800. This input mission profile is given in Fig. 3.1.

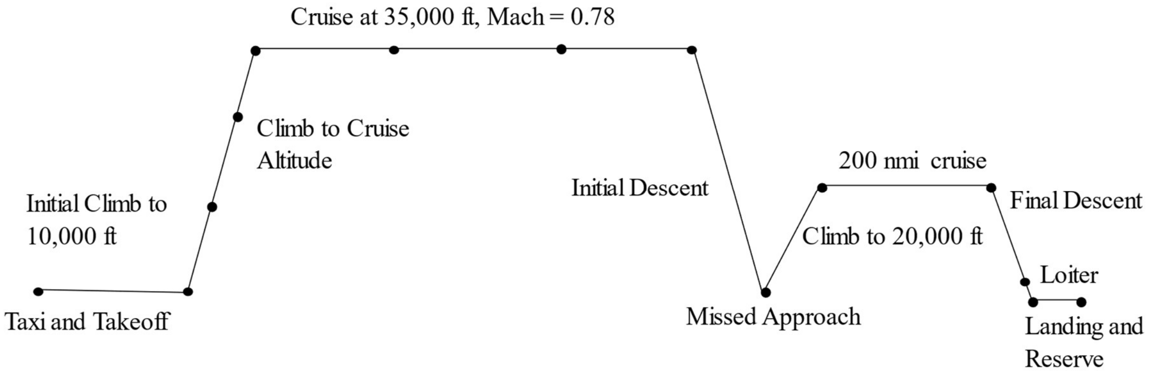

Figure 3.1 B 737-800 mission profile used for the analysis of aircraft configuration with hydrogen combustion.

In the mission profile in Fig. 3.1, a 10-minute taxi is assumed followed by the takeoff and an initial climb at the maximum rate of climb to 10,000 ft. Next, two evenly spaced climb sections are considered assuming that the plane is flying at the optimum rate of climb. The cruise section is split into 3 separate segments to model various conditions experienced by the plane as it loses fuel weight. Next is the initial descent followed by an assumed missed approach. The reserve fuel is defined as the fuel required to climb back to 20,000 ft, cruise for 200 nautical miles, descend, loiter for 30 minutes, and land with 5% reserve fuel left. Note that this is a slightly simplified model of a real-world mission profile; however, it should yield fairly accurate results. A value of 17,000 lbs. of hydrogen fuel was used for testing both configurations. This value was derived simply from comparing the energy density of hydrogen fuel and jet fuel.

Engine performance estimates for the hydrogen combustion powered turbofan engine were derived from a model created in the NPSS software. For more information on how this model was derived, see Ref. [43]. This studied showed a 64% improvement in specific fuel consumption compared to a similarly modeled jet engine. The results from this study were used alongside the weighted bilinear interpolation methods mentioned in section 2.2.4 for range prediction of a hydrogen combustion powered aircraft. Special attention must be given to the design of cryogenic liquid hydrogen fuel tank to minimize fuel lost due to boil-off. Previous studies on the LH2 fuel tank design have led to a design of both spherical and cylindrical fuel tanks with hemispherical caps with 4.5 inches of foam insulation and aluminum skin [44, 45]. The material properties of this tank are used in estimating the overall added structural weight.

3.2 External Fuel Tank Configuration

3.2.1 Design

The external fuel tank configuration was based on the geometry of the Boeing 737-800 with hydrogen fuel tanks mounted on the wing. A few key changes had to be made, however. First, it was assumed that the engines would need to be shifted to be mounted at the aft of the fuselage since having both the fuel tanks and the engines mounted on the wing would likely cause structural and aeroelastic problems. To accompany this change, a T-tail configuration was used. A schematic of the B 737 based external tank configuration is shown in Fig. 3.2.

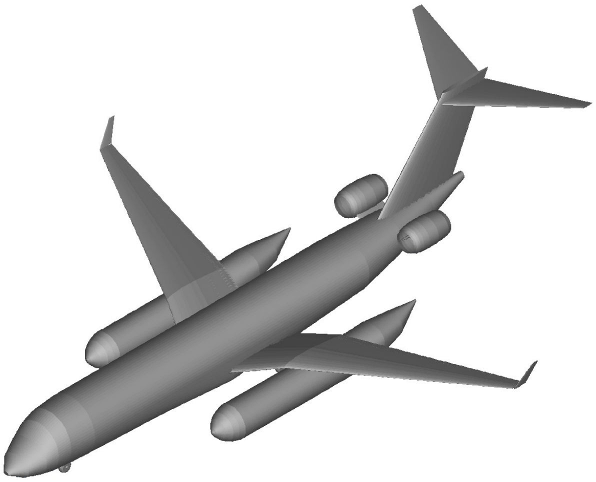

Figure 3.2 Schematic of B737-800 based hydrogen combustion aircraft configuration with externally mounted fuel tanks.

3.2.2 Results

The external tanks were found to add approximately10,000 lbs. of structural weight; however, the 1/3 fuel reduction based on comparative energy densities led to a gross takeoff weight of 154,000 lbs., significantly lower than the B737-800 with Jet fuel. The addition of parasite drag from the external tanks was estimated using the same skin friction estimation techniques based on the slender bodies for the aircraft fuselage. The tanks were estimated to generate about 50% of the parasite drag generated by the fuselage along with an interference factor of 1.5 to account for the mounting on the wing. The estimate of the parasite drag of the external tanks amounted to 0.0056, a significant increase. Initial estimates from WUADS calculated a maximum range of 2938 nautical miles, roughly the same as that of B737-800.

Ultimately the external tank configuration was determined to be infeasible for a number of reasons. Although the overall efficiency of this configuration was seen to be roughly equivalent to that of B737-800, it was still seen to be inefficient compared to the internal tank configuration.

The drag penalty caused by the wing mounted fuel tanks was simply too large to be acceptable. In addition, safety concerns also arise with this configuration, such as the lack of wing clearance on takeoff and the inability to perform the wheels up landing. Furthermore, given the aft engine placement, hydrogen fuel lines would likely require to be placed near the passenger compartment, leading to poor insulation conditions for the cryogenic fuel and the concern of asphyxiation in the event of a busted fuel line. From this study, it was determined that an internal LH2 fuel tank configuration would likely be needed for the design of any hydrogen powered aircraft.

3.3 Internal Fuel Tank Configuration

3.3.1 Design

A separate configuration was examined to analyze the benefit of internal pressurized cryogenic hydrogen fuel tanks in the fuselage. To accommodate the added required volume of the tanks, the fuselage geometry was based on that of the Boeing 767. The added volume of the fuselage allowed for the space for the fuel tanks to be placed both above and behind the passenger compartment to accommodate an adequate amount of hydrogen fuel. A high wing configuration was used to accommodate the previously established safety concerns with pumping hydrogen fuel near the passenger compartment as mentioned in the last section. Figure 3.3 shows the hydrogen combustion powered aircraft based on the fuselage of the B767 with internal LH2 fuel tanks.

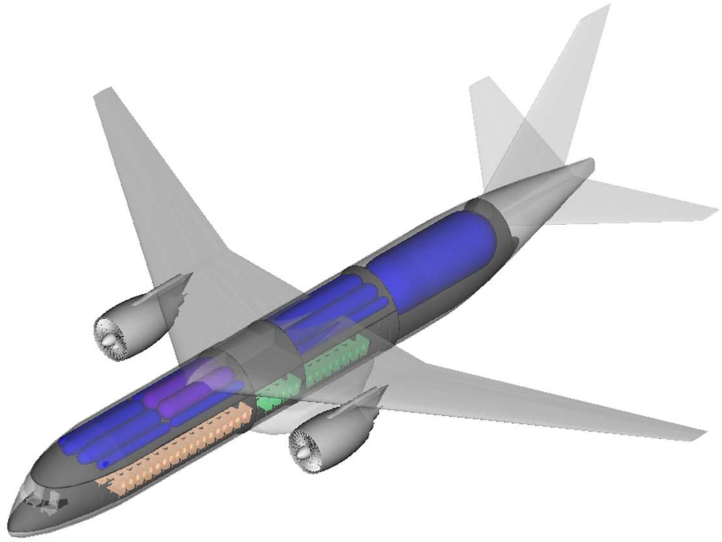

Figure 3.3 Hydrogen combustion powered aircraft based on the fuselage of the B767 with internal LH2 fuel tanks.

An optimization case was run on the wing geometry of the modified B767 configuration with internal fuel tanks to further increase the efficiency. The design variables in this case were set as the taper ratio, quarter chord sweep angle, and the wing area. A constant aspect ratio of 13.56 was used based on an estimate of the current maximum obtainable aspect ratio without experiencing the negative aeroelastic effects [46]. To follow the same ICAO reference code as for the B737-800, wingspans over 113 ft were assumed to have a wing folding mechanism like that of the B777 [42]. The results of this optimization problem in comparison to the B737-800 are given in Table 3.1.

Table 3.1 Wing optimization results for hydrogen combustion powered aircraft with 767 Body

	Taper Ratio	c/4 Sweep Angle (deg)	Area (ft^2)	Maximum Range (nmi)
Boeing 737-800	0.159	25.02	1340	2935
767 Body LH2 Aircraft	0.143	28.3	1527	3341

3.3.2 Results

As can be noted from Table 3.1, the aircraft configuration with B767 fuselage and internal fuel tanks has greatly improved efficiency compared to B737-800. With an equivalent fuel weight in terms of total energy, the hydrogen combustion powered aircraft configuration has over 400 extra nautical miles of extra range compared to B737-800. With the extended fuselage of B767, the weight was calculated as 173,983 lbs., which is very close to that of the B737. The large fuselage added about 25 extra drag counts of parasite drag; however the extended B767 with internal fuel tanks is still far more efficient than B767 with external tanks.

Another important metric to look at in the design of hydrogen powered aircraft is its economic viability. The production of the large scale green hydrogen is currently a well-funded area of research due to growing demands for alternative energy sources. However, there is disagreement on projections for the price of hydrogen fuel by the year 2050, but a reasonable estimate seems to be around $2.00 per kg [47, 48]. As shown in Table 3.2, at this price of green hydrogen, the modified B767 hydrogen combustion configuration could be significantly more economical to operate than the standard B767, especially in long flights. This is an important result since it shows that a hydrogen combustion powered aircraft configuration can be more energy efficient and economical even with the drawback of requiring large, pressurized fuel tanks.

Table 3.2 Fuel costs for B737-800 and modified B767 hydrogen combustion powered aircraft configurations at mission ranges of 1500 and 2500 nmi

	1500 nmi		2500 nmi	
	737-800	767 Body HC	737-800	767 Body HC
Fuel Required (lbs.)	26,414	9,697	40,776	13,555
Fuel Cost ($)	9,841.275	8,796.982642	15,192.24	12,296.91
Percent Difference		-10.61%		-23.55%

Chapter 4: Modeling of Powertrain for Hydrogen Fuel Cell Powered Aircraft

4.1 Introduction

A hydrogen fuel cell powered aircraft is a highly advantageous concept for decarbonization since it would be entirely free of all emissions (it produces only water) as opposed to a hydrogen combustion powered aircraft which would be carbon free but emit Nitrogen Oxides (NOx) and water vapor. However, a hydrogen fuel cell powered aircraft requires the use of a fully electrified drivetrain, which is a complex and big design challenge. While excelling in the lightweight and short range flight, the limitations in designing a fully electrified drivetrain potentially reduce the prospects of a hydrogen fuel cell powered commercial aircraft to smaller passenger count and short-range flights. Alternative to the hydrogen combustion powered configuration presented in Chapter 3, special attention must be given to the design of the electrified powertrain to analyze the propulsive performance of the aircraft. This chapter provides the details of the system architecture of the powertrain of a hydrogen fuel cell powered aircraft. Additionally, the models for system performance are derived for use in the full aircraft analysis.

4.2 Powertrain Components

A thorough understanding of the design of the hydrogen fuel cell (HFC) powertrain is critical in the conceptual design and analysis of a hydrogen fuel cell powered aircraft. A simplified model of the HFC powertrain with all the required components is shown in Fig. 4.1.

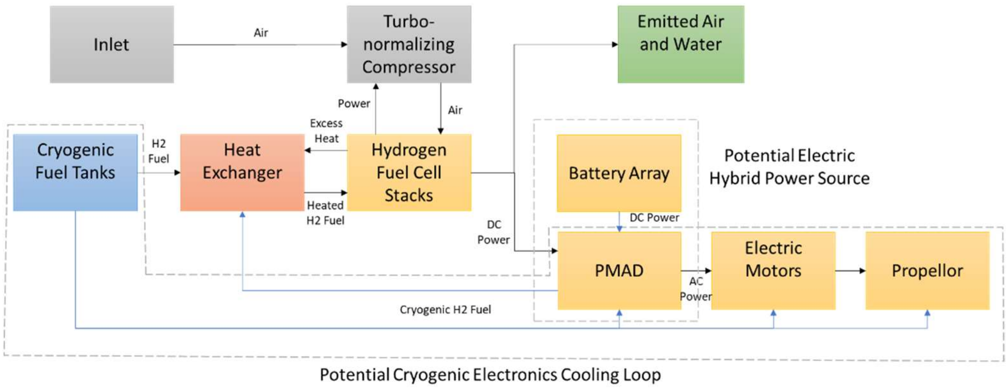

Figure 4.1 Model of the powertrain of a hydrogen fuel cell powered aircraft.

Several crucial processes must occur to power the hydrogen fuel cell stacks. First, air must be captured from the atmosphere, cooled, and pressurized to within the operating temperature and pressure of the hydrogen fuel cell. Similarly, the cryogenic fuel flow from LH2 tank must be heated to within the operating conditions and the excess heat generated by the fuel cell stacks and electronics must be cooled and vented into the atmosphere. The power generated from the hydrogen fuel cell stacks must be filtered through a power management and delivery system which is capable of combining the power output from the fuel cells and the battery array, converting the DC power output to an AC current, and dividing the total power among all the necessary components. The following section covers the specific design parameters of the various components needed in an HFC powertrain as well as the automated design process used to carry out this analysis. As an important note, fuel cell technology and its application in aviation is still an ongoing research field with several emerging technologies; however, with a focus on this project, only the most well researched technologies are considered.

4.2.1 Fuel Cell Stacks

Several potential designs of fuel cells exist, each with their own potential benefits and drawbacks for use in aviation. Two of the most well researched fuel cell designs are the Proton-

Exchange Membrane Fuel Cells (PEMFCs) and the Solid Oxide Fuel Cells (SOFCs) which have been commonly considered for these purposes; however, due to SOFC's emission of NOx gas, this fuel cell design is not considered in this project [49, 50, 51]. PEMFCs are naturally suited for use in aviation for a variety of reasons, the most important being that it is entirely emission free. Other benefits are their low weight, high efficiency, and resistance to degradation. Two designs of PEMFC exist for consideration – the low temperature and the high temperature PEMFC (LT-PEMFC and HT-PEMFC). Perhaps the most studied and prevalent design of hydrogen fuel cell, LT-PEMFC operates using the membrane saturated in the liquid water to act as the electrolyte between the hydrogen fuel and the air. The liquid water contained in the membrane implies that the LT-PEMFC is well moisturized and has an operating temperature between 60-100°C, a relatively low operating temperature in comparison to other designs [50]. HT-PEMFC in contrast works using a membrane containing a form of acid increasing the operating temperature and thus the efficiency of the entire system. The high temperature requirement in HT-PEMFC's leads to a long start up time and quicker degradation, thus leading to the LT-PEMFC design being selected as the optimum fuel cell type for this project.

4.2.2 Turbo-Normalizing Compressor

Research on operation of PEMFC at high altitudes shows a steep drop in fuel cell efficiency with decreasing ambient air pressure and density with altitude [52, 53, 54]. For this reason, a prospective hydrogen fuel cell powered aircraft would require the use of an air supply system in which the air is captured from the atmosphere, compressed to ensure constant airflow through the fuel cell stacks, and heated to within the operating temperatures. A diagram of this process is shown in in Fig. 4.2.

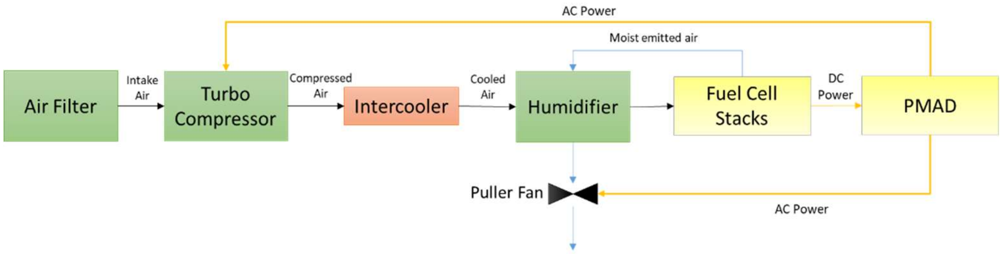

Figure 4.2 Turbo normalizing compressor system

Design and optimization of a compressor for use in a hydrogen fuel cell powered aircraft requires an analysis of differing efficiencies since higher operating pressure typically results in higher fuel cell efficiency; however, it requires a larger portion of the generated power also [50, 53]. Several system architectures have been proposed to achieve this high-altitude compression such as a dual diaphragm compressor or a multistage turbo compressor [55, 56].

4.2.3 Thermal Management System

Perhaps the most crucial and complex step in the design of a fully electrified hydrogen fuel cell powertrain is the design of a thermal management system. There are several areas which require heating and cooling and a few solutions have been proposed to manage this system. The main areas which require thermal management are as follows: heating of the cryogenic fuel to within operating temperature for the fuel cells, cooling of the excess heat generated by the fuel cell stacks, cooling of the various subsystems involved in the powertrain, and heating of the captured air to within the operating temperature. A schematic of this system is shown in Fig. 4.3.

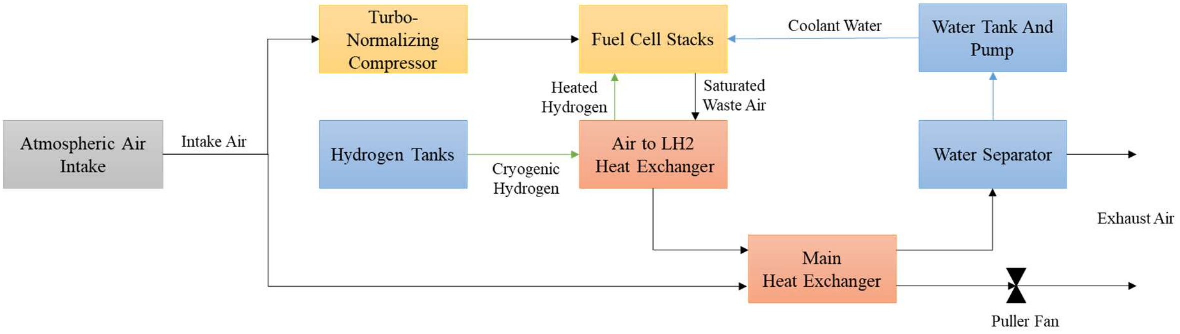

Figure 4.3 Powertrain thermal management system

Even running at absolute optimum conditions, modern PEMFC's have a maximum thermal efficiency of around 50-55%, meaning that the waste heat is generated at a rate equal to that of the shaft power required to propel the aircraft. This is a massive amount of heat generated which if inadequately cooled could cause rapid overheating and degradation of the fuel cells. The most efficient way currently possible to remove this heat makes use of a phase change cooling cycle known as the evaporative cooling. In this process, water is captured from the exhaust stream and is injected back into the fuel cell. This water acts as a coolant, since the entire excess heat generated by the fuel cells can be captured by the phase transition as the water in the membrane evaporates. This in turn greatly reduces the required radiator size and could potentially nullify the need for a humidifier in the turbo-normalizing compressor altogether [57, 58]. An example of a phase change cooling loop specifically designed for Megawatt-scale aircraft engines was demonstrated by Kösters et al. in application to a 9 MW engine where it was shown to reduce the total engine drag loss by 23% compared to the traditional cooling methods [59].

Given the existence of liquid hydrogen (LH2) fuel on board, the use of cryogenic superconducting electric components becomes both achievable and highly beneficial. Two novel architectures have been proposed for this concept. In the University of Illinois' Center for High-

Efficiency Electrical Technologies for Aircraft (CHEETA) project, the cryogenic LH2 fuel on board is used directly as a coolant for superconducting electrical systems to greatly increase the efficiency, namely in the electric motors powering the propellors [60]. A similar system which uses the cryogenic hydrogen fuel as a coolant for highly efficient electronic subsystems has been presented by Hartmann et. al in Ref. [61] in which it was shown that the systems such as the gearbox, electric motors, power converters, etc. could demonstrate efficiencies of over 99%. Conversely in GKN Aerospace's H2GEAR project, the cryogenic environment in which the LH2 fuel is stored is also used to house the cryogenic helium to be used as a coolant for superconducting electrical components [62].

Finally, the cryogenic hydrogen fuel must be heated to within operating temperatures of the fuel cell. This process can be accomplished using a simple heat exchanger from the hot, saturated air exiting the fuel cell stacks, both heating the cryogenic fuel and cooling the exhaust gas from the fuel cell stacks. In fact, Lenger et. al described a system they refer to as a reversible cryogenic exergy utilization system (rCEUS) [63]. In the rCEUS, a thermodynamically ideal heat engine process is employed using the coolant stream from the fuel cells as a heat source and the cryogenic hydrogen fuel as a heat sink to utilize the entirety of the cryogenic hydrogen's exergy. This effectively serves three purposes: heating the hydrogen to within operating conditions, cooling the exhaust gas, and generating a supplemental source of power. It was found that this system effectively reduced the overall fuel cell stack power demand by a value of 14-31%. Note that while the heat transfer effects of this system are modeled in this dissertation, the supplemental power generation is not.

4.2.4 Hybrid Battery-Fuel Cell Power

Running hydrogen fuel cells at off-design power outputs tends to result in both the sub optimal efficiency and increased degradation rates. The available power from the fuel cells is relatively independent of the altitude, solely limited by the compressor efficiency. This leads to a unique design challenge in sizing the power supply with no auxiliary power sources. Sizing the HFC stacks to maximize efficiency and minimize fuel cell degradation at cruise conditions means no excess of power would be available for the takeoff and climb portions of the flight leading to unfavorable takeoff characteristics and a very long and expensive climb. Sizing the HFC stacks to provide an excess power for the takeoff and climb however would inevitably lead to the decreased efficiency and increased degradation at cruise. Perhaps a better solution is the use of stored batteries to supplement power requirements in takeoff and climb while using only the fuel cells during cruise. A graphical description of this method is shown in Figure 4.4.

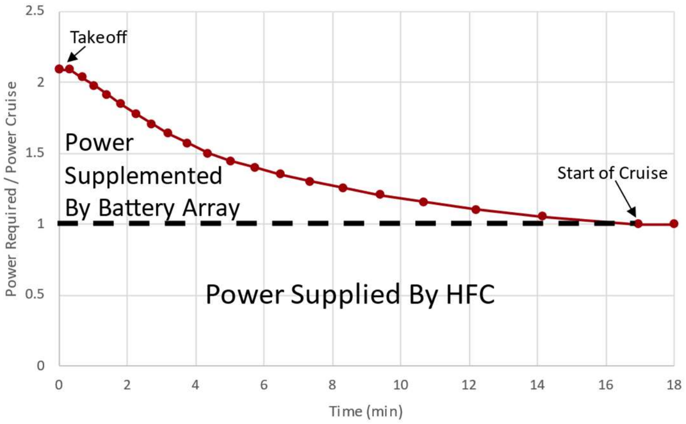

Figure 4.4 Power required during the takeoff and climb sections normalized by the power required at cruise

This system architecture has been well studied for its use in aerospace applications. In fact, in addition to supplementing the power requirements, the use of hybrid fuel cell battery power for propulsion offers useful redundancy for power sources [64, 65]. Extra power generated by the fuel cells in the low power requirement portion of the cruise flight can be used to passively recharge the battery array in the flight, nullifying portions of the required reserve fuel. This concept was demonstrated with great success in a two-seat aircraft as a part of the ENFICA-FC project in 2012 where it was found to be a feasible propulsion source for future aircraft [65].

4.2.5 Hybrid Turbogenerator-Fuel Cell Power

As an alternative to the use of lithium-ion batteries for supplemental power augmentation, a hydrogen combustion system can be used. Multiple system architectures have been proposed for this purpose. Kösters et. al proposed a system which uses a hydrogen combustion jet engine to alleviate the exhaust drag created by expelling the excess heat from the fuel cell, a system which was seen to be highly efficient [59]. Through initial studies however, it appears that the addition of extra engines and nacelles add a greater drag and weight penalty than the power savings can account for. Alternatively, a simple hydrogen power turbogenerator can be used. Systems which utilize a hybrid gas turbine – fuel cell power source have been well studied and found to be highly advantageous [17, 66]. There are a few drawbacks to such a system, however. The heat produced by a hydrogen powered gas generator would greatly increase the required sizing of the thermal management system. Additionally, such a system would not be inherently emission free. For these reasons, a hybrid turbogenerator-fuel cell power system was not considered for further analysis in this project.

4.3 Powertrain Modeling

The full fuel cell stack power required, P_{fc}, can be expressed as follows.

$$P_{stack} = P_{shaft} + P_{comp} + P_{cool} + P_{misc} \tag{4.1}$$

where P_{shaft} represents the power requirement from the propellors calculated by WUADS, P_{comp} is the power requirement of the compressor, P_{cool} is the power required from the cooling system, and P_{misc} represents all other power requirements. The compressor and cooling system power however are largely dependent on the performance of the fuel cells however, meaning an iterative loop is required to balance all these power requirements. The following section provides details of all the models used in this calculation. Note that all the equations are in SI units.

4.3.1 Fuel Cell Model

A semi empirical method was used to model fuel cell performance, largely based on the methods described by Spiegel in Ref. [67]. This model finds the fuel cell stack's power output, heat generation, and mass flow rates based on a few inputs: the current density $i\ (A/cm\hat{}2)$, the operating pressure $P_{op}(atm)$, the operating temperature $T_{op}(k)$, active area $a_{cell}(cm^2)$, and the number of fuel cells. The cell voltage of the fuel cell is calculated using the following equation.

$$V_{cell} = E_N - V_{ohm} \quad - V_{act} - V_{conc} \tag{4.2}$$

In Eq. (4.2), E_N represents the thermodynamic potential of the cell and can be modelled using the Nernst equation shown below [68].

$$E_N = 1.229 - 0.85 * 10^{-3}\left(T_{op} - 298.15\right) + 4.3085 * 10^{-5} T_{op}\left(\ln p_{H_2} + .5 \ln p_{O_2}\right) \tag{4.3}$$

where p_{H_2} and p_{O_2} represent the partial pressures at the fuel cell interface of hydrogen and oxygen. These values can be modeled using the following relations [69].

$$p_{H_2} = 0.5 p_{H_2O}^{sat} \left[\exp\left(-\frac{1.635i}{T_{op}^{1.334}}\right)\frac{p_a}{p_{h_2O}^{sat}} - 1\right] \tag{4.4}$$

$$p_{O_2} = p_{H_2O}^{sat} \left[\exp\left(-\frac{4.192i}{T_{op}^{1.334}}\right)\frac{p_c}{p_{h_2O}^{sat}} - 1\right] \tag{4.5}$$

where p_a and p_c are the anode and cathode pressures which for simplicity are both set equal to the fuel cell operating pressure. p_{h_2O} in the equation represents the saturation pressure of water, which can be modeled empirically as follows.

$$\log_{10} p_{H_2O} = -2.1794 + (0.02953T_{op}) - (9.1837 * 10^{-5}T_{op}^2) + (1.4454 * 10^{-7}T_{op}^3) \quad (4.6)$$

Note that the temperature used in Eq. (4.5) must be input in degrees Celsius. The total voltage output of the cell from Eq. (4.2) is the difference between the thermodynamic potential and the ohmic overpotential V_{ohmic}, the activation potential loss V_{act}, and the concentration potential loss V_{conc}. These terms can be modelled simply as follows [67].

$$V_{ohmic} = i * Z_{ohmic} \quad (4.7)$$

$$V_{act} = -\frac{RT}{2\alpha F}\ln\left(\frac{i}{i_0}\right) \quad (4.8)$$

$$V_{conc} = \alpha_1 * i^k \ln\left(\frac{i}{i_{limit}}\right) \quad (4.9)$$

The parameters found in these models and their respective values are given in Table 4.1. For a more thorough explanation of these parameters, see Refs. [67, 55].

Table 4.1 Fuel cell model parameters

Variable	Symbol	Value	Unit
Universal gas constant	R	8.314	$J/(K * mol)$
Faraday constant	F	96487	Coulombs
Internal cell resistance	Z_{ohmic}	0.19	$Ohm * cm^2$
Transfer coefficient	α	0.5	
Amplification constant	α_1	0.085	
Exchange current density	i_0	$10^{-6.912}$	A/cm^2
Limiting current density	i_{limit}	1.5	A/cm^2
Mass transport constant	k	1.1	

Using the parameters calculated in Eqs. (4.7-4.89), the total cell voltage can be found using Eq. (4.2). The power generated by a fuel stack containing a total number of cells N_{cells} can then be found using the following equation.

$$P_{stack} = V_{cell} * N_{cells} * i * A_{cell} \tag{4.10}$$

The mass flow required for hydrogen and oxygen in the fuel cell operation can be expressed as follows [70].

$$\dot{m}_{H_2} = \left(1.05 * 10^{-8} \frac{P_{stack}}{V_{cell}}\right) kgs^{-1} \tag{4.11}$$

$$\dot{m}_{air} = \left(3.57 * 10^{-7} \frac{P_{stack}}{V_{cell}}\right) kgs^{-1} \tag{4.12}$$

4.3.2 Compressor

The power required by the compressor system can be modeled assuming isentropic compression as follows [50].

$$P_{comp} = \dot{m}_{air} C_{p,air} (T_{t_2} - T_{t_1}) / \eta_{em} \tag{4.13}$$

where $C_{p,air}$ is the heat capacity of the air and η_{em} is the electric motor efficiency ratio, assumed to be constant for all components which use electric motors. T_{t_1} and T_{t_2} represent the total temperatures before and after the compressor and can be calculated as follows. Note the subscript atm denotes atmospheric conditions.

$$\frac{T_{t_1}}{T_{atm}} = 1 + \frac{(\gamma - 1)}{2} M_\infty^2 \tag{4.14}$$

$$T_{t_2} = T_{t_1} \left(1 + \left(\frac{1}{\eta_{comp}}\right) \left(\frac{P_{op}}{P_{atm}}\right)^{\left(\frac{\gamma-1}{\gamma} - 1\right)}\right) \tag{4.15}$$

where η_{comp} is the compressor efficiency, P_{op}/P_{atm} is the ratio of the fuel cell operating pressure to the atmospheric pressure, and γ is the specific heat ratio of air, 1.4.

4.3.3 Cooling System

For simplicity and general applicability across a wide range of full aircraft configurations operating at different atmospheric conditions, this work did not employ a full thermodynamic model of the fuel cell system. Instead, a generalized empirical model developed by NASA for use on electrified aircraft thermal management systems was employed [71]. In this model, the parasitic power requirement from the pumps powering the cooling system is modeled as follows.

$$P_{cool} = \left(0.371P_{rejected} + 1.33\right)f(dT) \tag{4.16}$$

where $P_{rejected}$ is the power generated by the fuel cell stack, which is rejected, and it can be estimated based on the fuel cell efficiency η_{fc}.

$$P_{rejected} = \left(\frac{1}{\eta_{fc}} - 1\right)P_{stack} \tag{4.17}$$

The fuel cell efficiency in Eq. (4.17) is estimated as the ratio of the cell's thermodynamic potential to the actual cell output from Eq. (4.2) and Eq. (4.3). $f(dT)$ in Eq. (4.16) is a correction factor calculated as follows.

$$f(dT) = 0.0038\left(\frac{T_{atm}}{dT}\right)^2 + 0.0352\frac{T_{atm}}{dT^2} + 0.1817 \tag{4.18}$$

where dT represents the difference in temperature between the hot coolant and the atmospheric air. This is a very generalized model; however, it has been seen to produce reasonable results for the cooling system power requirements in similar applications [50, 71].

4.3.4 Subsystems

All other subsystems with power requirements to be met by the fuel cell stack are simply modeled using electrical efficiency values. For example, the power loss in the power management and delivery system (PMAD) is modeled as follows.

$$P_{pmad} = P_{stack}(1 - \eta_{pmad}) \tag{4.19}$$

The power lost in the electric motors powering the propellor only depends on the shaft power required and can be modelled similarly as follows.

$$P_{em} = P_{shaft}(1 - \eta_{em}) \tag{4.20}$$

4.4 System Performance and Optimization

The overall power required by the fuel cell stacks then depends on the sum of all the components described previously. An iterative loop must be performed in which a total power output is guessed and the fuel cell stack sizing is calculated using Eq. (4.10), then all the subsystems are sized accordingly. The total power requirement is then calculated using Eq. (4.1) and the guessed power requirement is updated. The weight of the whole powertrain is estimated simply using the component energy density estimates, which are examined in chapter 5.

Using these models, the overall fuel cell stack performance can be calculated using 4 user defined inputs: the current density, the operating pressure, the operating temperature, and the shaft power required at cruise. The operating conditions in this work are held to 80°C and 1.1 atm in accordance with the normal values of LT-PEM fuel cells. Additionally, the shaft power required at cruise is calculated by WUADS for each individual case based on the aircraft's aerodynamic performance. This leaves only the current density of the fuel cells which need to be optimized for each case. This is not a simple optimization problem, however. Optimizing with the objective to minimize overall power loss from subcomponents or to minimize the overall hydrogen fuel flow would lead to smaller current densities. Smaller current densities however lead to a larger required number of cells and a larger system weight. This effect can be seen in Fig. 4.5 in which both the powertrain weight and specific fuel consumption are modeled. To balance this tradeoff of fuel efficiency to weight, the overall range of several full aircraft configurations was tested where it was determined the optimum current density was around 0.7 a/cm^2. Note that this value was relatively constant across all tested configurations and was held as a constant for all tested configurations.

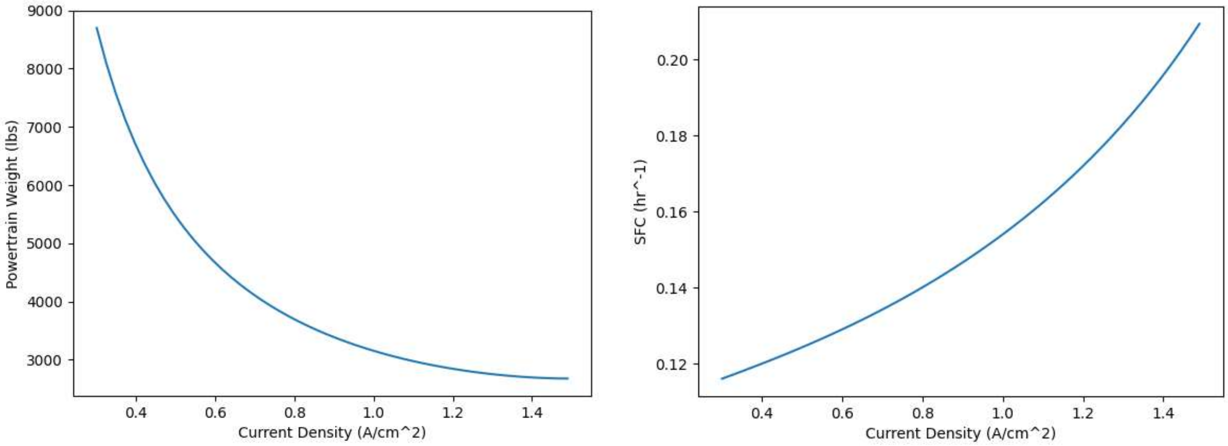

Figure 4.5 Powertrain weight (left) and SFC (right) for a 1MW hydrogen fuel cell powertrain

Chapter 5: Hydrogen Fuel Cell Powered Aircraft Configurations

5.1 Proposed Configurations

Three configurations of hydrogen fuel cell powered aircraft were tested. The first configuration tested was a retrofitted Cessna 208. This configuration was mainly tested as a validation case to compare to similar studies which have been conducted. The second configuration tested was a short ranged, regional sized airliner with a range of 1305 nmi with a maximum of 50 passengers. This configuration is based on the geometry of the Bombardier CRJ-200. This aircraft was analyzed at several different component efficiency levels to model the impact of technological innovation in hydrogen fuel cell powered aviation. The last aircraft tested was a short to medium range airliner with a maximum of 100 passengers based on the Boeing 737-200. This configuration was tested at several different design ranges between 1000 and 2300 nmi and compared to a similarly designed hydrogen combustion powered aircraft configuration.

Similar constraints are proposed for each hydrogen fuel cell aircraft configuration as were put on the hydrogen combustion aircraft configurations in chapter 2. These configurations must have similar takeoff and landing characteristics as the aircraft they are based on, meaning that the wing area must be at minimum the same and there must be an excess of power or high lift devices present. To meet the ICAO reference code requirements, the latter two proposed configurations must have wingspans below 113 ft, meaning that the wider wingspans should make use of a wing folding mechanism like that of the Boeing 777 max. Considerable emphasis must also be placed in ensuring the logical safety standards with the use of cryogenic hydrogen fuel. For example, cryogenic fuel tanks must be stored in an unpressurized environment separated from the passenger compartment by use of a solid bulkhead to reduce the impact of potential risks posed by the hydrogen gas leaks. Likewise, hydrogen fuel should not be transported through lines which pass through the passenger compartment.

In both the CRJ-200 and the 717-200 configuration, the fuel tanks are held inside the aircraft's fuselage. In the baseline configuration, a single large cylindrical tank with spherical caps contains the entire fuel in the fuselage aft of the passenger compartment with the hydrogen fuel cell stacks and related powertrain components located aft of the tank. The battery array which helps with excess power requirements during takeoff and climb part of the mission profile is contained within the wings. The design of this hybrid battery-fuel cell power system was discussed in Chapter 4.2.4. A schematic of this configuration is shown in Fig. 5.1.

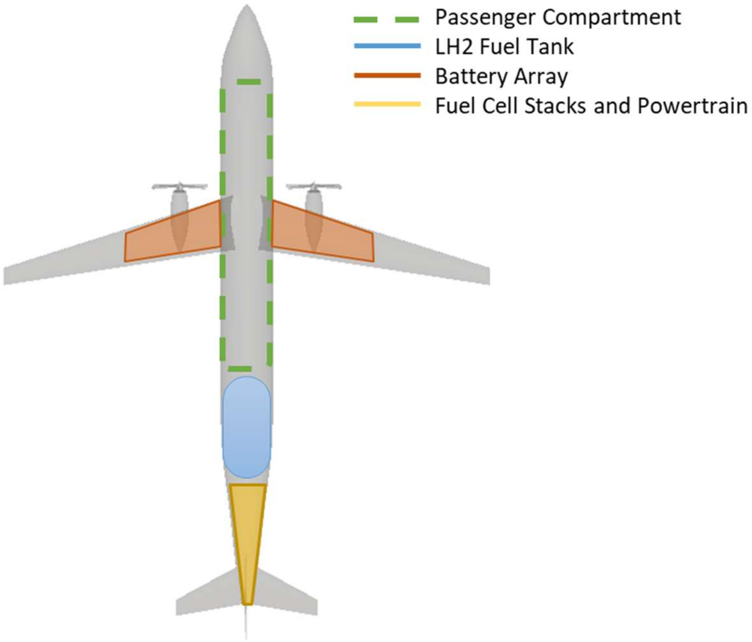

Figure 5.1 Proposed hydrogen fuel cell powered aircraft configuration with aft fuel tanks

The main advantage to the proposed design is the simplicity offered in the storage of all fuel near the fuel cell power train. By having one section aft of the passenger compartment that contains both the cryogenic fuel and the powertrain, complex designs such as cryogenic cooling loops and heat exchangers are greatly simplified. This design also provides the simplest and greatest safety measures in reducing the risk of hydrogen fuel leaks. There are however several downsides to this design. With all the hydrogen fuel concentrated in the aft of the fuselage, there are significant stability and control concerns with shifting of the center of gravity. Likewise, the placement of both the powertrain and fuel tanks in the aft section increases the distance at which power must be transmitted to the engines. The electric motors powering the engines would not be able to be cryogenically cooled as well due to the restriction of not passing the LH2 fuel lines through the passenger compartment. Additionally, extending the fuselage a significant amount lengthwise introduces issues with the structural integrity of a high fineness ratio fuselage. Some of these concerns can be addressed by increasing the diameter of the fuselage and by employing the overhead fuel tanks in conjunction with this configuration as shown in Fig. 5.2.

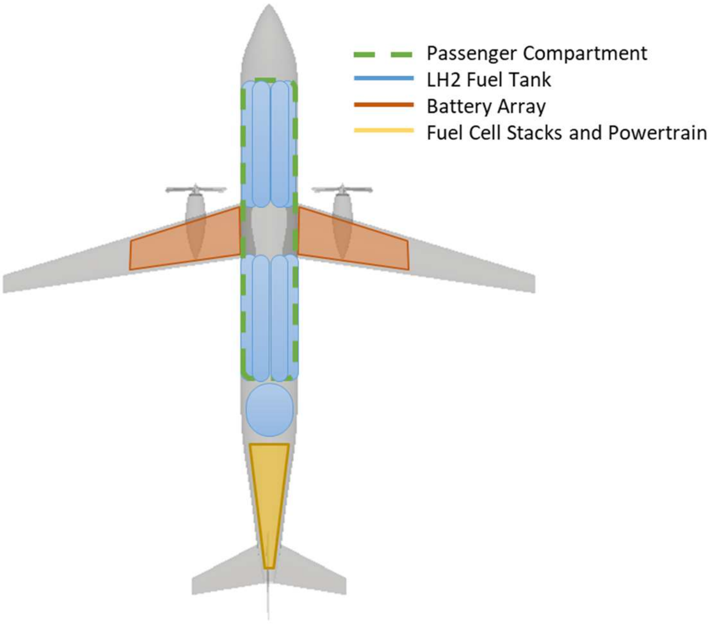

Figure 5.2 Proposed hydrogen fuel cell powered aircraft configuration with aft and overhead fuel tanks

In the proposed design in Fig. 5.2, the diameter of the fuselage is extended to include the overhead fuel tanks. The unpressurized environment aft of the passenger compartment must be extended to overhead portion of the fuselage using another solid bulkhead. As a requirement, the fuselage must maintain adequate space for cargo storage which can be accomplished by extending the diameter below the passenger compartment. A 2D cross section of the placement of these overhead fuel tanks is shown in Figure 5.3.

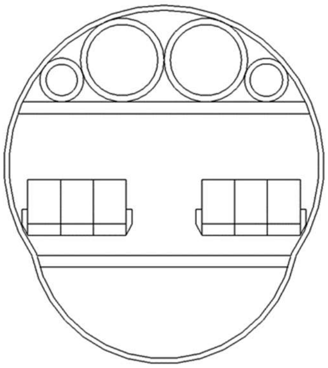

Figure 5.3 Cross sectional view of the overhead fuel tank configuration

This design has several benefits compared to the baseline design with aft fuel tanks configuration. First, by controlling the fuel flow from each tank the issue of the shifting center of gravity throughout the mission profile can be essentially nullified. Additionally, cryogenic fuel from the overhead tanks can be used as a coolant for the electric motors powering the propellors increasing their thermodynamic efficiency. This design does however introduce added structural weight from the addition of the fuel tanks and added overhead bulkhead as well as added drag from the extended fuselage.

Both configurations presented here have several degrees of freedom in the optimization. The fuselage can be extended either lengthwise or by their diameter. The engines could be placed on the aft section of the fuselage to simplify the power delivery system from the fuel cell powertrain; however, this could potentially present challenges in balancing the center of gravity. The overhead fuel tank configuration has flexibility in the number of fuel tanks used in the overhead compartment. Extending the fuselage by an adequate amount in diameter can also nullify the need for aft fuel tanks altogether in this configuration.

An additional aspect is considered in this design process: the use of a Truss braced wing. As mentioned in section 1.4.3, a truss braced wing configuration could greatly benefit the efficiency of an aircraft by extending the maximum possible aspect ratio. This could greatly extend the range of such an aircraft. A schematic of a generalized truss braced wing configuration based on the Boeing Sugar High configuration is shown in Fig. 5.4 [7].

Figure 5.4 Aircraft configuration with a truss braced wing

5.2 Design Process

With the full Hydrogen Fuel Cell (HFC) powertrain modeled, WUADS can now be used to analyze the full aircraft configurations to predict the overall performance and efficiencies. The full process of generating an aircraft geometry, sizing the fuselage to fit the fuel tanks, sizing the HFC powertrain, and running a full range analysis was automated and is shown in Fig. 5.5.

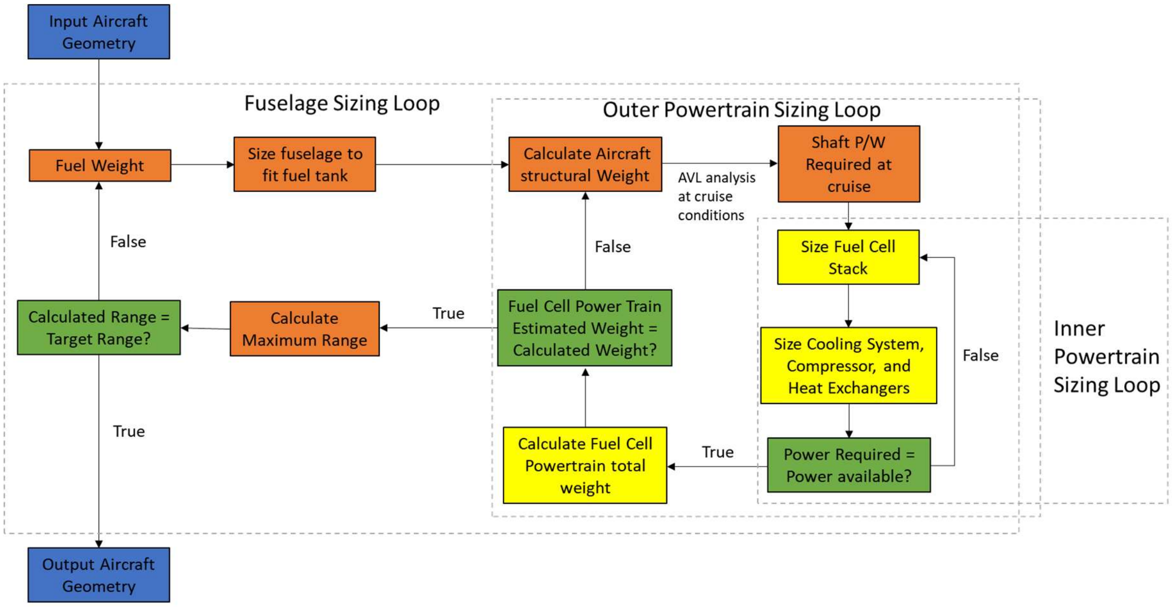

Figure 5.5 Hydrogen fuel cell powered aircraft design process

The process shown in Fig. 5.5 uses a series of three iterative loops to fully size a hydrogen fuel cell powered aircraft. First an aircraft configuration is input with a specified maximum range. An estimate of necessary fuel weight is generated, and the fuselage is sized around this amount of fuel, extending and expanding the fuselage as needed to accommodate the amount of fuel. The aircraft structural weight and drag are calculated using an estimated powertrain size and a full analysis is performed at cruise conditions using the previously discussed analysis code. From this mission analysis, the required shaft power at cruise is calculated. This allows for an estimate of the required size of the fuel cell stack, which in turn allows for the required cooling system, compressor, and heat exchanger to be sized using the models described in Chapter 4. The total power consumed by these subsystems along with the main engine is calculated and the fuel cell size is adjusted appropriately, making up the inner powertrain sizing loop. Once all values are converged, the total powertrain weight can be calculated. If the power train size is significantly different than estimated, the full structural weight is recalculated, and the cruise condition is once again analyzed making up the outer powertrain sizing loop. This loop rarely takes more than three iterations to converge. Using the calculated powertrain sizing and efficiency, the full mission is analyzed to determine the maximum range. If the range is significantly different from the target range, the amount of fuel required is altered appropriately and the full process is run again, making up the fuselage sizing loop. This whole process allows for the correct powertrain and fuselage sizing for a given aircraft configuration.

5.3 Test Case – Cessna 208 Caravan

5.3.1 Problem Setup

The Cessna 208 Caravan was chosen as a validation case for the hydrogen fuel cell sizing methodology due to multiple other studies previously conducted on this plane [50, 56]. The Cessna 208 is a regional size turboprop plane with a maximum passenger count of 10 and a maximum range at full cargo weight of around 325 nmi and a maximum range of 1070 nmi. A schematic of the Cessna 208 is shown in Fig. 5.6.

Figure 5.6 Cessna 208 Caravan

An analysis of the current jet fuel powered Cessna 208 using WUADS was first conducted to verify the solution methodology. In this analysis it was found that estimates for both the weight and the parasite drag of the fuselage were underpredicted due to its irregular shape. To rectify this issue, a correction factor was applied for both of these variables to match the published values. Lacking detailed data of how the Pratt and Whitney PT6A-114A engine's efficiency varies with altitude and velocity, it is difficult to use the WUADS code to precisely predict the range of the aircraft; however, simulations were run using rough estimates of the specific fuel consumption seem to imply that the range predictions are accurate. All data reported on the baseline Cessna 208 are from the published data, and not the calculations. A cruise altitude of 10,000 ft at a Mach number of 0.25 was assumed. The mission profile was simplified to include one climbing section, a cruise section, and a descent.

5.3.2 Results

Upon analysis, a total of 354 lbs. of hydrogen fuel was required to complete the mission at maximum payload. This corresponds to a spherical tank with an outer radius of 3 feet, fitting nearly perfectly within the extended fuselage of the Cessna 208. A comparison of the performance of the hydrogen fuel cell powered Cessna 208 to the baseline aircraft is shown in Table 5.1 [72].

Table 5.1 Performance of the hydrogen fuel cell (HFC) powered Cessna 208 compared to the baseline aircraft

	Cessna 208	Cessna 208 - HFC
Maximum Takeoff Gross Weight (lbs.)	8000	9350
Useful Load (lbs.)	3305	2154
Operating Empty Weight (lbs.)	4695	7196
Maximum Fuel (lbs.)	2224	354
Range at Max Payload (nmi)	325	325
Maximum Range (nmi)	1070	1319

The hydrogen fuel cell powered variation of Cessna 208 is found to cut the fuel weight significantly from the baseline variation at the cost of a higher structural weight. As expected, due to the higher fuel efficiency in a hydrogen fuel cell powered aircraft, the maximum range at zero payload is significantly increased when sized to match the mission range at maximum payload.

The hydrogen fuel cell power train had weight around 1653 lbs. and required a total power production of 1775 kW. A full breakdown of the powertrain components' weight and power requirements is given in Table 5.2.

Table 5.2 Hydrogen fuel cell powertrain's component weight and power requirements for Cessna 208

	Weight (lbs)	Power Required (kW)
Fuel Cell Stack	1113	1775
Compressor	193	385
Cooling System	146	651
Electric Motor	144	720
Heat Exchanger	57	
Fuel Tank	121	

The values obtained for the component weight and power requirements as well as the maximum range are found to accurately match those obtained in a similar case in Refs. [50, 56], verifying the implementation of the methodology. Unfortunately, these results are still subject to a great deal of uncertainty as the specifics of the engine and the fuel cell performance are largely unknown. Maximum range can be greatly extended by oversizing the fuel tank; however this is determined mainly by the customer requirements.

5.4 Technology Readiness Evaluation – CRJ200

5.4.1 Problem Definition

Closely based on the Bombardier CRJ200 aircraft, the first configuration tested is a 50-passenger regional size commercial aircraft with a target maximum range of 1300 nmi. The purpose of this case is twofold. First, the powertrain sizing methodology is validated against the existing similar system architectures. Secondly, the smaller configuration will allow for the evaluation of the technology readiness giving an estimate as to when hydrogen fuel cell technology will become viable to penetrate the marketplace of short-range commercial aircraft. A schematic of the CRJ200 is shown in Figure 5.7.

Figure 5.7 Baseline model of the Bombardier CRJ200

5.4.2 Problem Setup

A test case was first run on the baseline Jet A powered version of the Bombardier CRJ-200 for both validation of the underlying models and for comparison purposes. This test case used estimated engine performance of the GE CF34-3AI for propulsion characteristics. For the baseline configuration, a cruise altitude of 37,000 ft at Mach 0.74 was used. Performing the analysis using the WUADS code, a maximum takeoff gross weight of 53,540 lbs. and a range of 1330 nmi for maximum cargo weight were calculated, both were within 2% of their real-world values.

A hydrogen fuel cell variant of the CRJ-200 was then designed using the same wing and tail geometry. The fuselage was extended backwards to accommodate the necessary fuel tanks and powertrain components, shifting the wing back as needed to maintain a constant static margin. The same low wing and aft engine design was used; however, the engines were swapped for the electrified propellors. A trade study was conducted in which it was determined that the optimum cruise altitude and Mach number for the best aerodynamic performance were 30,000 ft and 0.5 respectively.

5.4.3 Component Performance Estimates

As mentioned before, multiple subsystem performance estimates were used to demonstrate the efficiency of this configuration at different tmes in the future. These estimates are given below in Table 5.3.

Table 5.3 Performance estimates for future fuel cell powertrain subsystems in the years 2025, 2030, and 2035

	Component Specific Power (kW/kg)		
Year	**2025**	**2030**	**2035**
Fuel Cell Stacks	2000	2500	3000
Compressor	2000		
Power Management and Delivery (PMAD)	10000	12500	15000
Electric Motors	5000	7500	10000

	Component Thermal Efficiency		
Year	**2025**	**2030**	**2035**
Fuel Cell Stacks	0.5	0.5	0.5
Compressor	0.7		
Power Management and Delivery (PMAD)	0.9	0.94	0.97
Electric Motors	0.9	0.95	0.99

	Component Specific Energy (Wh/kg)		
Year	**2025**	**2030**	**2035**
Battery Array	300	400	500

These performance estimates are derived from a variety of sources. For example, LT-PEMFC maximum efficiencies in the future are corroborated from reports published by both the Aerospace Technology Institute and the EU Clean Hydrogen Partnership [73, 74]. Similarly, the specific energy of the battery arrays is obtained from a variety of sources including a NASA report detailing the future timeline of advancement in battery technology for aerospace applications [8, 75, 76]. Advancements in superconducting electronics using the aircraft's cryogenic fuel were considered when analyzing the performance of electronic components such as the motors and PMAD system [61, 62]. The 2030 estimates for these subsystems are simply interpolated between the existing values and the superconducting values. Components such as the compressor and cooling system where no notable emerging technologies outside of what was discussed in section 2 exist are simply evaluated using the previously discussed methods.

5.4.4 Results

The full powertrain performance was determined at the three tested technological advancement levels. A full breakdown of the subsystem weights and power requirements is shown in Fig. 5.8.

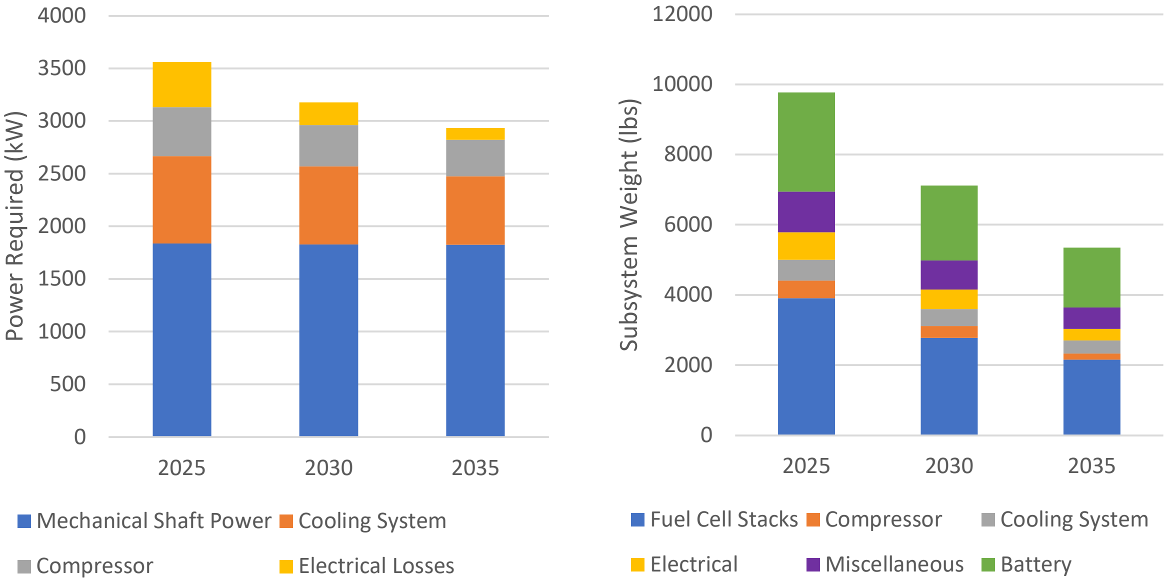

a) Component power requirements at cruise **b) Component weights**

Figure 5.8 Hydrogen fuel cell powertrain subsystem sizing at different levels of technological advancement

As expected, the weight and power requirements of the powertrain employing the projected 2025 technologies for this case are found to be prohibitively expensive. The powertrain weight accounted for approximately 30% of the overall structural weight of the aircraft using the 2025 forecast model whereas in the 2035 forecast model it accounted for only about 18%. Likewise, the waste heat and the subsystem power requirements using the 2025 forecast model accounted for over 48% of the total power production whereas the 2035 forecast model shows only 37%. These inefficiencies are reflected in the total fuel required to match the CRJ200's range of 1309 nmi at maximum loading conditions as shown in Table 5.4.

Table 5.4 Performance of hydrogen fuel cell powered CRJ200 at different technology levels

Year	2025	2030	2035
Takeoff Gross Weight (lbs.)	51367	47708	45940
Operating Empty Weight (lbs.)	34273	31030	29647
Maximum Fuel (lbs.)	4394	3979	3592

As shown in Table 5.4, the CRJ configuration based on the 2035 technology requires about 800 lbs. less fuel than that required for 2025 based technology level. This is a significant increase in efficiency and is mainly due to two effects. The first reason for the increase in efficiency is a lower specific fuel consumption in the 2035 technology-based configuration due to a significant reduction in the waste heat and subsystem power requirements. The second less obvious reason is an improvement in the climb performance. Climb is a crucial stage in determining the efficiency of a hydrogen fuel cell powered aircraft due to the increased power requirements and drastically lower powertrain weight. In fact, the 2025 technology-based configuration requires a drastic increase in the battery array sizing due to insufficient power available at the end of the climb. Finally, it is found that the hydrogen fuel cell powered aircraft of this size will be technologically feasible by the year 2030; however, it will show a large increase in the overall efficiency over the traditional propulsion methods by the year 2035 onward.

5.5 B717-200 Class Aircraft

5.5.1 Problem Definition

The main goal of this project is the design of a 100-passenger short range commercial aircraft comparable to the Boeing 717-200. To do so, a design study of a configuration close to B 717-200 aircraft is performed. In this study, both standard and truss braced wing configurations are considered, each with 0 to 4 overhead fuel tanks in the fuselage. Fuel cell powertrain components are calculated using the 2035 technology level estimates presented in the previous section. The goal of the project is to determine the most efficient design of hydrogen fuel cell powered short range commercial aircraft. The schematics of the two tested configurations are shown in Fig. 5.9. For the purpose of comparison, a variant of the standard configuration using a hydrogen combustion engine is also tested. This configuration is optimized for the same requirements using the propulsion performance estimates obtained by an NPSS simulation.

a) Boeing 717 standard hydrogen fuel cell configuration

b) Boeing 717 Truss-braced wing hydrogen fuel cell configuration

Figure 5.9 Two potential configurations of hydrogen fuel cell powered aircraft

5.5.2 Mission Profile

Selection of a mission profile, particularly the Mach number at cruise, is especially important for a hydrogen fuel cell aircraft configuration. The reason for this is that the fuel cell stacks are sized based on the power required at cruise, meaning that the fuel consumption is exponentially proportional to the cruise velocity. For example, increase in cruise Mach number for the truss braced wing configuration from Mach 0.5 to Mach 0.6 results in an increase in the required power of 38%. For this reason, an optimization is run at the cruise Mach number of each configuration. In this study, a few assumptions are made. The baseline geometry of the wing of the B717-200 and the Sugar-High are held constant for each of the configurations. Four overhead fuel tanks are included with a fuselage diameter of 15 ft, an assumption that is not far off from the optimized configuration which is presented in the next section. Propellor efficiency is assumed constant at 0.88 at cruise conditions independent of the freestream Mach number. A cruise altitude of 35,000 ft is used for all tested Mach numbers. Lastly, in order to have roughly equivalent ranges, the standard configuration is held at constant 7000 lbs. of fuel whereas the truss braced wing configuration has 6500 lbs. of fuel. The results of this study are shown in Fig. 5.10.

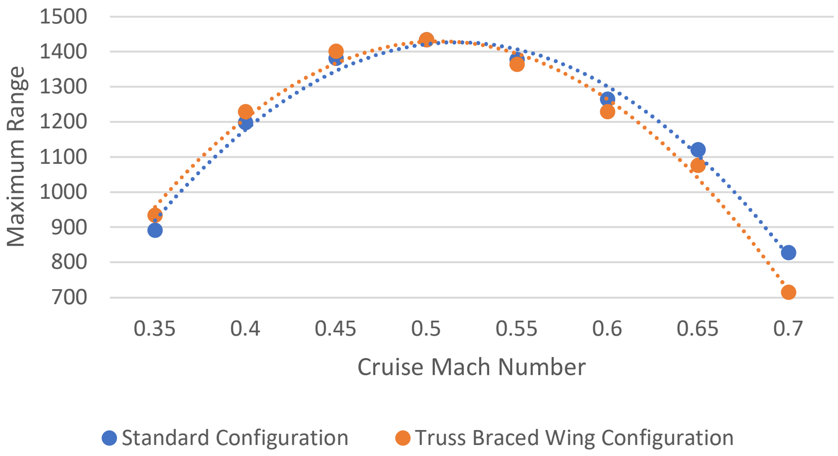

Figure 5.10 Cruise Mach number vs. maximum range for standard and truss braced wing configurations

From this study, an optimum Mach number of 0.52 for the standard configuration and 0.51 for the truss braced wing configuration were determined. Preferably the aircraft would fly at transonic speeds comparable to their jet fuel powered counterparts; however, the use of propellor engines and the cascading effect between the speed and the fuel consumption makes this potentially infeasible. With proper considerations, efficiency at a cruise Mach number around 0.6 may be achievable; however, it is unlikely that the transonic speeds will be achievable with short range hydrogen fuel cell powered aircraft.

5.5.3 Configuration Optimization

Two separate optimization cases were run to determine the optimum geometric characteristics of the wing and the fuselage. These optimization cases were run on configurations both with and without a truss. Each optimization case used the following design variables: wing area, wing quarter chord sweep, wing taper ratio, fuselage diameter, and the number of overhead fuel tanks inside the fuselage. Optimizing the number of overhead fuel tanks inside the fuselage as an integer allows the algorithm to consider each fuselage configuration presented in section 5.1. A consistent cabin and cargo sizing was assumed in sizing the fuselage and sizing the fuel tanks around them. The wing in each configuration was shifted to ensure a static margin of 0.2 to minimize the trim drag. The wing aspect ratio was held at 13.56 on the traditional configuration based on an estimate of the aeroelastic effects on the aspect ratio of the cantilever transonic wings made by Brooks et al [46]. Likewise, the aspect ratio of the truss braced wing configuration was held at a value of 23 based on the Boeing Sugar Volt configurations [7]. As previously mentioned, a large concern in the design of a configuration with all the fuel being contained in the aft section of the fuselage is the effect of a shifting center of gravity during the flight. This effect can essentially be mitigated using a configuration containing overhead fuel tanks. To model this effect, the cruise portion of the mission profile is split into 10 segments to capture the increase in the trim drag with fuel use. The optimum geometric design variables found for each configuration at a target range of 1430 nmi are shown in Table 5.5.

Table 5.5 Calculated optimum variables of standard and truss braced wing aircraft configurations

	Wing Area (ft^2)	C/4 Sweep (deg)	Taper Ratio	Fuselage Diameter (ft)	Number of Overhead Fuel Tanks
Standard Configuration	1242.6	7.29	0.27	14.74	4
Truss Braced Wing Configuration	1407.34	9.26	0.18	15.77	4

As shown in Table 5.5, both configurations experience an increase in efficiency using four overhead fuel tanks. This means that the decrease in trim drag from the mitigation of the shifting center of gravity is found to make up for the increase in the structural weight from the tanks. Likewise, both configurations seem to favor a wide fuselage with more fuel storage in the overhead tanks over a narrower configuration.

5.5.4 Analysis and Results

As expected, the truss braced wing for B717-200 based aircraft is seen to significantly increase the efficiency of the standard configuration. For a mission range of 1430 nmi, the standard configuration requires 7031 lbs. of fuel whereas the truss braced wing configuration only requires 6462 lbs. An interesting result arises however when the aircrafts are sized for different design ranges as shown in Figure 5.11. Each of these configurations was designed and optimized for their respective design ranges. This figure also shows the results for the hydrogen combustion configuration for comparison.

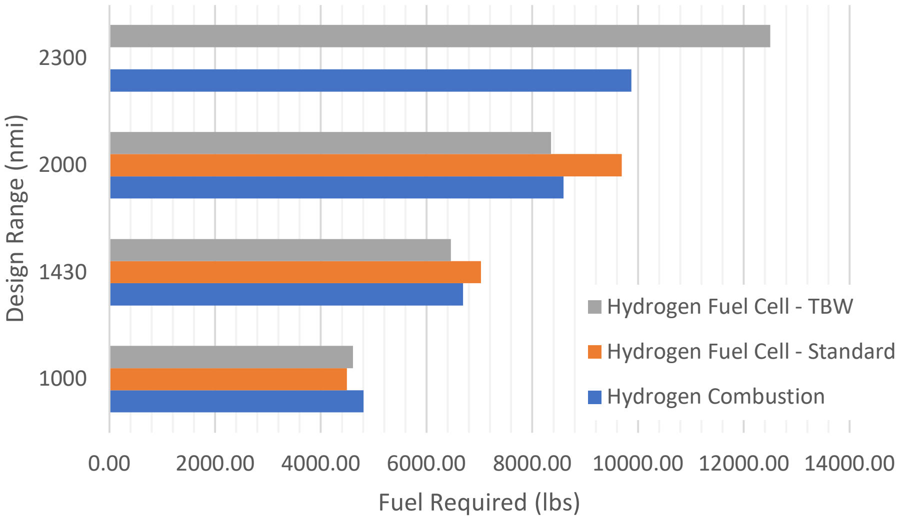

Figure 5.11 Fuel required vs. design range for each tested configuration

As can be noted from Figure 5.11, although the efficiency of the trussed braced wing configuration is much greater than the that of the standard configuration at longer design ranges, at a design range of 1000 nmi the standard configuration is seen to outperform the truss braced wing configuration. This effect is due to the climb performance of each configuration. Although providing a much larger lift to drag ratio at cruise, the truss-based wing is not seen to increase efficiency during the climb. This means that at lower design ranges where the climb has a higher weight fraction of the fuel burnt, the truss can actually be a hinderance to the overall fuel efficiency.

For the missions tested below a design range of 2000 nmi, the truss braced wing hydrogen fuel cell configuration slightly outperforms the hydrogen combustion configuration. At design ranges above 2000 nmi however, the hydrogen fuel cell powered configurations experience a steep drop off in efficiency. In fact, the standard hydrogen fuel cell configuration required a fuel weight so high that it could not complete the climb. This seems to imply that the hydrogen combustion engines will be required for larger, longer-range aircraft configurations.

Chapter 6: Optimization of 2D Airfoils

6.1 Introduction

With preliminary results for the planform shape of the wing, intermediate level design optimization can be conducted in which finer details of the wing such as the airfoil and twist distribution can be determined. The design of modern low drag supercritical airfoils in a transonic flow regime is a highly complex field which relies on the unpredictable computationally expensive predictions of two-dimensional flows containing transitional effects, shock waves, and flow separation. For these reasons this design challenge lends itself well to machine learning algorithms, namely the aforementioned surrogate model-based optimization methods. Still, many complexities plague this process such as the high dimensionality and tradeoffs between accuracy and computational efficiency. The following sections describe this process in detail as well as the methodology used to create a machine learning based airfoil optimization tool. Note that this chapter primarily focuses on the airfoil distribution optimization for the 767-body hydrogen combustion configuration presented in Chapter 3. This case was chosen because it operates in a transonic flight regime, leading to a much more complex aerodynamic optimization problem.

6.2 Airfoil Parameterization

The first step in airfoil optimization is to parameterize the airfoil to a manageable number of variables required to describe its shape in entirety. There are several airfoil parameterization techniques available, two of which are described below.

6.2.1 Bezier-Parsec Parameterization

The Bezier-Parsec parameterization method employs a series of Bezier curves to represent the thickness and camber line of an airfoil [77]. The Bezier-Parsec method is an extension of the classic Bezier parameterization method which uses pure floating Bezier points to represent an airfoil [78]. The added benefit of the Bezier-Parsec method is the use of meaningful aerodynamic values such as the leading edge, maximum thickness, etc., to provide a more physically relevant parameterization, an idea inspired from the Parsec method published by Sobieczky in 1999 [79]. In this method, the leading-edge thickness and camber lines are represented as fourth degree Bezier curves while the trailing edge lines are represented by third degree Bezier curves, leading to a total of 15 design variables. An example of an arbitrarily generated Bezier-Parsec curve generated airfoil is given below in Fig. 6.1.

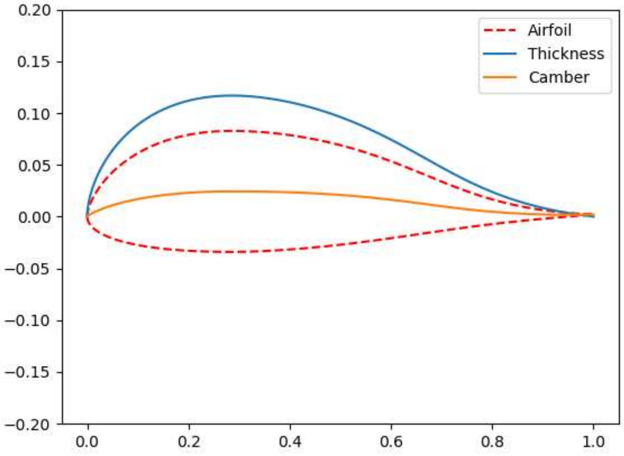

Figure 6.1 Bezier-Parsec Parameterized Airfoil

Despite the previously stated benefits, the Bezier-Parsec parameterization method has notable drawbacks. Due to the presence of cotangent functions in the equations which generate the airfoil, instabilities in the airfoil generation can be seen well within the feasible bounds of a transonic airfoil causing a large number of infeasible and illogical airfoils generated in the random sampling process. This leads to a large number of failed or wasted data points, rendering the optimization process incredibly expensive. Ultimately it was decided not to use the Bezier-Parsec parameterization method after further experimentation with the method. A similar conclusion was reached in Ref. [80].

6.2.2 CST Parameterization

Developed by Brenda M. Kulfan of Boeing in 2007, the Class Shape Transformation (CST) parameterization method uses a series of class and shape functions to describe the upper and lower surface curves of an airfoil [81]. The upper and lower surfaces of the airfoil in CST parameterization respectively are defined by the following equations.

$$\zeta_u(\psi) = C_{N1}^{N2}(\psi) * S_u(\psi) + \psi * \Delta\zeta_u \tag{6.1}$$

$$\zeta_l(\psi) = C_{N1}^{N2}(\psi) * S_l(\psi) + \psi * \Delta\zeta_l \tag{6.2}$$

where ψ and ζ represent the non-dimensional coordinates *x/c* and *z/c* respectively. $\Delta\zeta_u$ and $\Delta\zeta_l$ represent the *z* coordinates at the trailing edge, allowing for the generation of thick trailing edges. These equations are driven by two separate functions, the class function, and the shape function. The class function $C_{N1}^{N2}(\psi)$ is defined as follows.

$$C_{N1}^{N2}(\psi) = \psi^{N1} * (1-\psi)^{N2} \tag{6.3}$$

The values $N1$ and $N2$ can be varied to define different generalized shapes; however, for a round nosed, pointed trailing edge airfoil is defined by $N1$=0.5 and $N2$=1.0. The shape function for the upper and lower surfaces are defined as follows.

$$S_u(\psi) = \sum_{i=0}^{N_u} A_u(i) * S(\psi, i) \tag{6.4}$$

$$S_l(\psi) = \sum_{i=0}^{N_u} A_l(i) * S(\psi, i) \tag{6.5}$$

where the component shape function, S, is defined as follows.

$$S(\psi, i) = \frac{N!}{i!\,(N-i)!} * \psi^i (1-\psi)^{N-i} \tag{6.6}$$

In the above equations, S represents a series of Bernstein Polynomials which are summed to derive a smooth curve to represent the upper and lower surfaces of an airfoil. The variable N in these equations represents the number of Bernstein Polynomials used which consequently is always one less than the number of curvature coefficients used in the variable A. A represents a set of variable weighted curvature coefficients which in turn drive the overall shape of the airfoil, hence A is the set of design variables used in optimization.

CST has been shown to be a highly accurate method in the parameterization of airfoils [80, 81, 82]. With as few as 10 to 14 parameters, the CST method has been found to represent preexisting airfoils with an accuracy similar to that of higher degree parameterization methods such as the Bezier-parsec method [80]. The main drawback of the CST method is the lack of meaningful aerodynamic parameters, meaning that variables such as the maximum thickness ratio of the airfoil cannot be strictly bounded in the optimization. For the airfoil test cases presented here, the CST method is used with a total of 14 design variables: 7 representing the lower surface and 7 representing the upper surface.

6.3 WuFoil

Developed alongside WUADS, WuFoil is an aerodynamic performance analysis and optimization tools used for the design of airfoils with the capability of producing airfoils from lists of coordinates or from CST variables [19]. WuFoil however does not include any built-in analysis methods, it acts instead as an automatic input generation tool for existing aerodynamic performance codes. One such available analysis code is XFOIL, a panel-based design code for airfoils developed by Mark Drela [83]. XFOIL is a widely used high level panel-based airfoil analysis code which uses a coupled algorithm to model both viscous and inviscid effects over an airfoil. XFOIL is highly useful for the design of subsonic airfoil and thus is employed in designing the airfoils for the HFC configuration, however the code struggles to model the transonic and viscous effects at high Reynolds numbers, such as those experienced in the hydrogen combustion configuration. For these cases, WUFoil uses full RANS CFD simulations.

To run a full CFD case around an airfoil, a mesh must be generated first. GMSH is used to generate a full 3D, C - Block mesh around the airfoil. An example of this mesh is shown in Fig. 6.2.

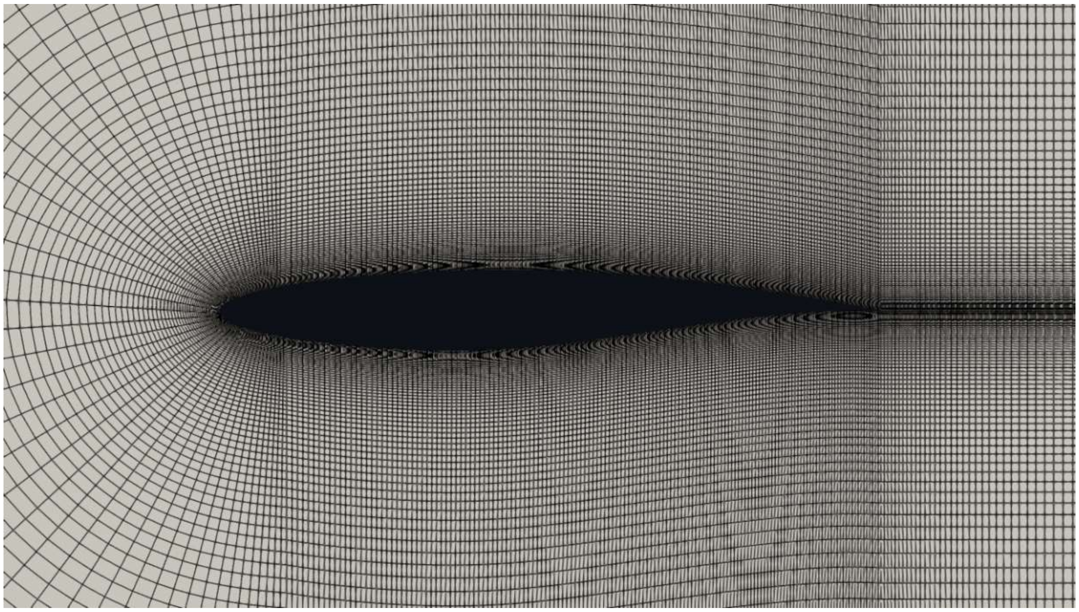

Figure 6.2 WUFoil generated airfoil mesh

The meshes generated by WUFoil naturally have customizable parameters, however the default mesh used in this project has a maximum y+ value of 1 in the boundary layer. The computational domain of the C-block mesh extends 15 chord lengths upstream and 25 chord lengths downstream with 350 grid points on the surface of the airfoil.

This mesh is input into the open source CFD solver SU2. The airfoils are simulated at their respective flow conditions using the compressible RANS equations. The flow in all cases is assumed to be turbulent, therefore the Spalart-Allmaras (SA) turbulence model is used. Far field pressure boundary conditions are used at all boundaries of the computational domain along with a non-slip wall boundary condition on the surface of the airfoil. A feature in SU2 was utilized in all cases to enforce a constant lift coefficient on the airfoil by running adjoint solutions at different angles of attack to determine the lift slope curve.

6.4 Convolutional Neural Networks (CNN) for Airfoil Prediction

6.4.1 Introduction

The Bayesian Optimization method described in Section 2.4 is highly efficient; however the computational cost of running hundreds of full CFD simulations for a single airfoil optimization case is still rather large. To alleviate this problem, an Artificial Neural Network (ANN) of airfoil simulation results was created. An ANN is a machine learning method which uses a collection of “artificial neurons” to establish relations between a multitude of variables. In particular, a multilayer perceptron (MLP) framework can be employed in which neurons are split into separate layers, the first and last of which represent the input and output with the middle neurons representing the intermediate weight functions dictating variables’ relationships. Figure 6.3 shows a sketch of this framework in the context of the problem of airfoil optimization.

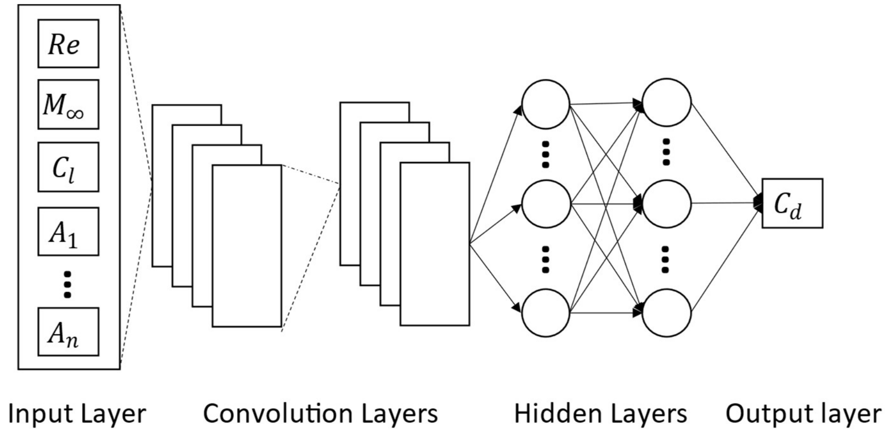

Figure 6.3 A sketch of the framework of Multi-Layer Perceptron (MLP) Artificial Neural Network (ANN)

Within the MLP framework, a set of variables is input which includes the desired lift coefficient, Reynolds number, and airfoil parameterization variables which denote the shape of the airfoil. Each neuron within the specified number of hidden layers represents an operation in which a weight and bias factor are used to determine the proper output. For a more thorough description of this process, see Ref. [84]. Training this network requires the creation a dataset in which hundreds of airfoils denoted by their respective parameterization variables and chord length are evaluated in SU2 simulations to determine their drag coefficient and angle of attack.

A useful tool in the creation of a MLP neural network is the inclusion of one or more convolution layers to create a Convolutional Neural Network (CNN). A convolution layer is designed to identify features within the input data by applying learnable filters called kernels. Each filter extracts specific features from the input, such as edges or patterns, creating a set of feature maps that capture the most relevant information for the task at hand. This is particularly useful in the evaluation of transonic airfoils as convolution layers can detect curves within the outline of the airfoil which may cause phenomena such as shock waves or separation. Similar frameworks have been utilized to analyze the performance of airfoils with reasonable accuracy in several cases in the past [84, 80, 85].

6.4.2 Neural Network Setup

For this task, two separate neural networks were considered. The first CNN consisted of a binary classification model intended to classify airfoils as either feasible or not feasible. In a sense, the point of this model is to predict whether or not an airfoil will provide a converged solution when analyzed using the previously described methodology. This model will allow for the creation of a code which will only generate feasible airfoils, ultimately reducing the number of failed experiments in the optimization process. The second model generated was a dedicated CNN regression model with the intent to predict both the drag coefficient and angle of attack of an airfoil with a set of pre-determined CST parameterization variables and a desired lift coefficient. If determined to be adequately accurate, the predictions generated by this model would be used as an alternative to running full CFD simulations on the sampled airfoils within the Bayesian optimization process, ultimately sharply reducing the total computation time.

Training these neural networks requires the use of a dataset consisting of thousands of airfoils and their simulation results. Unfortunately, the large publicly available airfoil databases such as the UIUC database don’t contain performance data, or the available data was generated using methods that do not include the transonic effects. To address this issue, a database of thousands of airfoils along with their respective simulation results was created. The sampling method to generate sample airfoils for this database was as follows. A set of 25 baseline transonic airfoils was gathered from existing sources and analyzed to determine their respective CST variable sets. Sample airfoils were then generated for the database by selecting one of these airfoils at random and altering their CST variables and desired lift coefficients by adding a random variable with a normal distribution based around 0 with a standard deviation of 0.15. This method was found to provide the necessary variety of airfoils while minimizing the number of failed experiments. In total, about 30% of the tested airfoils were found not to have the converged solutions. A total of 10,000 airfoils were tested for use in the neural network database.

6.4.3 Results

In creating each model, Bayesian optimization was used for hyperparameter tuning to determine the optimum layer sizes, learning rate, etc. After tuning, a similar framework was ultimately used for each model consisting of two convolution layers with 32 and 20 elements and 3 hidden layers with 250, 125, and 75 elements. For model evaluation, the airfoils database was split into training and testing datasets, with the testing data consisting of 20% of the total airfoils. The binary classification model was first trained with the goal of maximizing the overall classification accuracy. After hyperparameter tuning and training, this model was able to classify airfoils as either good or bad with a 92% accuracy. This is far from a perfect model, however the function created to generate only feasible airfoils for optimization purposes using this CNN binary classification model was seen to have reasonable success in reducing the overall computation time. On the other hand, the CNN regression model created was seen to be highly accurate with a mean error of predicted drag coefficients of 0.3% on the testing dataset. Ultimately this was determined to be accurate enough for use as a surrogate model in full airfoil optimization cases; the process and results of which are presented in the next section.

6.5 2D Airfoil Optimization

6.5.1 Problem Setup and Methodology

Two separate two-dimensional airfoil optimization cases were run to test the validity of the methods previously described in conjunction with the Bayesian optimization. Both airfoils were tested with at a Mach number of 0.78. This optimization case used the Python library for Bayesian Optimization with a Successive Response Surface Method (SRSM) domain reduction scheme as described in section 2.4 [34, 37]. Constraints were put on these optimizations to hold the thickness ratio of the optimized airfoils to their original values.

Unfortunately, in running the cases for use in the Bayesian optimization, the methodology described above still experienced several difficulties, most importantly the very high computational cost. Despite the use of machine learning algorithms, the naturally high dimensionality of airfoil parameterization meant a minimum of several hundreds of function calls. This was further amplified by the open design space of the airfoil commonly resulting in highly separated flows which required much more computational resources. The use of the SRSM domain reduction method should have somewhat alleviated this issue; however, a compromise between accuracy and efficiency was still required. Flows which could not be solved to an acceptable residual value within 3000 iterations or diverged were almost exclusively seen to exhibit strong transitional or separation effects, all of which could be reasonably assumed not the optimized results. To account for these failed simulations, a value of 0 was applied for the lift coefficient with the optimizer seeking to maximize the lift to drag ratio.

6.5.2 Results

The B737 mid-span-section airfoil was run with a chord length of 3 Meters, a target lift coefficient of 0.56, and a target thickness ratio of 12%. When run was conducted without the use of the CNN surrogate model, the optimization took about 300 iterations to converge. The resultant airfoil is shown below in Fig. 6.4 compared to the original B737 mid-span section airfoil.

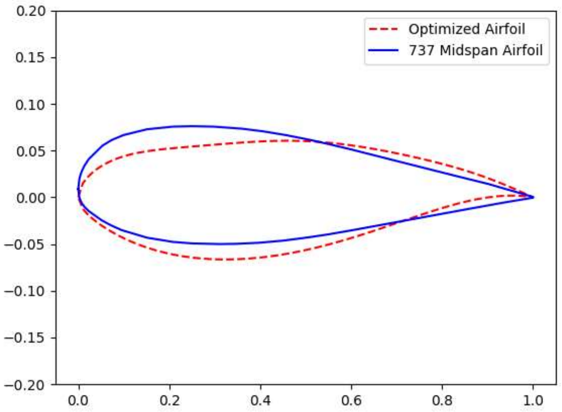

Figure 6.4 Optimized mid-span airfoil compared to the original B737 mid-span airfoil

As can be seen in Fig. 6.4, the optimized mid-span airfoil closely resembles the shape of a modern supercritical airfoil. The flat upper surface and concave lower surface on the airfoil aim to delay the shock formation across upper surface of the airfoil as can be noted in Fig. 6.5.

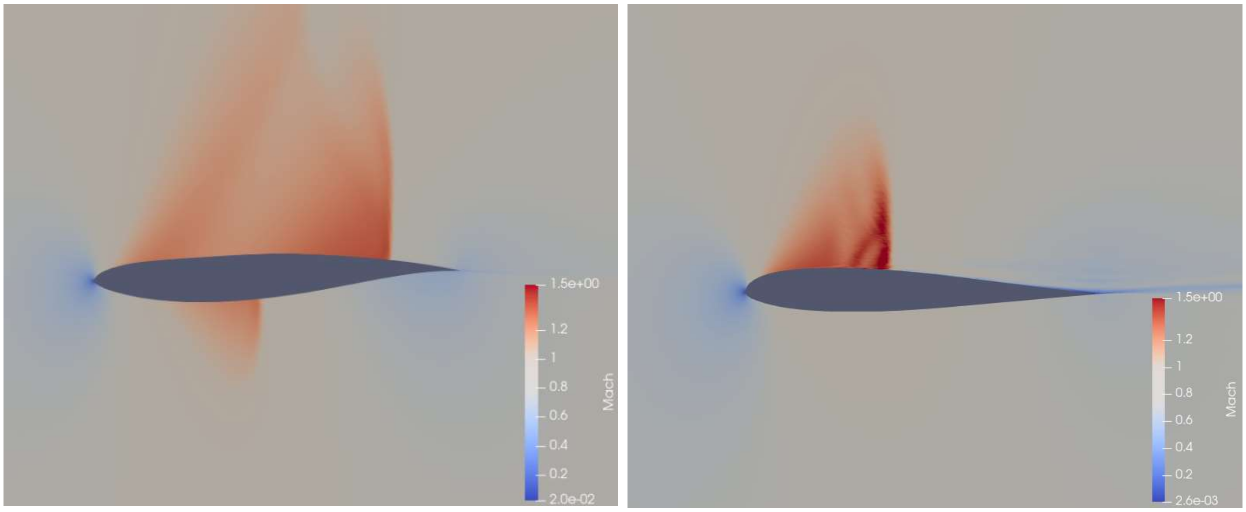

Figure 6.5 Shock wave formation on the surface of the optimized mid-span airfoil (left) and the original B737 mid-span airfoil (right)

Similarly, an optimization case was run for B737 outboard airfoil. In this case, the chord length was set to 1 meter with a thickness ratio of 0.101 and a local Reynolds number of 6 million. According to the elliptical lift distribution, the lift coefficient was set to 0.25. The optimized airfoil is a supercritical airfoil and is compared to the original B737 outboard airfoil in Fig. 6.6 as reported by the UIUC airfoil database. Figure 6.7 shows the supercritical nature of the optimized B737 outboard airfoil.

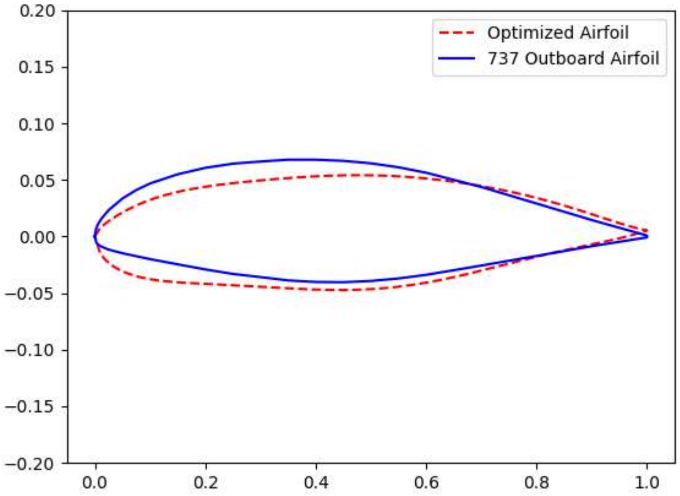

Figure 6.6 Optimized outboard airfoil vs original 737 outboard airfoil

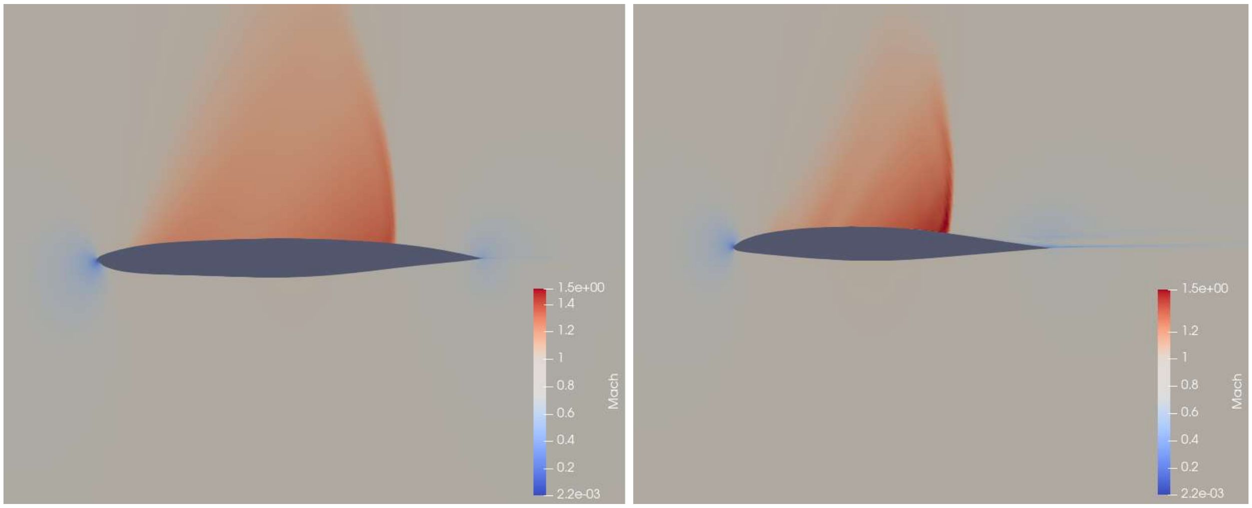

a) Optimized outboard 737 airfoil **b) Original outboard 737 airfoil**

Figure 6.7 Shock wave formation on optimized and original B737 outboard airfoils

Both of these optimization cases were repeated using the trained CNN regression model with airfoil generation filtered through the binary classification CNN model as a surrogate model. The use of this surrogate model in both cases was found to reduce the total run time of the optimization on a lab computer from about 18 hours to about 15 minutes. This optimization resulted in the following airfoils shown in Fig 6.8 in comparison to the optimized airfoil found previously without the use of surrogate modelling.

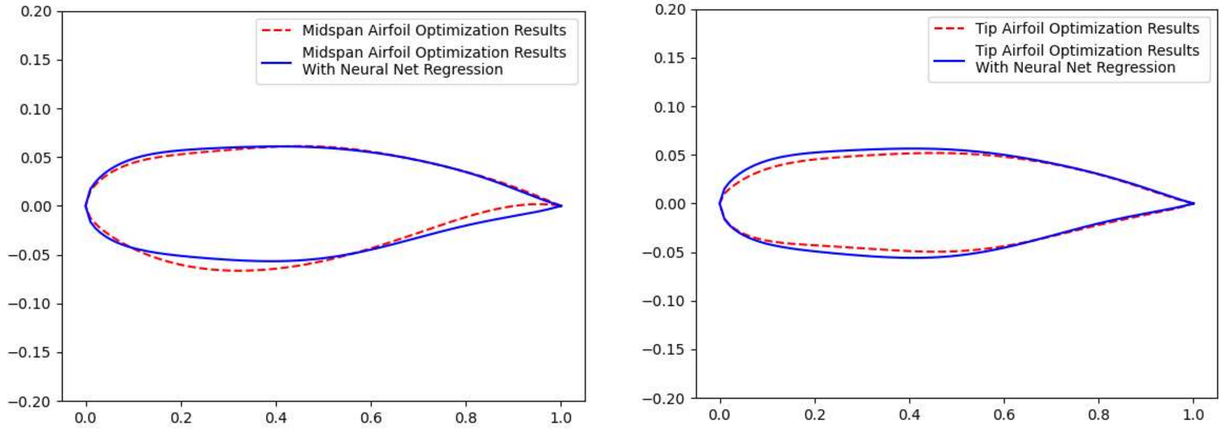

a) Midspan airfoil **b) Outboard airfoil**

Figure 6.8 Comparison of the optimized airfoils with and without neural net regression

As can be seen in Fig. 6.8, the optimized airfoil generated using a neural network regression surrogate model closely resembles that which was generated using the full CFD simulations of each tested airfoil with a few non negligible differences. As shown in Table 6.1, although the airfoils appear similar the airfoils designed using the CNN surrogate model fail to generate airfoils with drag coefficients as low as those generated without the surrogate model.

Table 6.1 Drag coefficients of the optimized airfoils with and without using CNN regression

	Midspan Airfoils C = 3m, Cl = 0.56			Outboard Airfoils C = 1m, Cl = 0.25		
	737 Midspan Airfoil	Optimized Midspan Airfoil	CNN Optimized Midspan Airfoil	737 Outboard Airfoil	Optimized Outboard Airfoil	CNN Optimized Outboard Airfoil
Cd	0.0277	0.00659	0.01056	0.00304	0.00115	0.00214

There are several potential explanations as to why the Bayesian optimization process which used a CNN surrogate model failed to produce as efficient a transonic airfoil as the one which did not. It is most likely that the random nature of the sampling method used to generate airfoils for the CNN training database failed to produce enough low drag, supercritical airfoils for the CNN to identify physical patterns near the optimum point. This problem can potentially be alleviated in the future by inputting a number of airfoils at or near the optimum points into the CNN training data. Nevertheless, it is expected that the optimized results obtained through the use of the surrogate models with finite accuracy would not be as efficient as those obtained through direct simulation results. This is not to say that the generated CNN models are not without their use in the airfoil optimization. An optimization methodology that uses a combination of both methods could likely improve both the computational efficiency issue of the standard Bayesian optimization and the accuracy issue of the CNN surrogate model. Optimized results obtained rapidly using the CNN model can be used for the first iteration of a domain reduction scheme, minimizing the required search space, and mitigating the issue of failed experiments. This process will be used in the remaining airfoil cases in the next chapter.

Chapter 7: Optimization of Airfoils for 3D Wing

7.1 Introduction

The methods described in the previous section work when analyzing and optimizing a purely two-dimensional airfoil; however, other issues must be considered when optimizing airfoil sections of a three- dimensional wing. The basic process of optimizing an airfoil distribution across a wing is to split the wing into several two-dimensional cross-sections and optimize the airfoil of each of these sections. This chapter provides the details of this process. First, the transformation techniques used to map the 2D airfoil results to a 3D wing are presented. These transformation techniques are then used to optimize the full wing of the 767-body hydrogen combustion configuration. Finally, the fully optimized 3D wing is modelled and analyzed using RANS CFD solver. These results are used to validate the mapping techniques as well as the results for lift distribution and drag obtained using WUADS in Chapter 3.

7.2 2D to 3D Airfoil Mapping Methods

7.2.1 2.5D Mapping

The basic correlation between the 2D and 3D airfoils on a simple constant chord swept wing has long been established by the simple sweep theory. In this theory, the Mach number experienced by the airfoil is split into two components - one normal and another tangent to the local sweep angle, Λ. The resultant 3D airfoil is shown in Fig. 7.1.

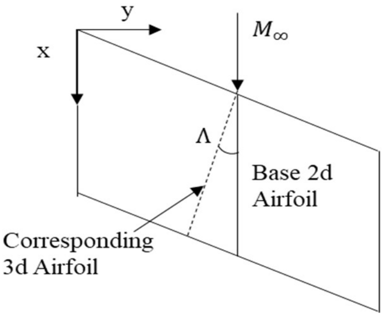

Figure 7.1 Baseline 2D airfoil and 3D airfoil in simple sweep theory

The parameters of the baseline 2D airfoil, namely C_p, C_L, C_D, and M_∞ can be related to the parameters of the corresponding 3D airfoil, denoted as C_p', C_L', C_D', and M_∞' using the following relations [86].

$$C_P' = \frac{C_p}{\cos^2 \Lambda} \tag{7.1}$$

$$C_L' = \frac{C_L}{\cos^2 \Lambda} \tag{7.2}$$

$$C_D' = \frac{C_D}{\cos^2 \Lambda} \tag{7.3}$$

$$M_\infty' = M_\infty \cos \Lambda \tag{7.4}$$

where C_P denotes the pressure coefficient across the airfoil, C_L the lift coefficient, C_D the drag coefficient, and M_∞ the free stream Mach number. This method is well established and has been widely used across the aerospace industry; however, it has some notable limitations in the case of tapered wings [86, 87].

7.2.2 2.75D Mapping

To improve upon the results from simple sweep theory for tapered wings, Lock proposed to use a conical definition of the wing [87]. In Lock's theory, each point along the airfoil's surface is defined on a curvilinear coordinate system originating from the wings origin, S, which is defined as the point at which the leading edge and the trailing edge meet if extended indefinitely. The point,

P, then can be described by and angle θ and a length r from the origin point S. The velocity u can be divided into components along r and θ directions. This coordinate system is shown in Fig. 7.2. Note that using Zhao's terminology, the transformations performed using the simple sweep theory are referred to as "2.5D" transformations whereas the conical methods are referred to as the "2.75D" transformations [86].

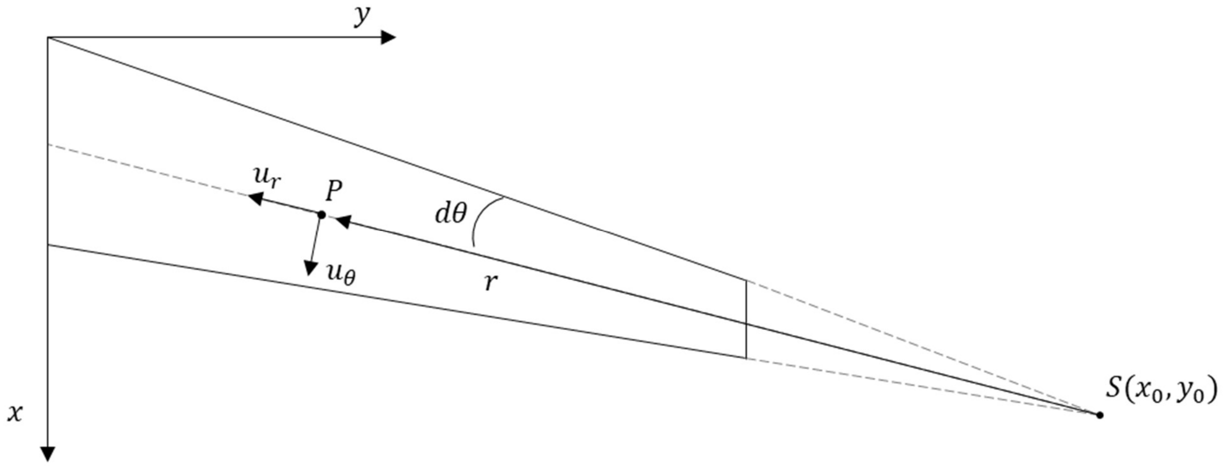

Figure 7.2 Conical parameters on a swept tapered wing

Each airfoil must still have a local sweep angle, Λ. Although the typical practice would be to set this sweep angle to the quarter chord, Streit et. al demonstrated that better results could be obtained for transonic airfoils using the sweep angle of the shock wave across the wing, typically at 50-75% of the chord [88]. Lock's method of airfoil parameter transformation works using the local sweep angle, the wing's reference sweep angle $\tilde{\Lambda}$, and the freestream Mach number M_∞ to transform the pressure coefficient at each point along the surface.

In Lock's method, isentropic flow relations are used to determine the local normal Mach number, M_θ by the equation:

$$1+\frac{1}{2}(\gamma-1)M_\theta^2=\frac{1+\frac{1}{2}(\gamma-1)M_\infty^2\cos^2\mathit{\Lambda}}{\left(1+\frac{1}{2}\gamma M_\infty^2 C_p'\right)^{\frac{\gamma-1}{\gamma}}} \tag{7.5}$$

where C_p' is the pressure coefficient on the 2D airfoil. Assuming the Mach number distribution is the same on the 2D and 3D airfoils, the pressure coefficient at each point on the airfoil surface can be expressed as follows [86, 87].

$$C_p=\frac{f-1}{\frac{1}{2}\gamma M_\infty^2}+fC_p'\,(\cos\widetilde{\Lambda})^2 \tag{7.6}$$

$$f\big(M_\infty,\Lambda,\widetilde{\Lambda}\big)=\left(\frac{1+\frac{1}{2}(\gamma-1)M_\infty^2\cos^2\tilde{\mathit{\Lambda}}}{1+\frac{1}{2}(\gamma-1)M_\infty^2\cos^2\Lambda}\right)^{\frac{\gamma}{\gamma-1}} \tag{7.7}$$

where γ = 1.4, the ratio of specific heats of the air. The above equations extend the assumptions of the simple sweep theory to model the taper effects; however in cases where the local sweep angle is equal to the wing reference sweep angle such as in the case of a single tapered trapezoidal wing, this model becomes equivalent to the results obtained using the simple sweep theory. Note that while the above equations assume isentropic flow, transonic solutions are still feasible as proven by Zhao et al. [86].

7.2.3 2.75D Mapping with Curvature Correction

An improvement can be made to the 2.75D transformation method described in section 7.2.2 by modeling the effects of surface curvature of the airfoil as described by Zhao et al. [86]. In this method, the *z* coordinate of the local airfoil must be defined first as $z=g(x)$. The surface of the wing can then be defined as follows.

$$z=\left(1-\frac{y}{y_0}\right)g(\xi) \tag{7.8}$$

where ξ is the normalized local chordwise coordinate at a point (x,y) defined as follows.

$$\xi = \frac{xy_0 - x_0 y}{y_0 - y} \tag{7.9}$$

In the context of the conical wing parameters shown in Figure 7.3, the coordinates of the point can be expressed as follows [86].

$$\begin{cases} r = \sqrt{(x - x_0)^2 + (y - y_0)^2 + z^2} \\ \theta = y_0 \int_0^{\xi} \frac{\sqrt{1 + [g'(\xi)]^2}}{(x_0 - \xi)^2 + y_0^2 + g^2(\xi)} d\xi \end{cases} \tag{7.10}$$

The velocity components in this coordinate system are defined as u_r and u_θ with the total velocity being defined as $q^2 = u_r^2 + u_\theta^2$. The local normal Mach number in this coordinate system can be estimated as $M_\theta = u_\theta / a_{local}$ where a_{local} is the local speed of sound, which can be estimated by the isentropic relation:

$$\frac{a_{local}^2}{U_\infty^2} = \frac{1}{M_\infty^2} + \frac{1}{2}(\gamma - 1)\left(1 - \frac{q^2}{U_\infty}\right) \tag{7.11}$$

The vorticity of the flow over the airfoil in this coordinate system can be expressed as follows [86].

$$\Omega_\mathrm{n} = \frac{1}{h_\theta h_r}\left[\frac{\partial}{\partial \theta}(h_r u_r) - \frac{\partial}{\partial r}(h_\theta u_\theta)\right] \tag{7.12}$$

where the metric coefficients of the coordinate system are $h_\theta = r$ and $h_r = 1$. Additionally, the flow can be considered irrotational, that is $\Omega = 0$. These simplifications result in the following equation.

$$\frac{du_r}{d\theta} = u_\theta = \sqrt{q^2 - u_r^2} \tag{7.13}$$

Combining Eq. (7.12) with Eq. (7.11) results in the following relation given by Xu et al [89].

$$\frac{du_r}{d_\theta} = u_\theta = \left[\frac{M_\theta \left[a_\infty^2 + \frac{1}{2}(\gamma - 1)(u_\infty^2 - u_r^2)\right]}{1 + \frac{1}{2}(\gamma - 1)M_\theta^2}\right]^{\frac{1}{2}} \tag{7.14}$$

where a_∞ is the freestream speed of sound, u_∞ is the freestream velocity, and M_θ is calculated using Eq. (7.5). Eq. (7.14) is an ordinary differential equation which can be solved using numerical methods. The boundary conditions for this equation are at the airfoil leading edge, $\theta = 0, u_\theta = 0, u_r = u_\infty \sin(\Lambda_{le})$. After solving this equation to obtain the velocity distribution, the following relation can be used for the resultant pressure coefficient.

$$1 + \frac{1}{2}(\gamma - 1)M_\theta\left(1 - \frac{q}{u_\infty}\right) = \left(1 + \frac{1}{2}\gamma M_\theta^2 C_p\right)^{(\gamma-1)/\gamma} \tag{7.15}$$

The difference in the calculated pressure distributions on an airfoil using the previously described methods is small but non negligible. This effect is particularly noticeable in regions where the local sweep angle is different than the reference sweep angle of the wing, for example the inboard section of a double tapered wing. The accuracy of these models is compared in Section 7.3 for the fully optimized airfoil distribution of the 767-body hydrogen combustion aircraft configuration.

7.3 Full Wing Optimization

7.3.1 Problem Set up

Using the previously described 2.75D transformation method with curvature corrections, the full wing airfoil distribution of the 767-body hydrogen combustion aircraft configuration described in chapter 3 was optimized. To optimize the whole wingspan, the wing was split into 10 even segments corresponding to 11 total airfoils, each at increasing increments of 10% of the wingspan. A double tapered geometry was used with the so called “Yehudi Line” at 30% of the wingspan. However, since this is a high wing configuration, the main landing gear does not need to be stored in the wing, meaning that there is discretion in how the double tapered geometry is shaped. To accommodate this, when running the airfoil optimization at the first station at 0% of the wingspan, the chord length was included as a design variable.

7.3.2 Methodology

The same methodology used for the airfoil optimization presented in Chapter 6 was employed. WuFoil was used to generate C-Block meshes around the airfoil which were then analyzed in SU2. The objective function of the optimization problem however was altered. An airfoil creates two types of drag in the optimization, the pressure drag and the friction drag. As described by Atkin and Gowree, when projecting 2D airfoils onto 3D wings these two types of drag do not have the same impact on the overall performance [90, 86]. This means that airfoils cannot be optimized solely to reduce the overall drag. Instead, in a method called the BVGK method, the weights of the two drag components can be summed as follows.

$$C_D = C'_{D_p} \cos^3 \Lambda + C'_{D_f} \cos^{0.2} \Lambda \tag{7.16}$$

where C'_{D_p} and C'_{D_f} are the corresponding calculated 2D pressure and friction drag coefficients, respectively. These drag components can simply be integrated across the surface of the airfoil using the results from SU2.

For the lift coefficient across the wing, an elliptical lift distribution was assumed to minimize the induced drag. This assumption was further supported by investigating the lift distribution of the optimized wing shape obtained in Section 3.3.2 using WUADS, where it was found to closely resemble an elliptical lift distribution. The minimum thickness ratio of the airfoils across the wing were assumed to vary linearly across the two sections of the wing; 0.14 at the root, 0.125 at the Yehudi line, and 0.08 at the tip.

7.3.3 Results

Each airfoil was first optimized using the CNN created in Chapter 6 for domain reduction, then optimized using the Bayesian Optimization with a SRSM model. The airfoils were all modeled with a total of 14 CST variables. The results of this optimization are shown in Fig. 7.3.

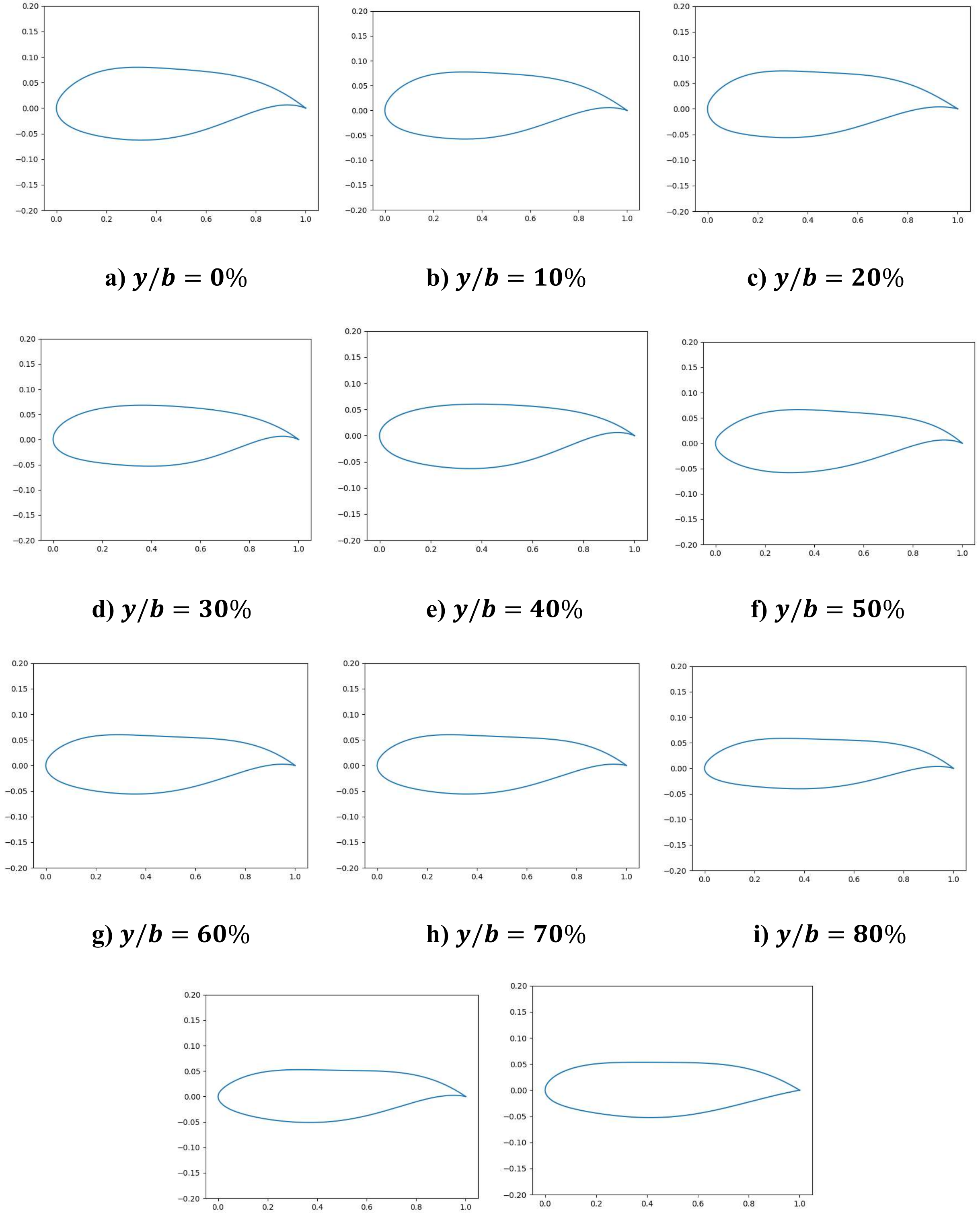

a) $y/b = 0\%$ b) $y/b = 10\%$ c) $y/b = 20\%$

d) $y/b = 30\%$ e) $y/b = 40\%$ f) $y/b = 50\%$

g) $y/b = 60\%$ h) $y/b = 70\%$ i) $y/b = 80\%$

j) $y/b = 90\%$ k) $y/b = 100\%$

Figure 7.3 Airfoil optimization results at various wing sections

Qualitatively, the results in Fig. 7.3 look promising since there are no sharp jumps among the airfoil shapes. Changes in the shape and thickness ratio of the airfoils occur smoothly across the distribution, meaning that the resultant wing shouldn't have any bumps or discontinuities. Additionally, each airfoil section and thus the entire wing demonstrate a clearly supercritical shape. This can be noticed in the shockwave formation on each airfoil as shown in Fig. 7.4.

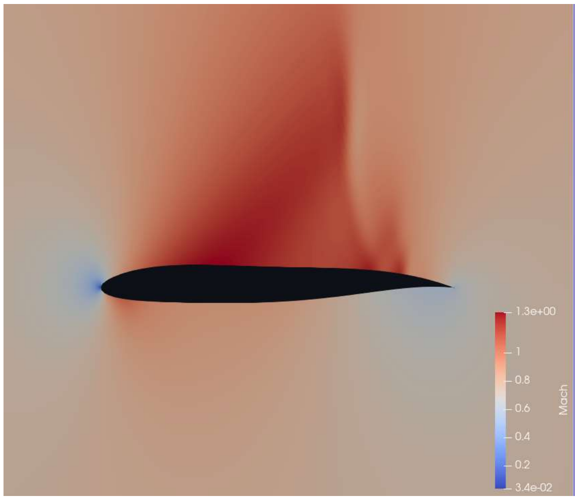

Figure 7.4 Shock wave formation on the optimized airfoil at y/b = 0.6.

7.4 3D Wing Analysis

With the 11 optimized airfoils, the full 3D wing geometry was modelled using NASA's OpenVSP code. As expected, the 3D wing did not contain any noticeable bumps and was found to be an entirely smooth surface. The wing geometry is shown in Fig. 7.5.

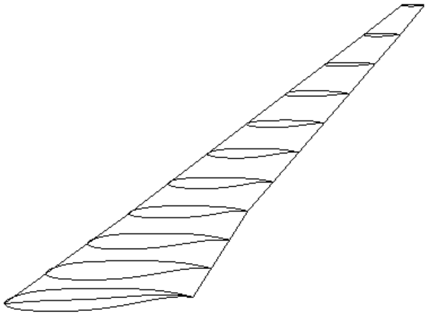

Figure 7.5 3D wing with fully optimized airfoil distribution

7.4.1 Methodology

A very fine structured hex mesh was generated around the optimized wing using ANSYS ICEM. This mesh has a total of 41 million cells with a maximum y+ of 1 in the boundary layer. The computational domain extends 20 times the wingspan downstream and 10 times the wingspan in all other directions. The representative mesh is shown in Fig. 7.6. Note that this is not the actual mesh used in the computation, but is the coarsened version for clarity in the figure.

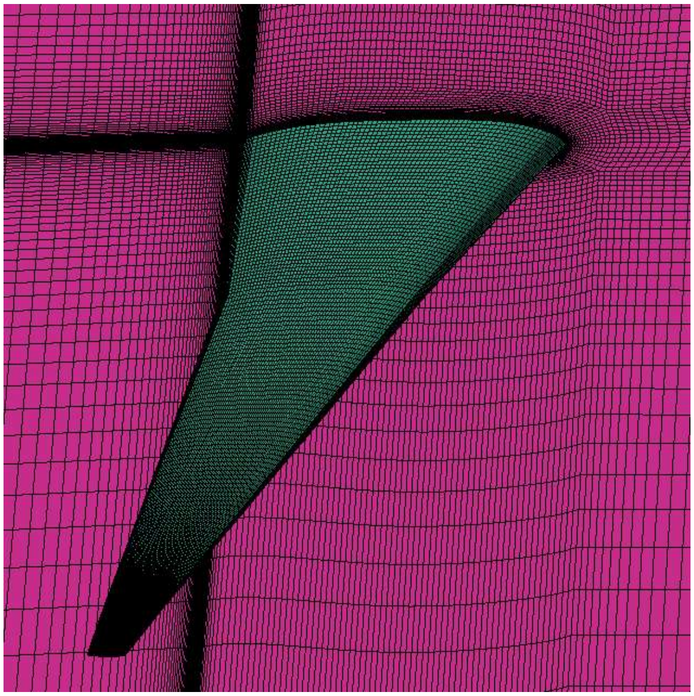

Figure 7.6 Coarsened version of mesh used in full wing CFD simulation.

The CFD simulation was run in ANSYS Fluent using the density-based solver to accurately capture the transonic effects. A Mach number of 0.78 was used. Since the airfoil twist was adjusted at each station to match the desired lift coefficient, the simulation was run at an angle of attack of 0 degrees. Pressure far field boundary conditions were imposed at each of the far field faces of the computational domain. The Spalart-Allmaras turbulence model was used to model the turbulence effects.

7.4.2 Results

The CFD RANS computations on the optimized 3D wing showed a delayed shockwave formation (indicative of the supercritical nature) on the upper surface compared to the non-optimized wing. Figure 7.7 shows the pressure contours on the wing and the shock location.

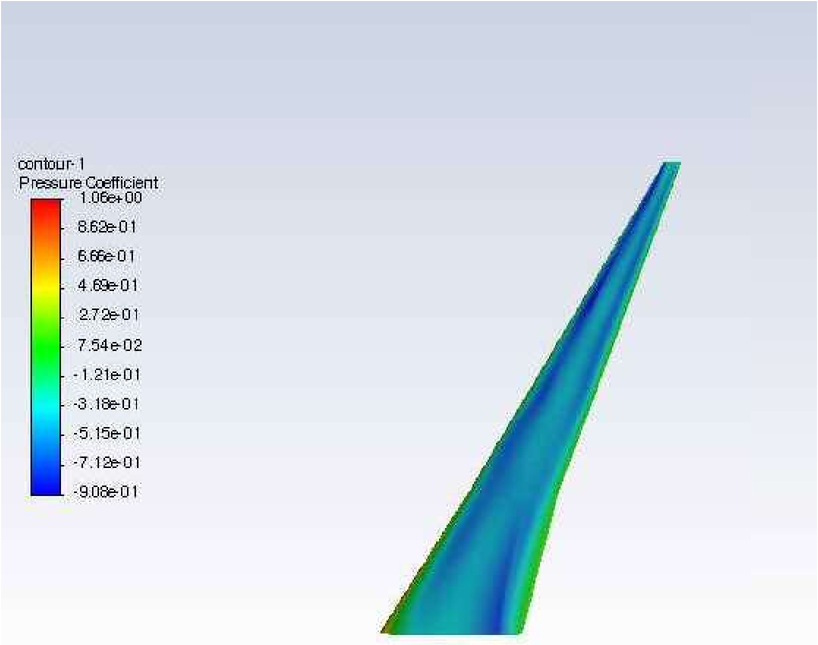

Figure 7.7 Pressure coefficient distribution on the 3D optimized wing.

The pressure coefficient distribution on each airfoil section of the wing can be seen to closely resemble that obtained by using the 2.75D transformation method described in section 7.2. The comparison between the two pressure distributions is shown in Fig. 7.8.

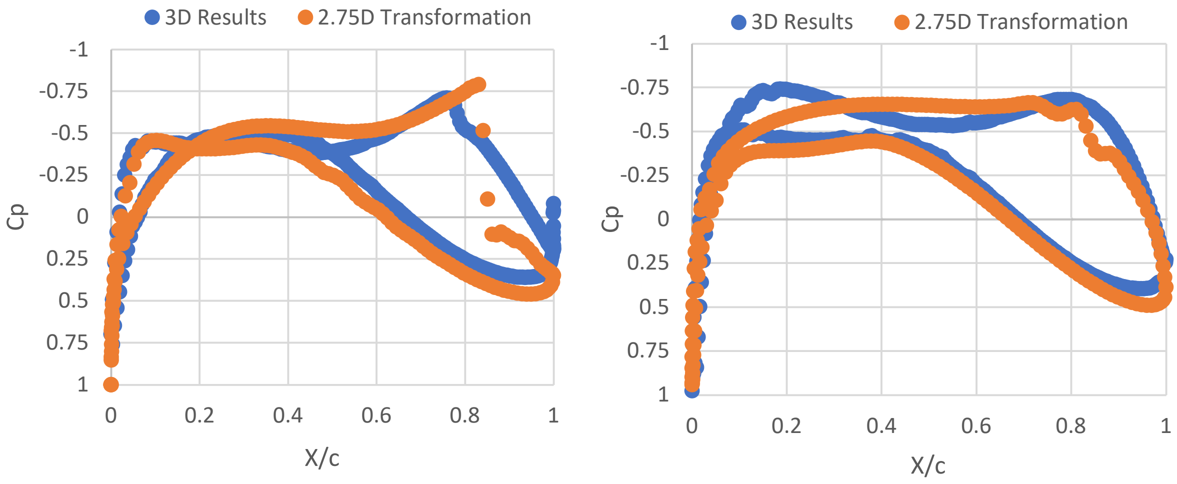

a) 10% Wingspan

b) 40% Wingspan

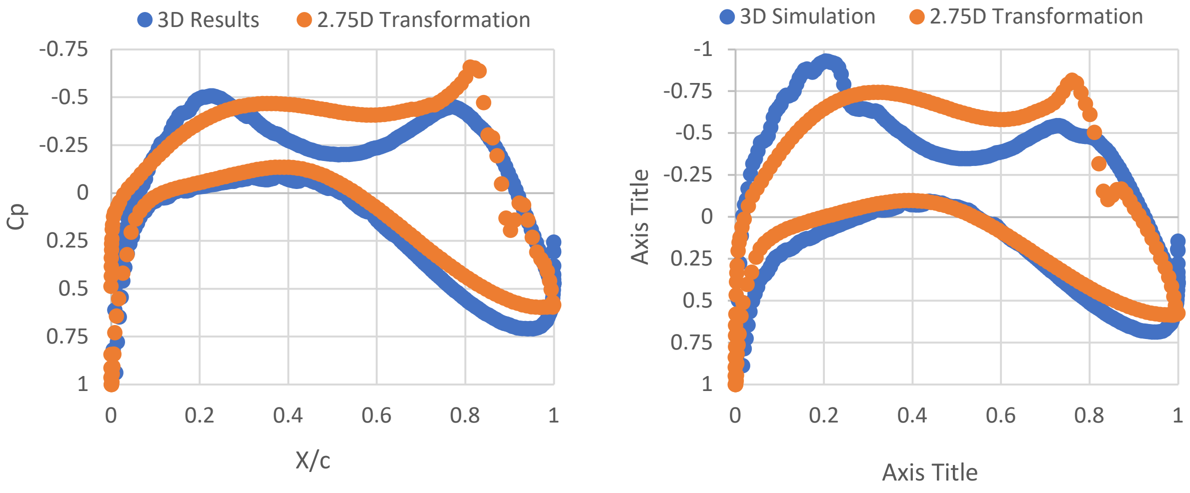

c) 60% Wingspan

b) 90% Wingspan

Figure 7.8 Comparison of pressure distributions on airfoils at various sections of the optimized wingspan using the full 3D CFD and 2.75 D theory.

As can be noted from Fig. 7.8, the pressure distributions predicted by the 3D simulations and 2.75D transformation method exhibit the same general trends; however there is a notable difference in the predicted flow behavior near the leading edge and the shock wave. This error is further amplified near the wing root. It is likely that these differences stem from the differences in methodology between the 2.75D and 3D simulations; however further testing and analysis would be needed to come to a definitive conclusion. It is found however that the 3D airfoil optimization produced a highly efficient supercritical wing with a lift to drag ratio of 27.1 at cruise condition. Note that this value is within 1% of the wing's lift to drag ratio estimated using WUADS validating the methodology. Although there is discrepancy between the 2.75D and 3D methodology, it can still be concluded that the previously described methodology is a highly effective way to optimize the airfoil distribution across the wingspan.

Chapter 8: Summary and Future Work

8.1 Summary

In this dissertation, a comprehensive methodology for the conceptual design of a hydrogen powered aircraft has been developed. This methodology involves using a combination of empirical estimations along with low level simulations to provide rapid analysis of a given aircraft's range and performance. The WUADS code was developed using this methodology and once validated was subsequently used to analyze several configurations of hydrogen powered aircraft. The first configuration tested was a hydrogen combustion powered aircraft based on the performance of the Boeing 737-800. In this study it was shown that a configuration with internal liquid hydrogen (LH2) tanks would greatly improve the efficiency compared to a configuration with externally mounted LH2 tanks. The optimized configuration of hydrogen combustion powered aircraft had an extended fuselage based on that of the Boeing 767 and was shown to improve efficiency compared to Boeing 737-800. Next, the design of an electrified hydrogen fuel cell power train for an aircraft was analyzed. The system architecture was laid out for all the required components, and models were developed to analyze the overall performance. This methodology was used to test the efficiency of three hydrogen fuel cell powered aircraft. The first configuration tested was a small, commuter aircraft based on a retrofitted Cessna 208 Caravan. This case was mainly used for validation purposes. The next case tested was based on the performance of the Bombardier CRJ-200 and was used to analyze the role of increasing the component efficiencies on the viability of hydrogen fuel cell powered aircraft. In this study it was shown that such a configuration could be technologically and economically viable in the next 10-15 years. Lastly, a configuration was tested based on the performance of the Boeing 717-200. This configuration was tested at several mission ranges and was compared to a hydrogen combustion configuration to analyze the difference in efficiencies of different aircraft classes. It was found that the hydrogen fuel cell configurations can be very competitive for a regional to small size airliner, but larger aircraft configurations would probably need to use hydrogen combustion.

Using the optimized hydrogen powered aircraft configurations, the airfoil distributions on a wing section were analyzed. This is a much more detailed design process and therefore required more precise high-fidelity results. RANS CFD simulations were used alongside the machine learning based optimization methods to boost the efficiency. Sleek, highly efficient supercritical airfoils were designed. In an attempt to increase the computational efficiency of this process it was found that artificial neural networks could be used to provide nearly accurate predictions of the optimized airfoils; however they do not produce very precise results. Lastly, a full 3D wing was optimized using the so called 2.75D transformation method. The resulting 3D wing was analyzed employing a full 3D RANS CFD simulation; it was found that although there was slight discrepancy between the 2.75D and 3D simulations, a highly efficient optimized wing could be designed using the 2.75D methodology.

8.2 Future Work

Additional work in the future should focus on the improvement the models employed in the WUADS code for them to be more extendable and applicable to a wide range of aircraft configurations. New models can be created to predict the effects of aircraft configurations such as supersonic aircraft, blended wing body, etc. Additionally, a full propulsion model is not currently available in WUADS but would help in making the code more applicable to configurations operating outside the normal conditions of a commercial airliner.

There are other ways to increase the efficiency of a hydrogen fuel cell powered aircraft which were not modeled in this dissertation. In particular, the use of a fully electrified drivetrain allows for the use of novel efficient propulsion systems, such as the distributed propulsion with boundary layer ingestion. In this dissertation, the propulsion was assumed to come from 2 to 4 wing mounted propellor engines; however there is substantial evidence that the use of a distributed propulsion system with several propellers across the wing span can greatly increase efficiency.

References

[1] P. Su-ungkavatin, L. Tiruta-Barna and L. Hamelin, "Biofuels, electrofuels, electric or hydrogen: A review of current and emerging sustainable aviation systems," *Progress in Energy and Combustion Science,* vol. 96, p. 101073, May 2023.

[2] K. S. Ng, D. Farooq and A. Yang, "Global biorenewable development strategies for sustainable aviation fuel production," *Renewable and Sustainable Energy Reviews,* 2021.

[3] Air Transport Action Group, "Waypoint 2050," September 2021. [Online]. Available: https://aviationbenefits.org/media/167417/w2050_v2021_27sept_full.pdf.

[4] US Department of Energy, "Sustainable Aviation Fuel Grand Challenge," [Online]. Available: https://www.energy.gov/eere/bioenergy/sustainable-aviation-fuel-grand-challenge.

[5] P. J. Ansell, "Review of sustainable energy carriers for aviation: Benefits, challenges, and future viability," *Progress in Aerospace Sciences,* vol. 141, August 2023.

[6] J. O'Malley, N. Pavlenko and S. Searle, "Estimating sustainable aviation fuel feedstock availability to meet growing European Union demand," in *International Council On Clean Transportation*, Berlin, 2021.

[7] M. K. Bradley and C. K. Droney, "Subsonic Ultra Green Aircraft Research: Phase II - Volume II - Hybrid Electric Design Exploration," NASA, 2015.

[8] A. Misra, "Summary of 2017 NASA Workshop on Assessment of Advanced Battery Technologies for Aerospace Applications," in *AIAA SciTech Forum*, Kissimmee, Fl., Jan. 2018.

[9] L. Sun, Y. Liu, R. Shao, J. Wu, R. Jiang and Z. Jin, "Recent progress and future perspective on practical silicon anode-based lithium ion batteries," *Energy Storage Materials,* vol. 46, pp. 482-502, April 2022.

[10] B. Kandelwal, A. Karakurt, P. R. Sekaran, V. Sethi and R. Singh, "Hydrogen powered aircraft: The future of air transport," *Progress in Aerospace sciences,* vol. 60, pp. 45-59, July, 2013.

[11] Boeing, "Boeing Phantom Eye Completes 1st Autonomous Flight," 4 June 2012. [Online]. Available: https://boeing.mediaroom.com/2012-06-04-Boeing-Phantom-Eye-Completes-1st-Autonomous-Flight.

[12] Airbus, "ZEROe: Towards the world's first hydrogen-powered commercial aircraft," [Online]. Available: https://www.airbus.com/en/innovation/low-carbon-aviation/hydrogen/zeroe. [Accessed February 2024].

[13] NASA, "Center for High-Efficiency Electrical Technologies for Aircraft (CHEETA)," [Online]. Available: https://uli.arc.nasa.gov/projects/8/.

[14] GKN Aerospace, "Hydrogen Technologies," [Online]. Available: https://www.gknaerospace.com/en/our-technology/future-technology/hydrogen-technologies/.

[15] ZeroAvia, "ZeroAvia Makes Aviation History, Flying World's Largest Aircraft Powered with a Hydrogen-Electric Engine," Janurary 2023. [Online]. Available: https://zeroavia.com/do228-first-flight/.

[16] L. Blain, "Megawatt-scale liquid H2 airliner powertrain comes to lift," 3 March 2024. [Online]. Available: https://newatlas.com/aircraft/megawatt-liquid-h2-powertrain-aviation/.

[17] M. K. Bradley and C. K. Droney, "Subsonic Ultra Green Aircraft Research: Phase I Final Report," NASA, Jan. 2011.

[18] M. Kiely, "WUADS," 2024. [Online]. Available: github.com/MikeKiely/WUADS.

[19] M. Kiely, "wuFoil," 2023. [Online]. Available: https://github.com/Mikekiely/wuFoil.

[20] D. Raymer, Aircraft Design: A conceptual Approach, Sixth Edition, 2018.

[21] E. Torenbeek, Synthesis of subsonic airplane design: An introduction to the preliminary design of subsonic general aviation and transport aircraft, with emphasis on layout, aerodynamic design, propulsion and performance, 2010.

[22] D. P. Wells, B. L. Horvath and L. A. McCullers, "The Flight Optimization System Weights Estimation Method," NASA Langley Research Center, 2017.

[23] M. Drela and H. Youngren, "Athena Vortex Lattice," February 2022. [Online]. Available: https://web.mit.edu/drela/Public/web/avl/avl_doc.txt.

[24] O. Gur, W. H. Mason and J. A. Schetz, "Full-Configuration Drag Estimation," *Journal of Aircraft,* vol. 47, no. 4, pp. 1356-1367, July 2010.

[25] NASA, "U.S. Standard Atmosphere, 1976," Washington D.C., 1976.

[26] R. S. Shevell, Fundementals of Flight (2nd Edition), 1983.

[27] F. Götten, M. Havermann, C. Braun, M. Marino and C. Bil, "Improved Form Factor for Drag Estimation of Fuselages with Various Cross Sections," *Journal of Aircraft,* vol. 58, no. 3, pp. 549-561, May 2021.

[28] W. Mason, "Analytic models for technology integration in aircraft design," in *Aircraft Design, Systems and Operations Conference*, Dayton, OH, Sept. 1990.

[29] D. Howe, Aircraft Conceptual Design Synthesis, 2000.

[30] O. Schulz, "Assessment of Numerical Models for Thrust and Speific Fuel Consumption for Turbofan Engines," Hamburg University of Applied Sciences, 2007.

[31] J. D. Mattingly, W. H. Heiser and D. T. Pratt, Aircraft Engine Design Second Edition, AIAA Educational Series, 2002.

[32] Y. Yu, Z. Lyu, Z. Xu and J. R. Martins, "On the influence of optimization algorithm and initial design on wing aerodynamic shape optimization," *Aerospace Science and Technology,* vol. 75, pp. 183-199, April, 2018.

[33] T. Head, M. Kumar, H. Nahrstaedt, G. Louppe and I. Scherbatyi, "scikit-optimize/scikit-optimize," Zenodo, 12 October 2021. [Online]. Available: https://github.com/scikit-optimize/scikit-optimize.

[34] F. Nogueira, "Bayesian Optimization: Open source constrained global optimization tool for Python," 2014. [Online]. Available: https://github.com/fmfn/BayesianOptimization.

[35] J. Snoek, H. Larochelle and R. P. Adams, "Practical Bayesian Optimization of Machine Learning Algorithms," in *Neural Information and Processing Systems*, 2012.

[36] J. Görtler, R. Kehlbeck and O. Deussen, "A Visual Exploration of Gaussian Processes," Distill, 2019. [Online]. Available: https://distill.pub/2019/visual-exploration-gaussian-processes/.

[37] N. Stander and K. Craig, "On the robustness of a simple domain reduction scheme for simulation-based optimization," *International Journal for Computer-Aided Engineering and Software,* vol. 19, 2002.

[38] Boeing Commercial Airplanes, "Next-Generation 737 Airplane Characteristics for Airport Planning," Boeing, 2023.

[39] Boeing Commercial Airplanes, "717-200 Airplane Characteristics for Airport Planning," Boeing, 2014.

[40] Gulstream, "Gulfstream g650/g650er," [Online]. Available: https://www.gulfstream.com/en/aircraft/gulfstream-g650er/. [Accessed February 2024].

[41] Bombardier, "CRJ Airport Planning Manual," 2016.

[42] "ICAO Aerodrome Reference Code," Skybrary, [Online]. Available: https://skybrary.aero/articles/icao-aerodrome-reference-code. [Accessed February 2024].

[43] R. E. Carter and R. K. Agarwal, "Development of a Liquid hydrogen Combustion High Bypass Geared Turbofan Model in NPSS," in *AIAA Aviation Forum*, Chicago, 2022.

[44] K. Shank, B. Thomas and R. K. Agarwal, "Insulation Design for Liquid Cryogenic Hydrogen Fuel Tanks for Hydrogen Powered Aircraft," in *AIAA Aviation Forum*, San Diego, 2023.

[45] C. McFarland and R. K. Agarwal, "A Simple Model of Thermal Insulation Design for Cryogenic Liquid Hydrogen Tank," Washington University Department of Mechanical Engineering and Materials Science Independent Study, https://openscholarship.wustl.edu/mems500/176/, 2022.

[46] T. R. Brooks, G. K. W. Kenway and J. R. R. A. Martins, "Benchmark Aerostructural Models for the Study of Transonic Aircraft Wings," *AIAA Journal,* vol. 56, no. 7, 2018.

[47] M. Singh, J. Moore and W. Shadis, "Hydrogen Demand, Production, and Cost by Region to 2050," Argonne National Laboratory, 2005.

[48] IRENA, "Global hydrogen trande to meet the 1.5 C climate goal: Part III - Green hydrogen cost and potential," International Renewable Energy Agency, Abu Dhabi, 2022.

[49] E. Waddington, J. M. Merret and P. J. Ansell, "Impact of LH2 Fuel Cell-Electric Propulsion on Aircraft Configuration and Integration," in *AIAA Aviation Forum*, Virtual, 2021.

[50] G. Vonhoff, "Conceptual Design of Hydrogen Fuel Cell Aircraft," Delft University of Technology, 2021.

[51] M. C. Massaro, R. Biga, A. Kolisnichenko, P. Marocco, A. H. A. Monteverde and M. Santarelli, "Potential and technical challenges of on-board hydrogen storage technologies coupled with fuel cell systems for aircraft electrification".

[52] J. Schröter, T. Graf, D. Frank, C. Bauer, J. Kallo and C. Willich, "Influence of pressure losses on compressor performance in a pressurized fuel cell air supply system for airplane applications," *International Journal of Hydrogen Energy,* vol. 46, no. 40, pp. 21151-21159, 2021.

[53] J. Höflinger and P. Hofmann, "Air mass flow and pressure optimisation of a PEM fuel cell range extender system," *International Journal of Hydrogen Energy,* 2020.

[54] W. J. Song, H. Chen, H. Guo, F. Ye and J. R. Li, "Research progress of proton exchange membrane fuel cells utilizing in high altitude environments," *International Journal of Hydrogen Energy,* vol. 47, no. 59, pp. 24945-24962, 2022.

[55] T. H. Bradley, B. A. Moffitt, D. N. Mavris and D. E. Parekh, "Development and experimental characterization of a fuel cell powered aircraft," *Journal of Power Sources,* vol. 171, no. 2, pp. 793-801, 2007.

[56] A. A. Kasim, M. Chan and E. Marek, "Performance and failure analysis of a retrofitted Cessna aircraft with a FUel Cell Power System fuelled with liquid hydrogen," *Jounal of Power Sources,* vol. 521, 2022.

[57] A. Fly and R. H. Thring, "A coparison of evaporative and liquid cooling methods for fuel cell vehicles," *International Journal of Hydrogen Energy,* vol. 41, no. 32, pp. 14217-14229, 2016.

[58] M. Striednig, M. Cochet, P. Boillat, T. J. Schmidt and F. N. Büchi, "A model based investigation of evaporative cooling for polymer electrolyte fuel cells - Stack lvel analysis," *Journal of Power Sources,* vol. 517, 2022.

[59] Kösters, T. L. Kösters, X. Liu, D. Kožulović, S. Wang, J. Friedrichs and X. Gao, "Comparison of phase-change-heat-pump cooling and liquid cooling for PEM fuel cells for MW-level aviation propulsion," *International Journal of Hydrogen Energy,* vol. 47, no. 68, pp. 29299-29412, 2022.

[60] P. Ranjan, G. K. Das, E. Waddington, M. G. Lauer, P. J. Ansell and K. James, "Preliminary Design and Optimization of a Hydrogen-Electric Aircraft Concept," in *AIAA Aviation Foum*, San Diego, 2023.

[61] C. Hartmann, J. K. Nøland, R. Nilssen and R. Mellerud, "Dual Use of Liquid Hydrogen in a Next-Generation PEMFC-Powered Regional Aircraft With Superconducting Propulsion," *IEEE Transactions on Transportation Electrification,* vol. 8, no. 4, pp. 4760-4778, 2022.

[62] M. O. Hales, N. Wood, S. Harrison, S. Taylor, M. Husband, J. Stonham, C. Zhao, D. Ettridge and D. Westmore, "H2GEAR Hydrogen Electric Powertrain - System Architecture," in *AIAA Aviation Forum*, San Diego, 2023.

[63] M. Lenger, S. Heinke, W. Tegethoff and J. Köhler, "Synergies of fuel cell system thermal management and cryogenic hydrogen exergy utilization," *Scientific Reports,* vol. 12, 2022.

[64] P. Hoenicke, D. Ghosh, A. Muhandes, S. Bhattacharya, C. Bauer, J. Kallo and C. Willich, "Power management control and delivery moduel for a hybrid electric aircraft using fuel cell and battery," *Energy Conversion and Management,* vol. 244, 2021.

[65] G. Romeo, F. Borello, G. Correa and E. Cestino, "ENFICA-FC: Design of transport aircraft powered by fuel cell & flight test of zero emission 2-seater aircraft powered by fuel cells fueled by hydrogen," *International Journal of Hydrogen Energy,* vol. 38, pp. 469-479, 2013.

[66] S. Patel, J. Ahuja, E. Ragauss, J. Gladin and D. N. Mavris, "Development of a Blended Wing Body Aircraft with Hydrogen-Electric Distributed Propulsion," in *AIAA Scitech Forum*, Orlando, 2024.

[67] C. Spiegel, PEM Fuel Cell Modeling and Simulation Using MATLAB, 2008.

[68] J. Wishart, Z. Dong and M. Secanell, "Optimization of a PEM fuel cell system based on empirical data and a generalized electrochemical semi-empirical model," *Journal of Power Sources,* vol. 161, no. 2, pp. 1041-1055, 2006.

[69] M. Azri, A. Nurfatika, A. Mubin, Z. Ibrahim, N. Abd Rahim and S. R. S. Raihan, "Mathematical Modelling for Proton Exchange Membrane Fuel Cell (PEMFC)," *Journal of Theoretical and Applied Information Technology,* vol. 86, no. 3, pp. 409-419, 2016.

[70] J. Larminie and A. Dicks, "Appendix 2: Useful Fuel Cell Equations," in *Fuel Cell Systems Explained, Second Edition*, 2003.

[71] J. W. Chapman, S. L. Schnulo and M. P. Nitzshe, "Development of a Thermal Management System for Electrified Aircraft," in *AIAA SciTech Forum*, Orlando, 2020.

[72] "Cessna 208 Caravan," Textron Aviation, [Online]. Available: https://cessna.txtav.com/en/turboprop/caravan.

[73] W. Bhatti, W. Wu, F. Doyle, J. Llambrich, H. Webber and N. Town, "Fuel Cells: Roadmap Report," Fly Zero, 2022.

[74] "Strategic Research and Innovation Agenda 2021 - 2027," Clean Hydrogen Partnership, 2022.

[75] A. Misra, "Energy Storage for Electrified Aircraft: The Need for Better Batteries, Fuel Cells, and Supercapacitors," *IEEE Electrification Magazine,* vol. 6, no. 3, 2018.

[76] L. Sun, Y. Liu, R. Shao, J. Wu, R. Jiang and J. Zhong, "Recent progress and future perspective on practical silicon anode-based lithium ion batteries," *Energy Storage Materials,* vol. 46, pp. 482-502, 2022.

[77] R. W. Derksen and T. Rogalsky, "Optimum aerofoil parameterization for aerodynamic design," in *OPTI 2009*, 2009.

[78] T. Rogalsky, R. W. Derksen and S. Kocabiyik, "Differential Evolution in Aerodynamic Optimization," 1999.

[79] H. Sobieczky, "Parametric Airfoils and Wings," *Recent Devlopment of Aerodynamic Design Methodologies. Notes on Numerical Fluid Mechanics,* vol. 65, 1999.

[80] K. van Velden, "Surrogate Modelling for Airfoil Shape Optimization," Delft University of Technology, 2017.

[81] B. M. Kulfan, "Universal Parametric Geometry Representation Method," *Journal of Aircraft,* vol. 45, no. 1, 2012.

[82] K. Lane and D. Marshall, "Inverse Airfoil Design Utilizing CST parameterization," in *48th AIAA Aerospace Sciences Meeting*, Orlando, 2012.

[83] M. Drela and H. Youngren, "XFOIL," 2013. [Online]. Available: https://web.mit.edu/drela/Public/web/xfoil/.

[84] S. A. Renganathan, R. Maulik and J. Ahuja, "Enhanced data efficiency using deep neural networks and Gaussian processes for aerodynamic design optimization," *Aerospace Science and Technology,* vol. 111, 2021.

[85] G. Pagliuca, K. Timoleon and S. Mark, "Surrogate modelling for wing planform multidisciplinary optimisation using model-based engineering," *International Journal of Aerospace Engineering,* 2019.

[86] T. Zhao, Y. Zhang, H. Chen, Y. Chen and M. Zhang, "Supercritical wing design based on airfoil optimization and 2.75 transformation," *Aerospace Scient and Technology,* vol. 56, pp. 168-182, 2016.

[87] R. C. Lock, "An Equivalence Law Relating Three- and Two- Dimensional Pressure Distributions," Ministry of Aviation: Aerodynamic Research Council Reports and Memoranda, London, 1962.

[88] T. Streit, G. Wichmann, F. V. K. z. Hatzbach and R. L. Campbell, "Implications of Conical Flow for Laminar Wing Design and Analysis," in *AIAA Applied Aerodynamics Conference*, Honolulu, 2011.

[89] Z.-M. Xu, Z.-H. Han and W.-P. Song, "An improved 2.75D method relating pressure distributions of 2D airfoils and 3D wings," *Aerospace Science and Technology,* vol. 128, 2022.

[90] C. J. Atkin and E. R. Gowree, "Recent developments to the viscous Garabedian and Korn method," in *Congress of the International Council of the Aeronautical Sciences*, Brisbane, 2012.

[91] C. Rice, Interviewee, *Private Correspondance.* [Interview]. October 2022.

[92] M. Kiely, R. K. Agarwal and C. Rice, "Automated Vortex Lattice Method Based Design Optimization of a Hydrogen Powered Aircraft," in *AIAA Aviation Forum*, Chicago, 2022.

[93] J. C. Amphlett, R. M. Baumert, R. F. Mann, B. A. Peppley and P. R. Roberge, "Performance Modeling of the Ballard Mark IV Solid Polymer Electrolyte Fuel Cell: I. Mechanistic Model Development," *Journal of the Electrochemical Society,* vol. 142, 1995.

Appendix A: Weight Estimation Methods

This Appendix provides details of the equations used for aircraft structural weight estimation in the WUADS code. As mentioned in section 2.2.1, WUADS uses a weighted average of the predictions using the three separate methods to calculate the components' structural weight - Raymer [20], Torenbeek [21], and NASA FLOPS [22]. Each component used in weight estimation is listed separately. It is important to note that an additional margin of 6% is applied to the overall aircraft structural weight to account for the unrepresented components and general materials. Note that all the three methods are not used for all the components. Certain methods are omitted due to inaccurate results, added complexity, or the requirement of single use input variables without further improving the results. The weight factors used for the weighted averages are all evenly distributed throughout the three methods unless otherwise indicated. The following terminology is used in the equations. Note that all units are in standard imperial units unless otherwise mentioned.

Nomenclature

W_{dg}: Design gross weight (lbs.)

N_Z: Ultimate load factor (g's)

Λ_x: Sweep angle at normalized x value.

S: Surface area (ft^2)

AR: Aspect Ratio

t/c: Airfoil thickness ratio

λ: Taper ratio

b: Wing-span (ft)

L: Length (ft)

D: Diameter (ft)

S_{wet}: Wetted surface area (ft^2)

Wing

Raymer:

$$W_{wing} = 0.0051\left(W_{dg}N_z\right)^{0.557} S_W^{0.649} AR^{0.5} (t/c)_{root}^{-0.4} * (1+\lambda)^{0.1} (\cos\Lambda_{0.25})^{-1} S_{csw}^{0.1} \qquad (A.1)$$

Torenbeek:

$$W_{wing} = 0.0017 W_{dg}\left(\frac{b}{\cos\Lambda_{0.5}}\right)^{0.75}\left[1+\left\{\frac{6.3\cos\Lambda_{0.5}}{b}\right\}^{0.5}\right] * N_Z^{0.55}\left(\frac{bS_W}{\lambda W_{dg}\cos\Lambda_{0.5}}\right)^{0.3} \qquad (A.2)$$

where

$S_{cs} =$ Control surface area

To improve the accuracy, WUADS assigns a weight of 0.75 to the Raymer's estimate and 0.25 to the Torenbeek's estimate.

Fuselage

Raymer:

$$W_{fuse} = 0.328 K_{door} K_{lg} \left(W_{dg}N_Z\right)^{0.5} L^{0.25} S_{wet}^{0.302} (1+K_{ws})^{0.04} (L/D)^{0.1} \qquad (A.3)$$

Torenbeek:

$$W_{fuse} = 0.021 K_f \left\{\frac{V_D l_h}{w_{fuse} h_{fuse}}\right\}^{0.5} (S_{wet})^{1.2} \qquad (A.4)$$

NASA:
$$W_{fuse} = 1.35 * (LD)^{1.28}(1 + 0.05N_{en})\left(1 + 0.38K_{cf}\right)N_{fuse} \tag{A.5}$$

where

K_{lg} = 1.12 if fuselage mounted landing gear, 1.0 otherwise

$K_{ws} = 0.75\left[\frac{1+2\lambda_{wing}}{1+\lambda_{wing}}\right]\left(\frac{b_{wing}\tan\Lambda_{0.25,wing}}{L}\right)$

K_f = 1.08 for pressurized fuselage, 1.07 for fuselage mounted landing gear, 1.10 for cargo floor (multiply all applicable)

V_D= Dive speed (Knots)

l_h = Tail arm, distance between tail quarter chord and wing quarter chord

w_{fuse} = fuselage width

h_{fuse} = fuselage height

$S_{wet} = \pi DL * \left(1 - \frac{2}{L/D}\right)^{2/3}\left(1 + \frac{1}{(L/D)^2}\right)$ [21]

N_{en} = Number of fuselage mounted engines

K_{cf} = 0 for passenger transport, 1 for cargo transport

Horizontal Tail

Raymer:
$$W_{ht} = 0.0379K_{uht}\left(1 + \frac{F_w}{B_{ht}}\right)^{-0.25} W_{dg}^{0.639}N_Z^{0.10}\,S_{ht}^{0.75}l_h^{-1.0}K_y^{0.704}$$
$$\left(\cos\Lambda_{0.5,ht}\right)^{-1}AR_{ht}^{0.166}\left(1 + \frac{S_{cs}}{S_{ht}}\right) \tag{A.6}$$

Torenbeek:
$$W_{ht} = K_h S_{ht}\left[\frac{3.81(S_{ht}^{0.2}V_d)}{1000\cos^{0.5}\Lambda_{0.5,ht}} - 0.287\right] \tag{A.7}$$

NASA:
$$W_{ht} = 0.53S_{ht}W_{dg}^{0.2}(\lambda_{ht} + .5) \tag{A.8}$$

where

K_{uht} = 1.143 if the whole tail moves, 1.0 otherwise

F_w = Fuselage width at horizontal tail intersection (*ft*)

l_h = Tail arm, distance between tail quarter chord and wing quarter chord

K_y = Aircraft pitching radius of gyration (estimated as $0.3l_h$)

S_{cs} = Elevator surface area

K_h = 1.0 for fixed incidence stabilizer, 1.1 for variable incidence stabilizers

V_d = Dive speed

To improve the accuracy, WUADS assigns a weight of 0.2 to the Raymer's estimate, 0.4 to the NASA's estimate, and 0.4 to the Torenbeek's estimate.

Vertical Tail

Raymer:

$$W_{vt} = 0.0026(1 + H_t/H_v)^{0.225} W_{dg}^{0.556} N_Z^{0.536} l_h^{-0.5} S_{vt} K_Z^{0.875} * \left(\cos \Lambda_{0.5,vt}\right)^{-1} AR_{vt}^{0.35} \, (t/c)_{root}^{-0.5} \qquad (A9)$$

Torenbeek:

$$W_{ht} = K_v S_{vt} \left[\frac{3.81(S_{vt}^{0.2} V_d)}{1000 \cos^{0.5} \mathit{\Lambda}_{0.5,vt}} - 0.287\right] \qquad (A.7)$$

NASA:

$$W_{vt} = 0.32 W_{dg}^{0.3} (\lambda_{vt} + 0.5) N_{vt}^{0.7} S_{vt} \qquad (A.8)$$

where

H_t = Horizontal tail height above fuselage

H_v = Vertical tail height above fuselage at tip

K_Z = Aircraft yawing radius of gyration (estimated as l_h)

K_v = 1.0 for fuselage mounted tails, otherwise $= 1 + 0.15\left(\frac{S_{ht}H_t}{S_{vt}b_v}\right)$

To improve the accuracy, WUADS assigns a weight of 0.2 to the Raymer's estimate, 0.4 to the NASA's estimate, and 0.4 to the Torenbeek's estimate.

Nacelle

Raymer: $$W_{nacelle} = 0.67424K_{ng}L_{nacelle}D_{nacelle}^{0.294}N_Z^{0.119}W_{ec}^{0.611}N_{en}^{0.984}S_{wet}^{0.224} \qquad (A.9)$$

where

K_{ng} = 1.017 for pylon mounted nacelle, 1.0 otherwise

$L_{nacelle}$ = Length of nacelle. Estimated as $0.07\sqrt{T_{max}}$ if unknown

$D_{nacelle}$ = Diameter of nacelle. Estimated as $0.04\sqrt{T_{max}}$ if unknown

W_{ec} = Weight of engine and required components. Estimated as $2.331W_{engine}^{0.901}K_pK_{tr}$ if unknown. Per engine.

N_{en} = Number of engines

T_max = Maximum thrust (lbf.)

Main Landing Gear

Torenbeek: $$W_{mlg} = K_{g_r}\left(20 + 0.04\left(W_{dg}\right)^{0.75} + 0.021W_{dg}\right)$$

NASA: $$W_{mlg} = 0.0117W_{dg}^{0.95}X_{mlg}^{0.43} \qquad (A.10)$$

where

K_{gr} = 1.0 for low wing aircraft, 1.08 for high wing aircraft

Nose Landing Gear

Torenbeek: $$W_{nlg} = K_{g_r}\left(12 + 0.06\left(W_{dg}\right)^{0.75}\right) \qquad (A.11)$$

NASA: $$W_{nlg} = 0.048 W_{dg}^{0.67} X_{nlg}^{0.43} \qquad (A.12)$$

Air Conditioning

NASA $$W_{ac} = 3.2\left(L_{fuselage} W_{fuselage} H_{fuselage}\right)^{0.6} + 9 N_{pass}^{0.83} V_{max} + 0.075 W_{avionics} \qquad (A.13)$$

where

N_{pass} = Number of Passengers

Avionics

Torenbeek: $$W_{avionics} = W_{empty}^{0.556} R_{des}^{0.25} \qquad (A.15)$$

NASA: $$W_{avionics} = 15.8 R_{des}^{0.1} N_{crew} \left(L_{fuselage} * D_{fuselage}\right) \qquad (A.16)$$

where

W_{empty} = Aircraft empty weight = $W_{dg} - W_{fuel} - W_{passengers} - W_{cargo} - W_{crew}$

R_{des} = Design range (nmi)

Anti Icing

Raymer: $$W_{anti-ice} = 0.002 W_{dg} \qquad (A.17)$$

NASA: $$W_{anti-ice} = \frac{B_{wing}}{\cos \Lambda_{0.25,wing}} + 3.8D_{nacelle}N_{en} + 1.5D_{fuselage} \qquad (A.18)$$

where

N_{en} = Number of engines

Auxiliary Power Unit (APU)

NASA $$W_{apu} = 54\left(L_{fuselage}D_{fuselage}\right)^{0.3} + 5.4N_{passengers}^{0.9} \qquad (A.19)$$

Electronics

NASA $$W_{electronics} = 92L_{fuselage}^{0.4}D_{fuselage}^{0.14}N_{fuselage}^{0.27}N_{en}^{0.69} * \left(1 + 0.044N_{crew} + 0.0015N_{passengers}\right) \qquad (A.20)$$

Where

$N\_fuselage$ = Number of fuselages

N_{en} = Number of engines

N_{crew} = Number of flight crew members

$N_{passengers}$ = Number of passengers

Flight Controls

Torenbeek $$W_{fc} = 0.64W_{dg}^{2/3} \qquad (A20)$$

NASA $$W_{fc} = 1.1M_{max}^{0.52}S_{cs}^{0.6}W_{dg}^{0.32} \qquad (A.21)$$

where

M_max = Maximum Mach number

S_cs = Total control surface area

Furnishings

NASA $$W_{furn} = 127n_{crew} + 44n_{passengers} + 2.6L_{pc}(W_{fuselage} + D_{fuselage}) \quad (A.22)$$

where

L_{pc} = length of passenger compartment

Hydraulics

Torenbeek: $$W_{hydraulics} = 0.12W_{dg} \quad (A.23)$$

NASA: $$W_{hydraulics} = 0.57\left(D_{fuselage}L_{fuselage} + 0.27S_{wing}\right) * \left(1 + 0.03N_{en_w} + 0.05 * N_{en_f}\right)\left(\frac{3000}{P_{hyd}}\right)^{0.35} M_{max}^{0.33} \quad (A.24)$$

where

N_{en_w} = Number of wing mounted engines

N_{en_f} = Number of fuselage mounted engines

P_{hyd} = Hydraulic system pressure, 3000 psi by default

M_{max} = Maximum Mach number

Instruments

Raymer: $$W_{instruments} = 4.509K_rK_{tp}N_{crew}^{0.541}N_{en}\left(L_f + B_w\right)^{0.5} \quad (A.25)$$

Torenbeek:

$$W_{Instruments} = N_{crew}\left(15 + 0.32\left(\frac{W_{dg}}{1000}\right)\right) + N_{en}\left(5 + 0.005\left(\frac{W_{dg}}{1000}\right)\right) \qquad (A.23)$$

NASA:

$$W_{instruments} = 0.48\left(D_{fuselage}L_{fuselage}\right)^{0.57} M_{max} * \left(10 + 2.5 * N_{crew} + N_{en_w} + 1.5 * N_{en_f}\right) \qquad (A.26)$$

where

$K_r = 1.133$ if reciprocating engine, 1.0 otherwise

$K_{tp} = 0.793$ if turboprop engine, 1.0 otherwise

Appendix B: Generalized Turbofan Model

As mentioned in section 2.2.5, the WUADS code estimates an engine's uninstalled thrust based on a pre calculated general model of a turbofan engine derived from Mattingly's methods detailed in the book "Aircraft Engine Design, Second Edition" [31]. This is a similar method used by Raymer in his book "Aircraft Design: A Conceptual Approach" [20]. The values used were meant to represent the CFM56-7B24 engine installed on the Boeing 737-800. The values for thrust and specific fuel consumption are given below.

Table B.1 Maximum thrust (lbf.) at different altitudes (ft.) and Mach Numbers

	Mach Number									
ALTITUDE	**0**	**0.1**	**0.2**	**0.3**	**0.4**	**0.5**	**0.6**	**0.7**	**0.8**	**0.9**
0	24200	21453	19316	17616	16221	15043	14084	13343	12732	12340
5000	20134	18149	16697	15684	15022	14061	13231	12669	12109	11639
10000	16940	15281	13991	13186	12647	12425	12466	11909	11398	11069
20000	11948	10723	9886	9323	8942	8761	8754	8992	9367	9755
30000	8482	7603	7045	6551	6371	6230	6220	6381	6681	7045
36000	7030	6255	5812	5480	5203	5148	5093	5259	5480	5812
45000	5484	4930	4551	4245	4084	4026	4011	4142	4332	4594

Table B.2 Specific fuel consumption at different altitudes (ft.) and Mach Numbers

	Mach Number									
ALTITUDE	**0**	**0.1**	**0.2**	**0.3**	**0.4**	**0.5**	**0.6**	**0.7**	**0.8**	**0.9**
0	0.375	0.422	0.480	0.510	0.633	0.703	0.797	0.961	1.230	1.793
15000	0.375	0.396	0.429	0.485	0.546	0.614	0.698	0.787	0.899	1.081
31000	0.315	0.357	0.393	0.437	0.481	0.539	0.578	0.657	0.717	0.822
35000	0.315	0.350	0.382	0.422	0.460	0.500	0.550	0.610	0.678	0.760
41000	0.300	0.363	0.392	0.419	0.458	0.509	0.546	0.615	0.672	0.726

To provide accurate estimates for both the thrust and the specific fuel consumption at a specified altitude and Mach number, these values are scaled using a method suggested by Chris

Rice in a private correspondence [91]. In this method, there are four input variables for a desired engine: thrust at sea level T_{sl}, thrust at cruise T_{cruise}, specific fuel consumption at sea level c_{sl}, and specific fuel consumption at cruise c_{cruise}. Both the specific fuel consumption and the thrust tables are altered as follows: they are scaled using a weighted bilinear interpolation to ensure accurate values at both cruise and at sea level. This gives updated versions of charts B.1 and B.2 which effectively maintain the same trends as the general turbofan model but are changed to fit the input engine. Considering an overwhelming majority of the fuel is burnt during cruise, this estimate should be fairly accurate for use in the range estimation.